9-4-2018

Threshold Resonance Effects and the Phase-Amplitude Approach

Di Shu
University of Connecticut - Storrs, di.shu.phys@gmail.com

Threshold Resonance Effects and the Phase-Amplitude Approach

Di Shu, Ph.D.

University of Connecticut, 2018

A fundamental aspect of scattering is the appearance of resonances, which appear in many systems. Although their effect is often lost due to averaging at room temperatures or higher, they can become dominant features at low or ultralow temperatures, where only a few partial waves contribute to the scattering process. Our ability to form and manipulate ultracold molecules provides the seed to study in a precise and controlled fashion the role of single partial waves, and state-to-state processes in chemical systems. We explore resonances occurring due to the existence of a quasi-bound state in the entrance channel of a scattering system and explain the energy scaling due to these near threshold resonances (NTR) based on the properties of the Jost functions. We also investigate the threshold resonance effects in the Efimov systems which have been studied in a variety of context, such as three-body Coulomb systems and nuclear three-body systems. Numerical schemes based on Milne's phase-amplitude approach are formulated to analyze NTR effects. We present a simple and practical approach to solve the long-standing problem of finding the non-oscillatory solution to Milne's equation. Our numerical approach also gives an integral representation of scattering phase shift and allows us to compute ultra-narrow shape resonances.

Threshold Resonance Effects and the Phase-Amplitude Approach

Di Shu

Diploma, Huazhong University of Science and Technology, China

A Dissertation

Submitted in Partial Fulfillment

of the Requirements for the Degree of

Doctor of Philosophy

at the

University of Connecticut

2018

APPROVAL PAGE

Doctor of Philosophy Dissertation

Threshold Resonance Effects and the Phase-Amplitude Approach

Presented by

Di Shu

Major advisor _____
Robin Côté

Associate advisor _____
John Montgomery

Associate advisor _____
Susanne Yelin

University of Connecticut

2018

for my fiancée Yue Wang

Acknowledgements

I would like to thank my major advisor Prof. Robin Côté, and also Prof. Susanne Yelin and Prof. John Montgomery, my associate advisors. I am very lucky to have the opportunity to work in Robin's group where I learned a lot and received helps in many aspects. Robin's guidance, ideas and discussions are invaluable to me and along with his friendly and easy going approach, that makes Robin one of the best advisors.

I give my special thanks to Ionel Simbotin. He is my best friend and mentor. He patiently guided me into my research. His knowledge in physics is so helpful to me that I think I would spend much more time without it. As a friend he is generous, considerate and fun; he definitely makes my life in the group more enjoyable.

I would like to also thank my other group members, Marko Gacesa, Jia Wang and Jovica Stanojevic. I learned a lot from them and we had such a great time.

My friends also made my time in grad school more enjoyable. I would like to thank my formal housemates Wenbo Li, Kan Fu and Hongyu Hu, etc.

I give my warmest thanks to my fiancée Yue Wang. Her support is crucial to me throughout my last couple of years as a grad student. She took care of me when I was in a lot of pressure and she encouraging words are the fuel for me to keep working hard.

Table of Contents

List of Figures

Figure **Page**

Chapter 1
Introduction

1.1 Radial Equation

In a scattering problem, the scattering wave function $\Psi^+_{\boldsymbol{k},i}$ for a projectile with momentum $\boldsymbol{p} = \hbar\boldsymbol{k}$ incident on a target in internal eigenstate i can be expanded onto a complete basis representing the channels. Here, we review the case of non-reactive processes, where the initial arrangement remains intact after the scattering event, though the general results are applicable to the reactive case. A more thorough discussion can be found in several scattering textbooks, such as [1, 2, 3]. We consider the Hamiltonian

$$H = \left(\frac{\boldsymbol{p}^2}{2\mu} + H_{\text{target}}\right) + V(\boldsymbol{r}, \boldsymbol{s}), \tag{1.1}$$

where $\boldsymbol{r}$ is the position projectile and $\boldsymbol{s}$ the set of coordinates describing the target, μ is the reduced mass of the projectile and target, and $V(\boldsymbol{r}, \boldsymbol{s})$ the interaction between them. H_{target} dictates the target dynamics, with the eigenstates $H_{\text{target}}\chi_n(\boldsymbol{s}) = E_n\chi_n(\boldsymbol{s})$, and we expand the full wavefunction $\Psi^+_{\boldsymbol{k},i}(\boldsymbol{r}, \boldsymbol{s})$ in the basis $\{\chi_n\}$,

$$\Psi^+_{\boldsymbol{k},i}(\boldsymbol{r}, \boldsymbol{s}) = \sum_n \psi_{n,i}(\boldsymbol{r})\chi_n(\boldsymbol{s}), \tag{1.2}$$

where $\psi_{n,i}(\boldsymbol{r})$ are the channel components, and the sum runs over discrete and continuum states. The asymptotic behavior reads

$$\psi_{n,i}(\boldsymbol{r}) \xrightarrow{\boldsymbol{r}\to\infty} \delta_{ni} e^{i\boldsymbol{k}\cdot\boldsymbol{r}} + f_{ni}\frac{e^{ik_n r}}{r}, \tag{1.3}$$

where $f_{ni} \equiv f(\boldsymbol{k}_n, n \leftarrow \boldsymbol{k}, i)$ stands for the scattering amplitude from the initial channel i with momentum $\boldsymbol{p} = \hbar\boldsymbol{k}$ into the channel n with momentum $\boldsymbol{p}_n = \hbar\boldsymbol{k}_n$.

Applying H onto the expansion (1.2) for $\Psi^+_{\boldsymbol{k},i}(\boldsymbol{r},\boldsymbol{s})$, and using $\int d\boldsymbol{s}\, \chi^*_m(\boldsymbol{s})\chi_n(\boldsymbol{s}) = \delta_{mn}$, one obtains the system of coupled equations [1]

$$-\frac{\hbar^2\nabla^2_{\boldsymbol{r}}}{2\mu}\psi_{m,i} + \sum_n V_{mn}\psi_{n,i} = (E - E_m)\psi_{m,i}, \tag{1.4}$$

where

$$V_{mn}(\boldsymbol{r}) \equiv \int d\boldsymbol{s}\, \chi^*_m(\boldsymbol{s}) V(\boldsymbol{r},\boldsymbol{s})\chi_n(\boldsymbol{s})\ . \tag{1.5}$$

Although there is an infinite set of coupled equations, one restricts the sum in Eq. (1.2) to a finite number N of discrete terms, provided the collision energy is low enough, to obtain the *close-coupling approximation*.

If we label the initial channel $i = 1$, the solution $\boldsymbol{\psi}_1(\boldsymbol{r})$ of the scattering problem (1.4) can be rewritten in matrix form

$$\nabla^2\boldsymbol{\psi}_1(\boldsymbol{r}) - \mathbf{U}(\boldsymbol{r})\boldsymbol{\psi}_1(\boldsymbol{r}) + \mathbf{K}^2\boldsymbol{\psi}_1(\boldsymbol{r}) = 0\ , \tag{1.6}$$

where $\boldsymbol{\psi}_1$ is a column with elements $\psi_{n,1}$ and $\mathbf{K}$ is a diagonal matrix,

$$\boldsymbol{\psi}_1(\boldsymbol{r}) = \begin{pmatrix} \psi_{1,1}(\boldsymbol{r}) \\ \vdots \\ \psi_{N,1}(\boldsymbol{r}) \end{pmatrix}, \qquad \mathbf{K} = \begin{pmatrix} k_1 & & 0 \\ & \ddots & \\ 0 & & k_N \end{pmatrix}, \tag{1.7}$$

with $k_n = \sqrt{2\mu(E - E_n)/\hbar^2}$, and where $\mathbf{U}(\boldsymbol{r})$ is an $N \times N$ matrix with elements $U_{mn} = \frac{2\mu}{\hbar^2} V_{mn}$. In general, the entrance channel can be any of $i = 1, \ldots, N$, leading to N distinct solutions $\boldsymbol{\psi}_1(\boldsymbol{r}), \ldots, \boldsymbol{\psi}_N(\boldsymbol{r})$, with each column $\boldsymbol{\psi}_i(\boldsymbol{r})$ describing the collision problem for initial channel i, and Eq. (1.6) can be rewritten as

$$\nabla^2 \boldsymbol{\Psi} - \mathbf{U}\boldsymbol{\Psi} + \mathbf{K}^2 \boldsymbol{\Psi} = 0, \tag{1.8}$$

where $\boldsymbol{\Psi}$ is the matrix

$$\boldsymbol{\Psi} = \left(\boldsymbol{\psi}_1,\ \boldsymbol{\psi}_2,\ \ldots\ , \boldsymbol{\psi}_N \right), \tag{1.9}$$

and the columns $\boldsymbol{\psi}_i$ read

$$\boldsymbol{\psi}_i = \begin{pmatrix} \psi_{1,i} \\ \psi_{2,i} \\ \vdots \\ \psi_{N,i} \end{pmatrix}. \tag{1.10}$$

1.2 Scattering basic

For simplicity, we consider the case of spinless particles, such that the system is rotationally invariant. Thus, a partial wave expansion can be employed for the solutions $\boldsymbol{\psi}_i(\boldsymbol{r})$ [1],

$$\boldsymbol{\psi}_i(\boldsymbol{r}) = \sum_{\ell=0}^{\infty} \frac{(2\ell+1)}{kr} \boldsymbol{\psi}_i^{(\ell)}(r) P_\ell(\cos\theta), \tag{1.11}$$

where $\cos\theta = \hat{\boldsymbol{r}} \cdot \hat{\boldsymbol{k}}_i$. For each ℓ and for each i, the vector (column) $\boldsymbol{\psi}_i^{(\ell)}(r)$ satisfies the radial equation

$$\left[\mathbf{I} \frac{d^2}{dr^2} - \mathbf{I} \frac{\ell(\ell+1)}{r^2} - \mathbf{U}(r) + \mathbf{K}^2 \right] \boldsymbol{\psi}_n^{(\ell)}(r) = 0, \tag{1.12}$$

where $\mathbf{I}$ is the $N \times N$ unit matrix.

For each angular momentum ℓ, we consider N distinct solutions denoted as vectors (columns) $\boldsymbol{\psi}_n^{(\ell)}(r)$, with $1 \le n \le N$. Each vector $\boldsymbol{\psi}_n^{(\ell)}(r)$ has N components $\psi_{mn}^{(\ell)}(r)$ obeying the asymptotic behavior

$$\begin{aligned}\psi_{mn}^{(\ell)}(r) &\xrightarrow{r\to\infty} C_n \left[i^\ell s_\ell(k_n r)\delta_{mn} + k_n f_{mn}^{(\ell)} e^{ik_m r} \right] \\ &= C_n \tfrac{i^{2\ell+1}}{2} \left[e^{-ik_n r}\delta_{mn} - (-1)^\ell \sqrt{\tfrac{k_n}{k_m}} S_{mn}^{(\ell)} e^{ik_m r} \right], \end{aligned} \tag{1.13}$$

where $s_\ell(x) = x j_\ell(x)$ is the Riccati–Bessel function, and $C_n(k_n)$ is a normalization constant. The scattering amplitudes $f_{mn}^{(\ell)}$ and the elements $S_{mn}^{(\ell)}$ of the S-matrix are related by

$$S_{mn}^{(\ell)} = \delta_{mn} + 2i\sqrt{k_m k_n} f_{mn}^{(\ell)} \, . \tag{1.14}$$

It is apparent in Eq. (1.13) that for each vector $\boldsymbol{\psi}_n^{(\ell)}(r)$ the incident wave is in component $\psi_{nn}^{(\ell)}(r)$ corresponding to channel n. The columns $\boldsymbol{\psi}_n^{(\ell)}(r)$ form an $N \times N$ matrix,

$$\boldsymbol{\Psi}^{(\ell)}(r) = \left(\boldsymbol{\psi}_1^{(\ell)}(r), \boldsymbol{\psi}_2^{(\ell)}(r), \ldots, \boldsymbol{\psi}_N^{(\ell)}(r) \right) \, , \tag{1.15}$$

and the asymptotic behavior in Eq. (1.13) can be recast in matrix notation,

$$\begin{aligned}\boldsymbol{\Psi}^{(\ell)}(r) &\xrightarrow{r\to\infty} \left[i^\ell s_\ell(\mathbf{K}r) + e^{i\mathbf{K}r}\mathbf{F}^{(\ell)}\mathbf{K} \right] \mathbf{C}(\mathbf{K}) \\ &= \frac{i^{2\ell+1}}{2} \Big[e^{-i\mathbf{K}r} - (-1)^\ell e^{i\mathbf{K}r} \mathbf{K}^{-1/2} \mathbf{S}^{(\ell)} \mathbf{K}^{1/2} \Big] \mathbf{C}(\mathbf{K}), \end{aligned} \tag{1.16}$$

where $\mathbf{F}^{(\ell)}$ and $\mathbf{S}^{(\ell)}$ are the matrices for $f_{mn}^{(\ell)}$ and $S_{mn}^{(\ell)}$, and with the diagonal matrices $\mathbf{K} = \mathrm{diag}\{k_j\}$ (see Eq. (1.7)), $\mathbf{K}^{\pm 1/2} = \mathrm{diag}\{k_j^{\pm 1/2}\}$, $\mathbf{C}(\mathbf{K}) = \mathrm{diag}\{C_j(k_j)\}$, $s_\ell(\mathbf{K}r) =$

$\mathrm{diag}\{s_\ell(k_j r)\}$, and $e^{\pm i\mathbf{K}r} = \mathrm{diag}\{e^{\pm ik_j r}\}$. The relationship between the scattering amplitudes and the S-matrix in Eq. (1.14) can thus be written as

$$\mathbf{S}^{(\ell)} = \mathbf{I} + 2i\mathbf{K}^{1/2}\mathbf{F}^{(\ell)}\mathbf{K}^{1/2} \,. \tag{1.17}$$

The differential cross sections for multi-channel scattering, with and without rearrangement [1], take the well known expression:

$$\frac{d\sigma_{m\leftarrow n}}{d\Omega} = \frac{k_m}{k_n}|f_{mn}|^2. \tag{1.18}$$

In general, the exact form of the expression depends on the angular momenta, internal structure, and the exact interactions entering the Hamiltonian, such as interaction with external fields, etc. For the simpler rotationally invariant and spinless system satisfying equations (1.11) and (1.12), we have

$$f_{mn}(\theta) = \sum_{\ell=0}^{\infty}(2\ell+1)f_{mn}^{(\ell)}P_\ell(\cos\theta), \tag{1.19}$$

where θ is the scattering angle. Integrating over angles, and using the properties of the Legendre polynomials P_ℓ, one obtains the cross sections for state-to-state transitions,

$$\sigma_{m\leftarrow n}(k_n) = 4\pi\frac{k_m}{k_n}\sum_{\ell=0}^{\infty}(2\ell+1)|f_{mn}^{(\ell)}|^2 \,, \tag{1.20}$$

which can be rewritten, with the help of Eq. (1.14), as

$$\sigma_{m\leftarrow n}(k_n) = \frac{\pi}{k_n^2}\sum_{\ell=0}^{\infty}(2\ell+1)|\delta_{mn} - S_{mn}^{(\ell)}|^2 \tag{1.21}$$

$$= \frac{\pi}{k_n^2}\sum_{\ell=0}^{\infty}(2\ell+1)|T_{mn}^{(\ell)}|^2 = \sum_{\ell=0}^{\infty}(2\ell+1)\sigma_{m\leftarrow n}^{(\ell)}. \tag{1.22}$$

The terms $\sigma^{(\ell)}_{m\leftarrow n}$ are the contributions corresponding to partial waves ℓ, and they are defined as

$$\sigma^{(\ell)}_{m\leftarrow n}(k_n) \equiv \frac{\pi}{k_n^2}|T^{(\ell)}_{mn}(k_n)|^2. \tag{1.23}$$

Note that in the equations above we employed the T-matrix, $\mathbf{T} = \mathbf{I} - \mathbf{S}$, with elements

$$T^{(\ell)}_{mn} = \delta_{mn} - S^{(\ell)}_{mn}.$$

Using the unitarity of the S-matrix, namely $1 = \sum_m |S^{(\ell)}_{mn}|^2 = |S^{(\ell)}_{nn}|^2 + \sum_{m\neq n} |S^{(\ell)}_{mn}|^2$, the cross sections for elastic and inelastic scattering read

$$\sigma_n^{\rm elast} \equiv \sigma_{n\leftarrow n} = \frac{\pi}{k_n^2}\sum_{\ell=0}^{\infty}(2\ell+1)\Big|1 - S^{(\ell)}_{nn}\Big|^2, \tag{1.24}$$

$$\sigma_n^{\rm inel} \equiv \sum_{m\neq n}\sigma_{m\leftarrow n} = \frac{\pi}{k_n^2}\sum_{\ell=0}^{\infty}(2\ell+1)\Big(1 - \big|S^{(\ell)}_{nn}\big|^2\Big). \tag{1.25}$$

We note that in the zero-energy limit, the cross sections are given by the s-wave ($\ell = 0$) partial wave and can be expressed in terms of a complex scattering length $a_n = \alpha_n - i\beta_n$ [4, 5, 6], namely $\sigma_n^{\rm elast} \approx 4\pi|a_n|^2$ and $\sigma_n^{\rm inel} \approx 4\pi\beta_n/k_n$, which exemplify the usual Wigner's threshold regime [5, 6, 7].

Chapter 2
Near Threshold Resonances

2.1 Introduction

A fundamental aspect of scattering is the appearance of resonances, which are rather ubiquitous, e.g., as shape resonances due to the centrifugal barrier in the entrance channel, or Feshbach resonances due to a quasi-bound state in a closed channel. Although their effect is often lost due to averaging at room temperatures or higher, they can become dominant features at low or ultralow temperatures, where only a few partial waves contribute to the scattering process. Since cold molecules were first predicted [8, 9] and observed experimentally [10, 11], rapid progress has been made in our ability to form and manipulate ultracold molecules [12, 13], which provides the seed to study in a precise and controlled fashion [14] the role of single partial waves, and state-to-state processes [15] in chemical systems. In fact, early experiments on KRb ultracold molecules [16, 17], which explored quantum-state controlled chemical reactions using quantum statistics, motivated several studies of chemical systems under extreme conditions, and particularly the role of resonances in controlling the outcome. This high level of control over interactions can be realized using Feshbach resonances [18], or by orienting ultracold molecules [17, 19]. In addition to investigations of degenerate quantum gases [20, 21], such control also allows studies of exotic three-body Efimov states [22, 23] or application to quantum information processing [24, 25, 26].

In this chapter we consider resonances occurring due to the existence of a quasi-bound state in the entrance channel of a scattering system. We first look at a few examples in single channel scattering, and explain the energy scaling due to these near threshold resonances (NTR) based on the properties of the Jost functions. We then employ a three-open channel model to illustrate the effect for higher partial waves ℓ up to f-wave ($\ell = 3$), and we end the discussion with the elastic case, where additional details are given on how long-range potentials affect the validity of our results.

The model potentials we are using in this chapter is illustrated in Fig. 2.2. Since the long range effect is of interest, we use an inverse power tail $\sim C_\alpha/R^\alpha$ with a hard wall at short range to analyze the scattering properties,

$$\begin{aligned} V(R) &= \infty,\ R <= R_{\rm wall}, \\ V(R) &= -\frac{1}{R^\alpha},\ R > R_{\rm wall}. \end{aligned} \tag{2.1}$$

For low energy scattering it is very convenient to use van der Waals units, namely $R_{\rm vdW}$ for length and $E_{\rm vdW} = \hbar^2/2\mu R_{\rm vdW}^2$ for energy, where μ is the reduced mass of the colliding particles. In general, for a potential behaving asymptotically as $V(r) \sim -C_\alpha r^{-\alpha}$, the van der Waals length scale is $R_{\rm vdW} = (2\mu C_\alpha/\hbar^2)^{\frac{1}{\alpha-2}}$. We will use van der Waals units throughout this chapter.

2.2 Near Threshold Resonances in Single Channel Scattering

2.2.1 Jost function for finite range potential

Jost functions can be understood as the energy dependent coefficients of regular solutions in a basis consists of asymptotic solutions. Jost functions encode most of the information of the two-body interaction; and physical quantities such as phase shift, cross section, can be expressed in terms of Jost functions. In this subsection,

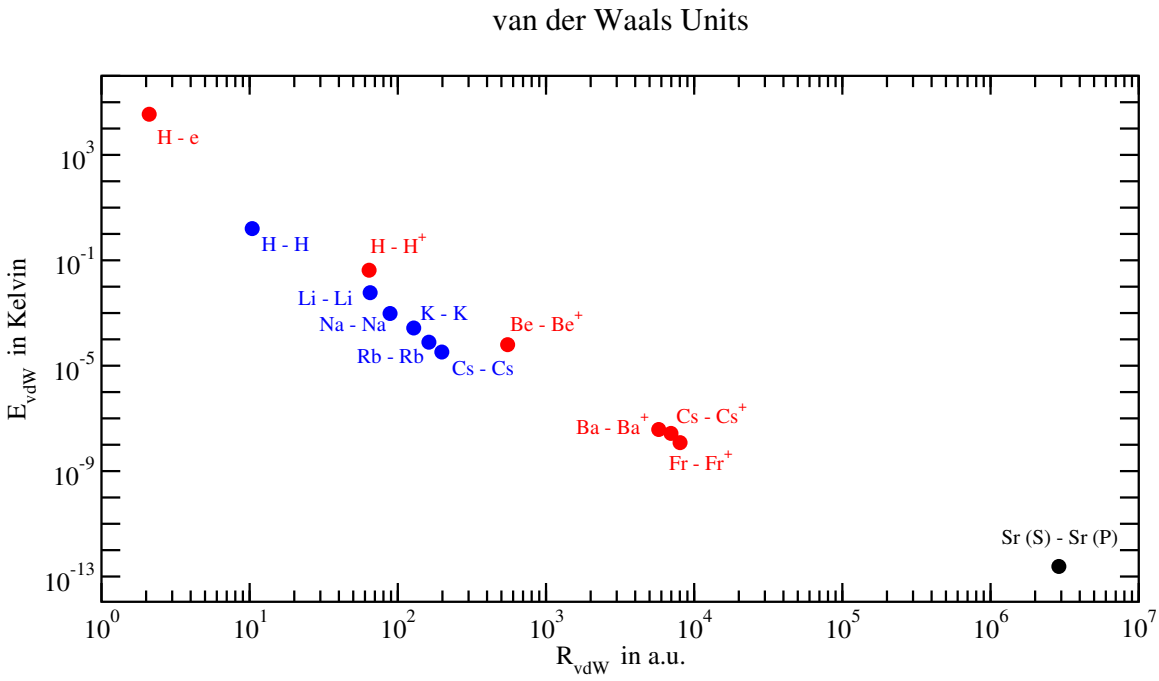

Figure 2.1. Van der Waals Units in a.u. and Kelvin.

we'll first investigate the case when the potential is finite, for which Jost functions are simple and easy to analyze.

The regular solution $\phi_k(R)$ is defined by imposing initial-value conditions at $\phi_k|_{R=0} = 0$, $\frac{d\phi_k}{dR}|_{R=0} = 1$, it can be expanded as [2],

$$\phi_{k,\ell}(R) = \phi_{0,\ell}(R) + k^2\xi_\ell(R) + k^4\xi_\ell(R) + ... \tag{2.2}$$

As a function of k, the regular solution is simply a power series of k^2. Asymptotically, the regular solution can be written as,

$$\phi_k = A_\ell(k)j_\ell(kr) + B_\ell(k)n_\ell(kr), \tag{2.3}$$

and alternatively,

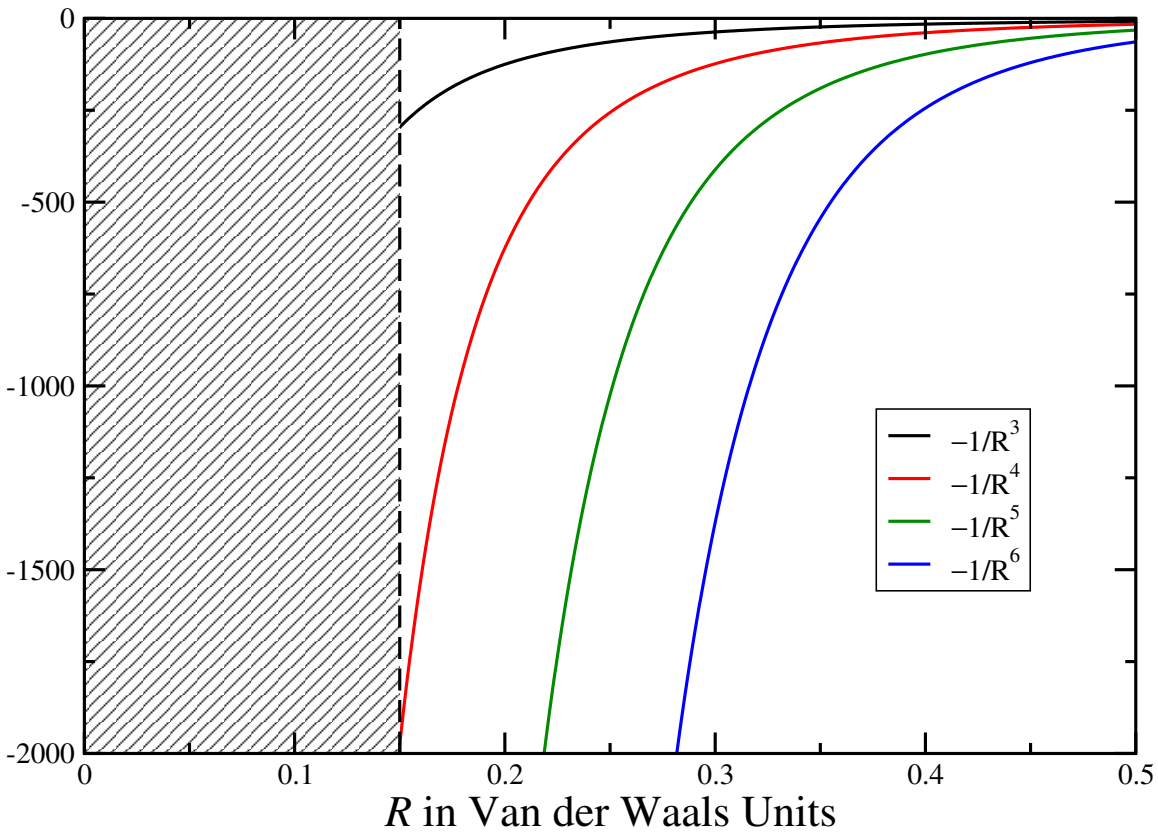

Figure 2.2. Model potentials used in this chapter. The potentials consist of two parts, a hard wall at short range and a long range tail that goes as $\sim C_\alpha/R^\alpha$. Since we use van der Waals units as described in main text, C_α is replaced with -1. The position of the hard wall is the tunable parameter to adjust the resonances.

$$\phi_k = \frac{1}{2ik^{\ell+1}}[F_\ell^* e^{ikR-\frac{\ell\pi}{2}} - F_\ell e^{-ikR-\frac{\ell\pi}{2}}]. \tag{2.4}$$

And the Jost Function can be defined as,

$$F = A - iB. \tag{2.5}$$

Thus, phase shift δ_ℓ and cross section σ_ℓ can be expressed in terms of $A(k)$ and $B(k)$,

$$\begin{aligned}
&\tan(\delta_\ell) = \frac{B_\ell}{A_\ell}, \\
&\sigma_\ell = 4\pi(2\ell+1)\frac{\sin^2(\delta_\ell)}{k^2} = \frac{4\pi(2\ell+1)}{k^2}\frac{B_\ell^2}{A_\ell^2+B_\ell^2}.
\end{aligned} \tag{2.6}$$

With the expansion of the regular solution Eq. (2.2), the derivation of the analytic form of $A_\ell(k)$ and $B_\ell(k)$ is straightforward,

$$\begin{aligned}
&k^{\ell+1}\phi_{k,\ell}(R_0) = Aj_\ell(kR_0) + Bn_\ell(kR_0), \\
&k^{\ell+1}\frac{d\phi_{k,\ell}}{dR}|_{R=R_0} = A\frac{dj_\ell}{dR}|_{R=R_0} + \frac{dBn_\ell}{dR}|_{R=R_0}.
\end{aligned} \tag{2.7}$$

Solving the linear equations, we obtain,

$$\begin{aligned}
A_\ell(k) &= k^{\ell+1}\frac{W[\phi_{k,\ell}, n_\ell]}{W[j_\ell, n_{ell}]}|_{R_0}, \\
B_\ell(k) &= k^{\ell+1}\frac{W[j_\ell, \phi_{k,\ell}]}{W[j_\ell, n_{ell}]}|_{R_0}.
\end{aligned} \tag{2.8}$$

Since $W[j_\ell, n_\ell] = -k$, and

$$\begin{aligned}
j_\ell(kR) &= \frac{(kR)^{\ell+1}}{(2\ell+1)!!}[1 + k^2(...) + k^4(...) + ...], \\
n_\ell(kR) &= \frac{(2\ell-1)!!}{(kR)^\ell}[1 + k^2(...) + k^4(...) + ...],
\end{aligned} \tag{2.9}$$

$A(k)$ and $B(k)$ can be expanded in the low-k limit as,

$$\begin{aligned}
A_\ell(k) &= A_\ell^{(0)} + A_\ell^{(2)}k^2 + A_\ell^{(4)}k^4 + ..., \\
B_\ell(k) &= k^{2\ell+1}[B_\ell^{(0)} + B_\ell^{(2)}k^2 + B_\ell^{(4)}k^4 + ...].
\end{aligned} \tag{2.10}$$

In the above equations, $A_\ell^{(n)}$ and $B_\ell^{(n)}$ are energy independent coefficients and they depend only on the potential. When there is a resonance or a bound state near

threshold, $A_\ell^{(0)}$ becomes vanishingly small and thus brings interesting near threshold resonance (NTR) effects.

As an example, we computed the Jost functions and cross sections for a finite potential,

$$\begin{aligned} &V(R) = \infty,\ R <= R_{\rm wall}, \\ &V(R) = -\frac{1}{R^3},\ R_{\rm wall} < R < R_0, \\ &V(R) = 0,\ R >= R_0, \end{aligned} \tag{2.11}$$

with $R_0 = 100 R_{\rm vdW}$, $\ell = 0$ and $R_{\rm wall}$ as the tunable parameter for adjusting the position of resonances. As we increase $R_{\rm wall}$, the depth of the well decreases and bound states are pushed up and become resonances. Fig. 2.3 depicts the typical energy dependence of $A(k),\ B(k)$ for a short range potential. The numerical result for the potential (2.11) is shown in Fig. 2.4. In the top panel, $A|_{E=10^{-16}} \approx A_0$ is plotted as a function of the tuning parameter, $R_{\rm wall}$, the position of the hard wall; the value oscillates around zero and when it is vanishingly small, the cross section has a very different behavior. The blue dots in the upper panel of Fig. 2.4 correspond to the blue curves in the lower panel and they represent non-resonant cases when there is no resonance near the threshold; the cross section directly transits from the high energy regime to the Wigner regime, which is flat. With the presence of near threshold resonances or quasi-bound states, equivalently $A^{(0)} \approx 0$, cross sections in the whole low energy regime are enhanced and a new regime appears between the high energy and Wigner regimes, shown by the slope of the red curves.

The NTR effect can be understood easily with Eq. (2.10). For the non-resonance cases where $A_\ell^{(0)}$ is far from zero, the leading terms of $A_\ell(k)$ is $A_\ell^{(0)}$ and $B_\ell^{(0)}k$ for $B_\ell(k)$, and according to Eq.(2.6), cross section is constant. However, when $A_\ell^{(0)} \approx 0$,

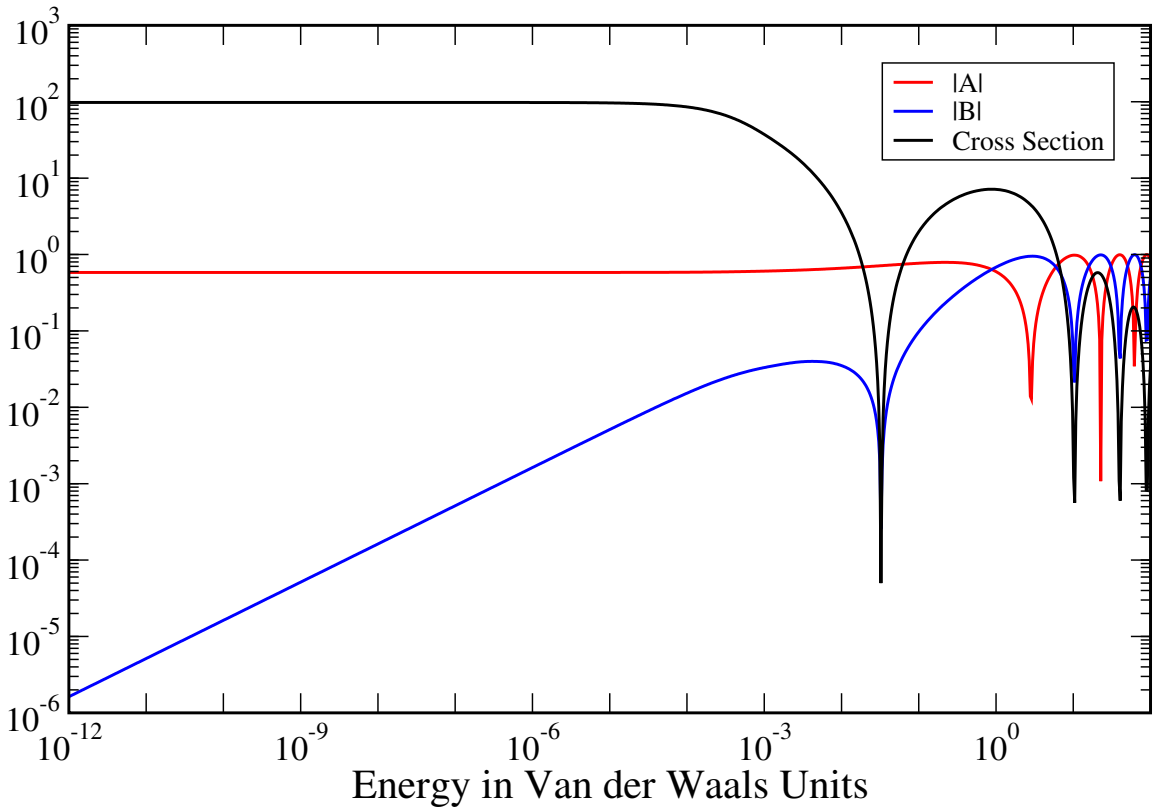

Figure 2.3. Typical behavior of $A(k)$ and $B(k)$ as function of energy for finite range potentials. Both $A(k)$ and the cross section tend to a constant for s-wave at the low-k limit, while $B(k) \sim k$.

leading terms of $A(k)$ becomes $A_\ell^{(2)} k^2$ while $B_\ell(k)$ is independent of $A_\ell^{(0)}$ and as a result cross section goes as k^{-2}.

The analysis for finite potentials is simple and similar analysis can be done with long range potentials, or specifically, potentials with inverse power tails.

2.2.2 Long range potential

When a potential is finite or vanishes very fast, only the energy dependence of $A(k)$ will be significantly affected NTRs; but for long range potentials, e.g. potentials in Fig. 2.2, both $A_\ell(k)$ and $B_\ell(k)$ are affected. According to Willner and Gianturco [27], the single-channel Jost function for a potential which behaves asymptotically

$(r \to \infty)$ as an inverse power $(V \sim r^{-\alpha})$ has the following k-dependence:

$$\begin{aligned} A_\ell(k) &= \tilde{A}_\ell(k) L^{AA}(k) + \tilde{B}_\ell(k) L^{AB}(k), \\ B_\ell(k) &= \tilde{B}_\ell(k) L^{BB}(k) + \tilde{A}_\ell(k) L^{BA}(k). \end{aligned} \tag{2.12}$$

$\tilde{A}(k)$ and $\tilde{B}(k)$ are analytic functions,

$$\begin{aligned} \tilde{A}(k) &= A^{(0)} + A^{(2)} k^2 + \cdots, \\ \tilde{B}(k) &= k^{2\ell+1} (B^{(0)} + B^{(2)} k^2 + \cdots), \end{aligned} \tag{2.13}$$

where we omit ℓ for simplicity. Note that $\tilde{A}(k)$ and $\tilde{B}(k)$ are of the same form as $A(k)$ and $B(k)$ for finite range potentials. The functions $L(k)$ in Eq. (2.12) contain the effect of the long-range tail, and can be expanded as power series (possibly including log-terms) [27], the coefficients $a,\ b,\ c,\ d,\ c',\ d'$ in the equations below are numerical constants independent of C_α. For the case when $n \neq 2\ell + 3$, the leading terms are

$$\begin{aligned} L^{AA} &\to 1 + a C_\alpha k^{\alpha-2} \log(k) + ..., \\ L^{BB} &\to 1 + b C_\alpha k^{\alpha-2} \log(k) + ..., \\ L^{AB} &\to c C_\alpha k^{\alpha-2} + c' C_\alpha^2 k^\alpha \log(k) + ..., \\ L^{BA} &\to d C_\alpha k^{\alpha-2} + d' C_\alpha^2 k^\alpha \log(k) + ... \end{aligned} \tag{2.14}$$

The functions $A(k)$ and $B(k)$ have leading terms,

$$\begin{aligned} B(k) &\to d(A_0 + A_2 k^2) C_\alpha k^{\alpha-2} + k^{2\ell+1} B_0, \\ A(k) &\to (A_0 + A_2 k^2) + c B_0 C_\alpha k^{2\ell+\alpha-1}, \end{aligned} \tag{2.15}$$

where we employ the simpler notation $A_s \equiv A^{(s)}$ and $B_s \equiv B^{(s)}$. For the case when $n = \ell + 3$, we have

$$
\begin{aligned}
L^{AA} &\to 1 + aC_\alpha k^{\alpha-2} + ..., \\
L^{BB} &\to 1 + bC_\alpha k^{\alpha-2} + ..., \\
L^{AB} &\to cC_\alpha k^{\alpha-2}\log(k) + c'C_\alpha k^{\alpha-2} + ..., \\
L^{BA} &\to dC_\alpha k^{\alpha-2}\log(k) + d'C_\alpha k^{\alpha-2} + ...
\end{aligned}
\tag{2.16}
$$

The corresponding $A(k)$ and $B(k)$ behave as

$$
\begin{aligned}
B(k) &\to d(A_0 + A_2k^2)C_\alpha k^{\alpha-2}\log k + k^{2\ell+1}B_0, \\
A(k) &\to (A_0 + A_2k^2) + cB_0C_\alpha k^{2\ell+\alpha-1}\log k.
\end{aligned}
\tag{2.17}
$$

Again, the parameter A_0 is closely related to near threshold resonances and since both $A(k)$ and $B(k)$ are dependent of A_0, the threshold energy dependence of the cross section becomes more interesting. We use the same model potentials as described in Sec. 2.1, except that the potentials now have long range tails up to infinite, instead of being finite range.

The first column in Fig. 2.5 shows numerical results for the case when $n = 4, \ell = 0$. Despite the long range tail $-1/R^{-4}$, the cross section looks very much like that of the short range potential in Fig. 2.4. According to Eq. (2.15), at ultra-cold limit $A(k) \approx A_0 + A_2k^2$, $B(k) \approx B_0k + dA_0C_\alpha k^2$, and consequently, $A^2(k) + B^2(k) \approx A_0^2 + B_0^2k^2 + 2A_0A_2k^2$. With the absence of near threshold resonance, $\sigma \approx \frac{4\pi}{k^2}\frac{B_0^2k^2}{A_0^2+B_0^2k^2} \approx \frac{4\pi B_0^2}{A_0^2}$ at the low-k limit. When there is a NTR effect, $A_0 \approx 0$ and $\sigma \approx \frac{4\pi}{k^2}\frac{\beta_0^2k^2}{(\alpha_2k^2)^2+\beta_0^2k^2} \approx \frac{4\pi}{k^2}$, which also explains the slope between the Wigner and higher energy regimes, the red curves in Fig. 2.4, since the leading terms of $A(k)$ and $B(k)$ are the same.

When $\ell \neq 0$, NTR will also result in shape resonances as we shall see in the next example for $n = 3, \ell = 1$. Again, we expand the Jost function in the ultra cold limit according to Eq. (2.15), $A(k) \approx A_0 + A_2k^2$, $B(k) \approx dA_0C_\alpha k + dA_2C_\alpha k^3 + B_0k^3$, so that $A^2(k) + B^2(k) \approx A_0^2 + d^2A_0^2C_\alpha^2k^2 + 2A_0A_2k^2 + A_2^2k^4 + 2d^2A_0A_2C_\alpha^2k^4$, thus

$\sigma \approx \frac{12\pi}{k^2}\frac{A_0^2C_\alpha^2k^2}{A_0^2+A_0^2C_\alpha^2k^2} \approx 12\pi C_\alpha^2$ for the non-resonant case. Eliminating terms with A_0 gives us,

$$\sigma = \frac{12\pi}{k^2}\frac{(B_0+A_2C_\alpha)^2k^6}{A_2^2k^4+(B_0+A_2C_\alpha)^2k^6} \approx 12\pi\big[\frac{B_0+A_2C_\alpha}{A_2}\big]^2, \tag{2.18}$$

which indicates that in the NTR regime the cross section is also constant as in the Wigner regime, but with a different value, as shown in Fig. 2.5 second column. Unlike the case when $\ell = 0$, a sharp peak appears between the NTR regime and Wigner regime. This can also be explained with leading terms of $A(k)$ and $B(k)$. In the s-wave case, the leading term of $A^2(k)+B^2(k) \approx A_0^2+B_0^2k^2+2A_0A_2k^2$ transits from A_0^2 to $B_0^2k^2$ where $k \sim A_0$, but the leading term of $B(k)$ is always $B_0^2k^2 \sim k^2$. While in the p-wave case, the leading term of $A^2(k)+B^2(k) \approx A_0^2+d^2A_0^2C_\alpha^2k^2+2A_0A_2k^2+A_2^2k^4+2d^2A_0A_2C_\alpha^2k^4$ transits from A_0^2 to $A_2^2k^4$, with the transition taking place near $k \sim |A_0|^{\frac{1}{2}}$. If A_0 and A_2 have different signs, the leading term of $A^2(k)+B^2(k)$ becomes of the order k^6 since $A^2(k) \sim A_4^2k^8$ and $B^2(k) \sim (A_0k+B_0k^3)^2 \sim (k^2k+B_0k^3)^2 \sim k^6$. Thus during the transition, denominator decreases significantly, which gives the peak of shape resonances. When A_0 and A_2 have the same sign, the leading term of $A^2(k)+B^2(k)$ during the transition will always be around k^4 and no peak will be present. Numerical results for $n = 6, \ell = 1$ shown as the dashed line in the third column of Fig. 2.5 includes an example with a quasi-bound state near the threshold instead of NTR. The overall enhancement and NTR regime of the cross section still persist but the shape resonance peak is absent. Using the same analysis as done in the cases of $n = 4, \ell = 0$ and $n = 3, \ell = 1$, the energy dependence of cross section in Wigner and NTR regimes can be easily derived, when no resonance is present, as

$$\sigma = \frac{12\pi}{k^2}\frac{B_0^2k^6}{A_0^2+B_0^2k^6} \approx 12\pi(\frac{B_0}{A_0})^2k^4, \tag{2.19}$$

and with the NTR effect, as

$$\sigma = \frac{12\pi}{k^2}\frac{B_0^2 k^6}{A_2^2 k^4 + B_0^2 k^6} \approx \ 12\pi\big[\frac{B_0}{A_2}\big]^2. \tag{2.20}$$

Another interesting new regime appears between the NTR regime and the Wigner regime, for cases such as $n = 4, \ell = 1$ and $n = 6, \ell = 2$, as we shall see next. We name the new regime the Effective Wigner regime.

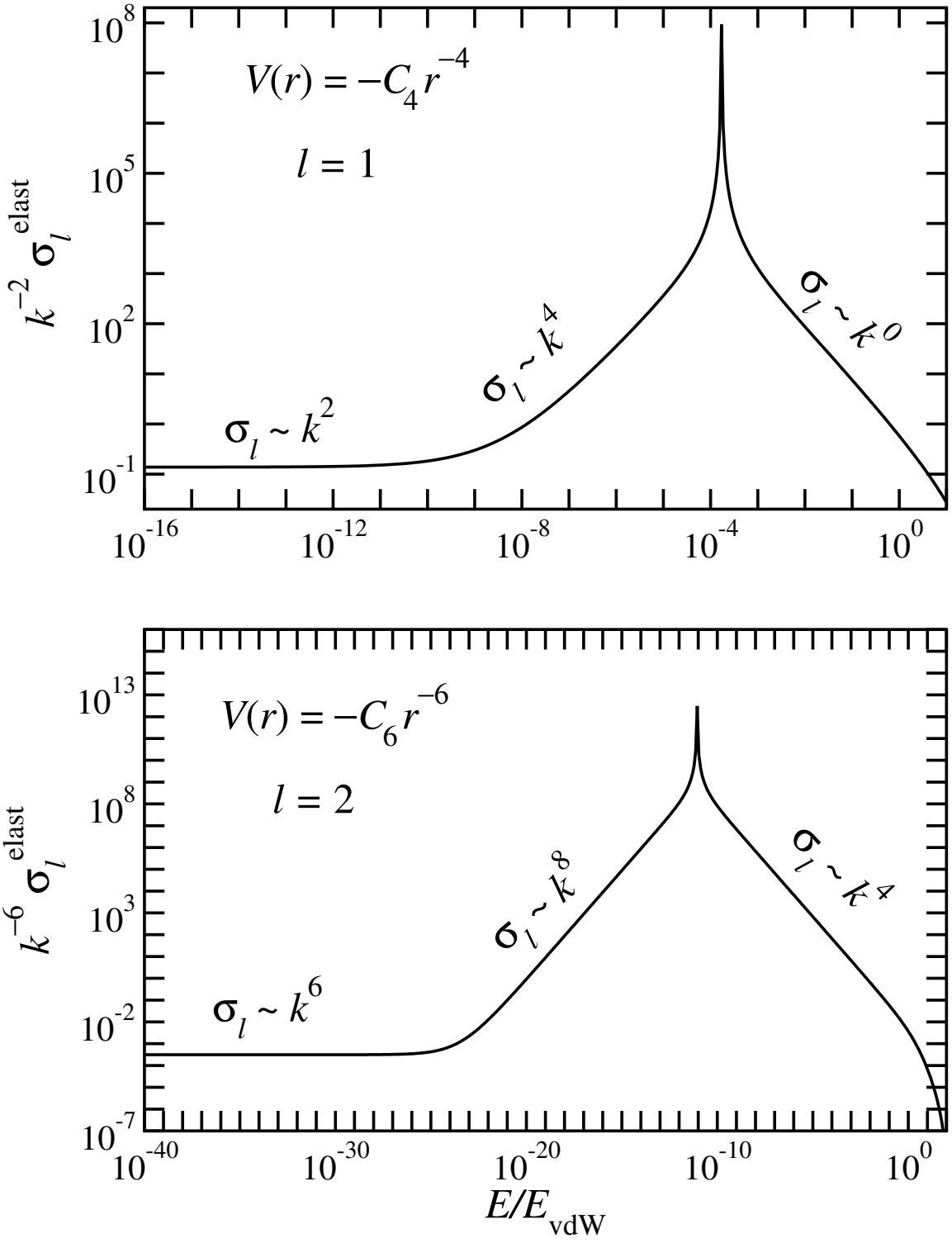

Figure 2.6. The partial wave contribution to the elastic cross section for the critical cases $\ell = 1$ with $\alpha = 4$ and $\ell = 2$ with $\alpha = 6$. The true Wigner regime behavior ($k^{2\alpha-6}$) was factored out, to better illustrate the three distinct regimes, but the k-dependence of σ^{elast} itself is indicated for each regime.

Following Eq. (2.15), we obtain the following expansions,

$$\begin{aligned} A(k) &\approx A_0 + A_2 k^2, \\ B(k) &\approx A_0 d C_\alpha k^{\alpha-2} + B_0 k^{2\ell+1}. \end{aligned} \tag{2.21}$$

For $\ell < \frac{\alpha-3}{2}$, the dominant term for $B(k)$ is $B_0 k^{2\ell+1}$ (just as in the case of a short-range potential), and the threshold behavior of $\sigma^{\rm elast}$ (including possible NTR effects) is as shown for $n = 4, \ell = 1$ and $n = 6, \ell = 1$. However, for $\ell > \frac{\alpha-3}{2}$, the dominant term for $B(k)$ will be $A_0 k^{\alpha-2}$. Consequently, when A_0 is vanishingly small, both $A(k)$ and $B(k)$ will lose their dominant term simultaneously, and both the denominator and the numerator in the expression (2.6) for the elastic cross section are now sensitive to NTR effects. In particular, for any given inverse power α, there will be a partial wave ℓ such that both terms ($A_0 k^{\alpha-2}$ and $B_0 k^{2\ell+1}$) compete in Eq. (2.21) for $B(k)$ at low k. In such a case, the corresponding partial-wave contribution to the elastic cross section can have a rather surprising threshold behavior, as illustrated in Fig. 2.6 for $\ell = 1$ with $\alpha = 4$, and for $\ell = 2$ with an $\alpha = 6$ inverse-power potentials.

Fig. 2.6 shows the threshold behavior of the quantity $k^{6-2\alpha}\sigma_\ell^{\rm elast}$ for two critical cases: $\ell = 1$ with $\alpha = 4$, and $\ell = 2$ with $\alpha = 6$. Although one recovers the expected behavior $\sigma^{\rm elast} \sim k^{2\alpha-6}$ for $k \to 0$, this true Wigner regime is displaced to exceedingly low energies, which are practically inaccessible. There is instead an intermediate regime between the NTR and the true Wigner regimes, which we refer to as the *effective* Wigner regime. The appearance of three distinct regimes can be explained by the low-k behavior of the Jost function in Eq. (2.21). For $\ell = 1$ and $\alpha = 4$, we have

$$\begin{aligned} A(k) &\approx A_0 + A_2 k^2, \\ B(k) &\approx A_0 d C_4 k^2 + B_0 k^3, \end{aligned} \tag{2.22}$$

and using Eq. (2.6), the numerical results in Fig. 2.6 are readily understood. Indeed, the denominator $A^2 + B^2$ in Eq. (2.6) is dominated by $A(k)$ at low k, and hence the position of the shape resonance is the value of k where $A(k)$ vanishes, $k_{\rm res} = |A_0 A_2^{-1}|^{\frac{1}{2}}$, which marks the transition between the NTR and the effective Wigner regimes. On the other hand, the transition between the effective and true Wigner regimes is dictated by the behavior of $B(k)$. Namely, this transition takes place near the values of k where the two terms in Eq. (2.22) have the same absolute value, i.e., $k_{\rm eff} = |A_0 d C_4 B_0^{-1}|$. It is thus clear that $k_{\rm eff}$ approaches the threshold much faster than $k_{\rm res}$ when $A_0 \to 0$, and the true Wigner regime almost disappears into the deep ultracold regime. Therefore the significant difference between $k_{\rm eff}$ and $k_{\rm res}$ opens a window with abnormal energy scaling between Wigner and NTR regimes. Similarly, for $\alpha = 6$ and $\ell = 2$, we have

$$\begin{aligned} A(k) &\approx A_0 + A_2 k^2, \\ B(k) &\approx A_0 d C_6 k^4 + B_0 k^5, \end{aligned} \tag{2.23}$$

and $k_{\rm eff} \sim |A_0|$ approaches the threshold faster than $k_{\rm res} \sim |A_0|^{\frac{1}{2}}$ when $A_0 \to 0$, just as in the previous case.

So far we have discussed the NTR effect when $n \neq 2\ell + 3$, and the analysis is very similar for $n = 2\ell + 3$, except the terms with $k^{m_1} \log^{m_2}(k)$ could be dominate and these terms are responsible for the well-known logarithmic energy dependence of cross section for $n = 3, \ell = 0$.

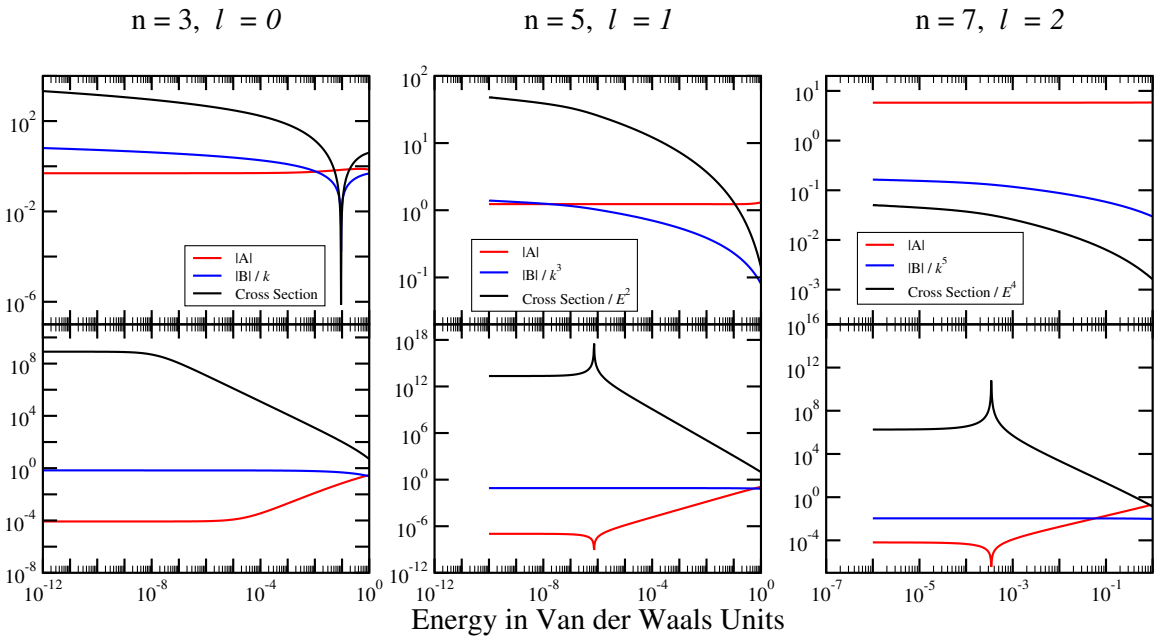

Figure 2.7. Results for the case $n = 2\ell + 3$.

As shown in top panels of Fig. 2.7, cross sections for $n = 3, \ell = 0$, $n = 5, \ell = 1$ and $n = 7, \ell = 2$ behave as $\log^2(k)$, $k^4 \log^2(k)$ and $k^8 \log^2(k)$ respectively. However, with a NTR effect, not only a new regime appears, the "Wigner regime" seems to lose the logarithmic behavior to become the same as for $n \neq 2\ell + 3$. In other words, the NTR effect reduces the long range effect of the potential. A detailed analysis for $n = 3, \ell = 0$ is demonstrated below, it is very similar for the other two cases.

Using Eq. (2.17), $A(k)$ and $B(k)$ can be expanded as, $A(k) \approx A_0 + cB_0C_\alpha k^2 \log(k)$, $B(k) \approx dA_0C_\alpha k \log(k) + B_0 k$. In the Wigner regime, $A(k) \sim A_0$, $B(k) \sim dA_0C_\alpha k \log(k)$ and in turn $\sigma \approx\approx 4\pi C_n^2 (\log k)^2$. When A_0 is vanishingly small, $A^2(k) + B^2(k) \approx B_0^2 k^2$ and $B(k) \approx B_0 k$, so the cross section has an energy dependence of $\sim k^{-2}$ shown as the NTR regime in the lower panels of Fig. 2.7. As we lower the energy and move gradually from the NTR regime towards the Wigner regime, A_0^2 becomes dominant with $k \sim |A_0/B_0|$, and $dA_0C_\alpha k \log(k)$ becomes dominate where $k \sim \exp[-|B_0/(dA_0C_\alpha)|]$, which is much smaller than $|A_0/B_0|$ when A_0 is small. Therefore, before the cross

section reaches the real Wigner regime where $k \sim dA_0C_\alpha k\log(k)$ dominates in the expansion of $B(k)$, $B(k) \sim B_0k$, $A^2(k) + B^2(k) \sim A_0^2$, which gives a constant cross section in finite range potential case. Again the abnormal new regime can be interpreted as due to the large difference between $k_{\rm eff}$ and $k_{\rm res}$, as in the case of $n = 4, \ell = 1$ and $n = 6, \ell = 2$.

For high partial waves, $B(k)$ in Eq. (2.12) will be dominated by the anomalous term $L^{BA}(k)\tilde{A}(k) \approx dC_\alpha k^{\alpha-2}(A_0 + A_2k^2)$. Thus, irrespective of A_0 being small or large, we have

$$\sigma_{\ell=\rm high}^{\rm elast} \sim \left[\frac{dC_\alpha k^{\alpha-3}(A_0 + A_2k^2)}{A_0 + A_2k^2}\right]^2 \sim k^{2\alpha-6}, \tag{2.24}$$

which is valid for $\ell > \frac{\alpha-3}{2}$. The threshold behavior is no longer affected by a shape resonance, and the Wigner regime covers the entire domain of low energy, see bottom panel in Fig. 2.10. If the resonance becomes bound (just below the threshold) the spike disappears, and there are no resonant effects whatsoever.

2.3 Near Threshold Resonances in Multi-Channel Scattering

2.3.1 Jost function formula

Jost functions are useful in the analysis of single channel scattering and also give insight into multi-channel problems as we shall see in this section. For N coupled channels, the regular solution $\mathbf{\Phi}^{(\ell)}(r)$ is defined as an $N\times N$ matrix obeying Eq. (1.12). The components $\phi_{mn}^{(\ell)}$ satisfy the boundary condition $\phi_{mn}^{(\ell)}(r) \sim \delta_{mn}r^{\ell+1}$ as $r \to 0$; more specifically, assuming the potential elements $U_{mn}(r)$ are less singular than r^{-2} at the origin, we impose the initial condition

$$\phi_{mn}^{(\ell)}(r) \xrightarrow{r\to0} \delta_{mn}\, s_\ell(k_mr). \tag{2.25}$$

The asymptotic behavior of $\phi^{(\ell)}_{mn}$ can be written as

$$\phi^{(\ell)}_{mn}(r) \xrightarrow{r\to\infty} s_\ell(k_m r) A^{(\ell)}_{mn} + c_\ell(k_m r) B^{(\ell)}_{mn}, \tag{2.26}$$

where $s_\ell(x) = x j_\ell(x) \sim \sin(x - \ell\frac{\pi}{2})$ and $c_\ell(x) = -x y_\ell(x) \sim \cos(x - \ell\frac{\pi}{2})$ are the Riccati–Bessel and Riccati–Neumann functions, respectively. We recast Eq. (2.26) in terms of the free-particle solutions $c_\ell \pm i s_\ell \sim e^{\pm i(x-\ell\pi/2)}$, namely

$$\begin{aligned}\phi^{(\ell)}_{mn}(r) \xrightarrow{r\to\infty} \frac{i}{2}\big[&\big(A^{(\ell)}_{mn} - iB^{(\ell)}_{mn}\big)e^{-i(k_m r-\ell\pi/2)} \\ &- \big(A^{(\ell)}_{mn} + iB^{(\ell)}_{mn}\big)e^{+i(k_m r-\ell\pi/2)}\big], \qquad (2.27)\\ \equiv \frac{i^{\ell+1}}{2}\big[&\mathcal{J}^{(\ell)}_{mn} e^{-ik_m r} - (-1)^\ell \mathcal{J}^{(\ell)*}_{mn} e^{+ik_m r}\big], \qquad (2.28)\end{aligned}$$

and we identify the Jost matrix elements,

$$\mathcal{J}^{(\ell)}_{mn} \equiv A^{(\ell)}_{mn} - iB^{(\ell)}_{mn}. \tag{2.29}$$

We now rewrite the asymptotic behavior (2.28) in matrix form,

$$\mathbf{\Phi}^{(\ell)}(r) \xrightarrow{r\to\infty} \frac{i^{\ell+1}}{2}\big[e^{-i\mathbf{K}r}\boldsymbol{\mathcal{J}}_\ell - (-1)^\ell e^{i\mathbf{K}r}\boldsymbol{\mathcal{J}}^*_\ell\big], \tag{2.30}$$

which we multiply by $i^\ell \boldsymbol{\mathcal{J}}^{-1}_\ell \mathbf{C}(\mathbf{K})$ on the right, and compare with Eq. (1.16) to find the physical solution,

$$\mathbf{\Psi}^{(\ell)} = i^\ell \mathbf{\Phi}^{(\ell)} \boldsymbol{\mathcal{J}}^{-1}_\ell \mathbf{C}(\mathbf{K}), \tag{2.31}$$

and the S-matrix,

$$\mathbf{S}^{(\ell)} = \mathbf{K}^{1/2} \boldsymbol{\mathcal{J}}^*_\ell \boldsymbol{\mathcal{J}}^{-1}_\ell \mathbf{K}^{-1/2}. \tag{2.32}$$

In the formalism presented here we assumed that neither the target nor the projectile have any internal rotational degrees of freedom, in order to focus on the orbital angular momentum ℓ of the relative motion, which is responsible for the shape resonances that will produce NTR effects.

2.3.2 Numerical results

2.3.2.1 Model potentials

For a systematic investigation of near-threshold shape resonances in high partial waves, we employ a simple model which incorporates the key ingredients of coupled-channel scattering. This will allow for easy tuning of NTRs. We shall illustrate the effects of NTRs on cross sections for partial waves s, p, d, f.

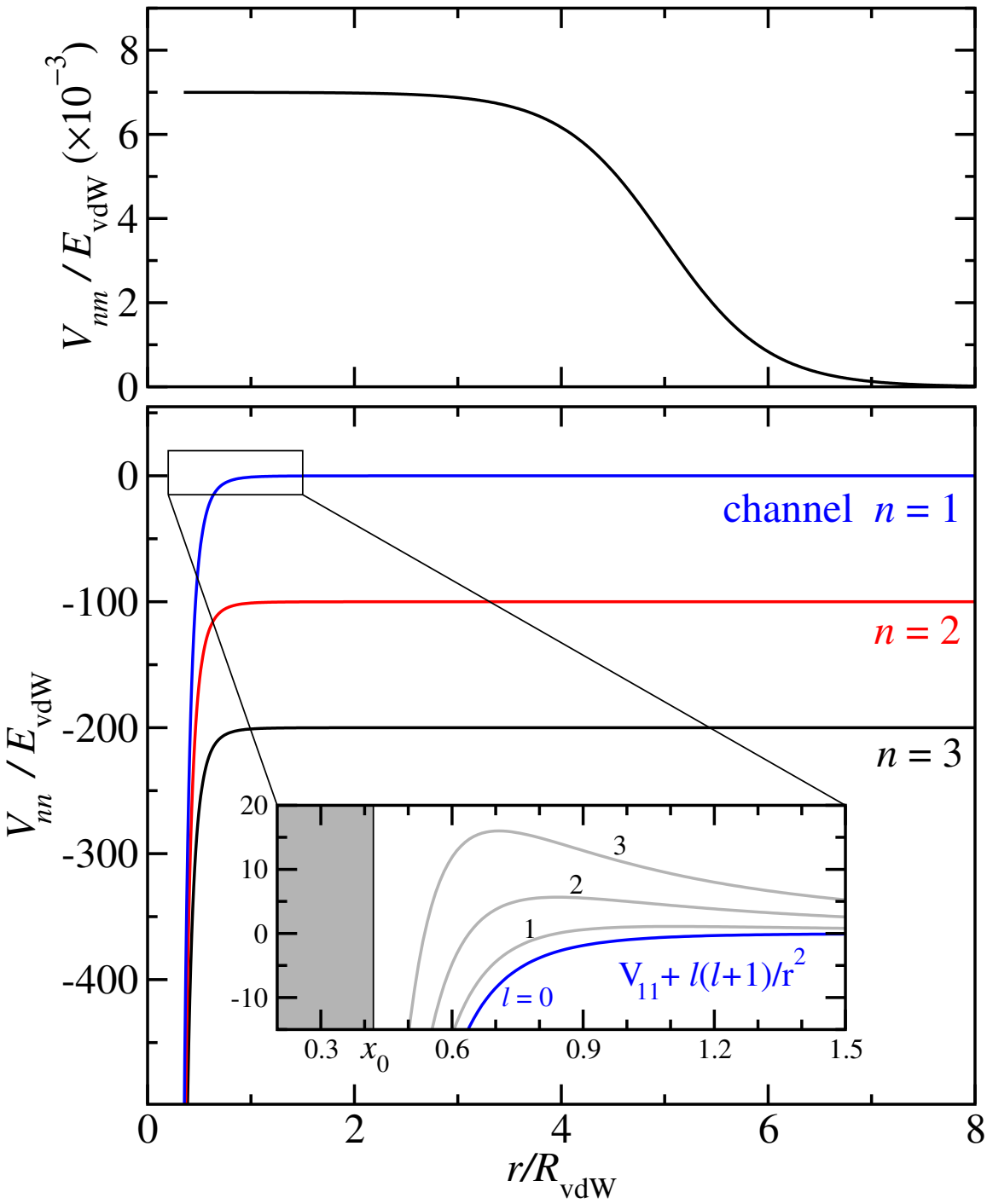

Figure 2.8. Upper panel: coupling potentials used in our three-channel model, see Eq. (2.34). Lower panel: diagonal potentials, see Eq. (2.33). The inset shows the effective potential in the entrance channel, including the centrifugal term, for $\ell = 0, 1, 2, 3$.

Fig. 2.8 depicts the potentials V_{nm} used in our model. There are three channels (all open) with identical attractive diagonal potentials $V_{nn}(r) = -C_6/r^6$, and a hard wall is placed at short range. The position r_0 of the hard wall was tuned for each partial wave to bring a shape resonance near the threshold of the entrance channel $n = 1$, just as in the single channel case in Sec. 2.2. We also use the van der Waals units as described in Sec. 2.1. Using the dimensionless variable $x \equiv r/R_{\rm vdW}$, the diagonal potentials read

$$\frac{V_{nn}(x)}{E_{\rm vdW}} = \begin{cases} +\infty, & r < r_0, \\ -x^{-6}, & r > r_0, \end{cases} \tag{2.33}$$

and the off-diagonal couplings (which are all identical) are given by

$$\frac{V_{nm}(x)}{E_{\rm vdW}} = \frac{0.007}{1 + e^{2x-10}}. \tag{2.34}$$

The channel threshold energies E_n are

$$\frac{E_n}{E_{\rm vdW}} = \begin{cases} 0, & n = 1, \\ -100, & n = 2, \\ -200, & n = 3, \end{cases} \tag{2.35}$$

with $n = 1$ being the entrance channel. The locations of the hard wall for each partial wave ℓ are

$$\frac{r_0}{R_{\rm vdW}} = \begin{cases} 0.42402677, & \ell = 0, \\ 0.37845091, & \ell = 1, \\ 0.34646173, & \ell = 2, \\ 0.32219300, & \ell = 3, \end{cases} \tag{2.36}$$

adjusted in order to bring a shape resonance near the threshold of the entrance channel ($n = 1$) for each of the partial waves ($\ell \equiv \ell_1 \leq 3$) studied here . Except for the entrance channel, we used $\ell_2 = \ell_3 = 0$ in channels $n = 2, 3$.

2.3.2.2 Numerical results of inelastic cross sections

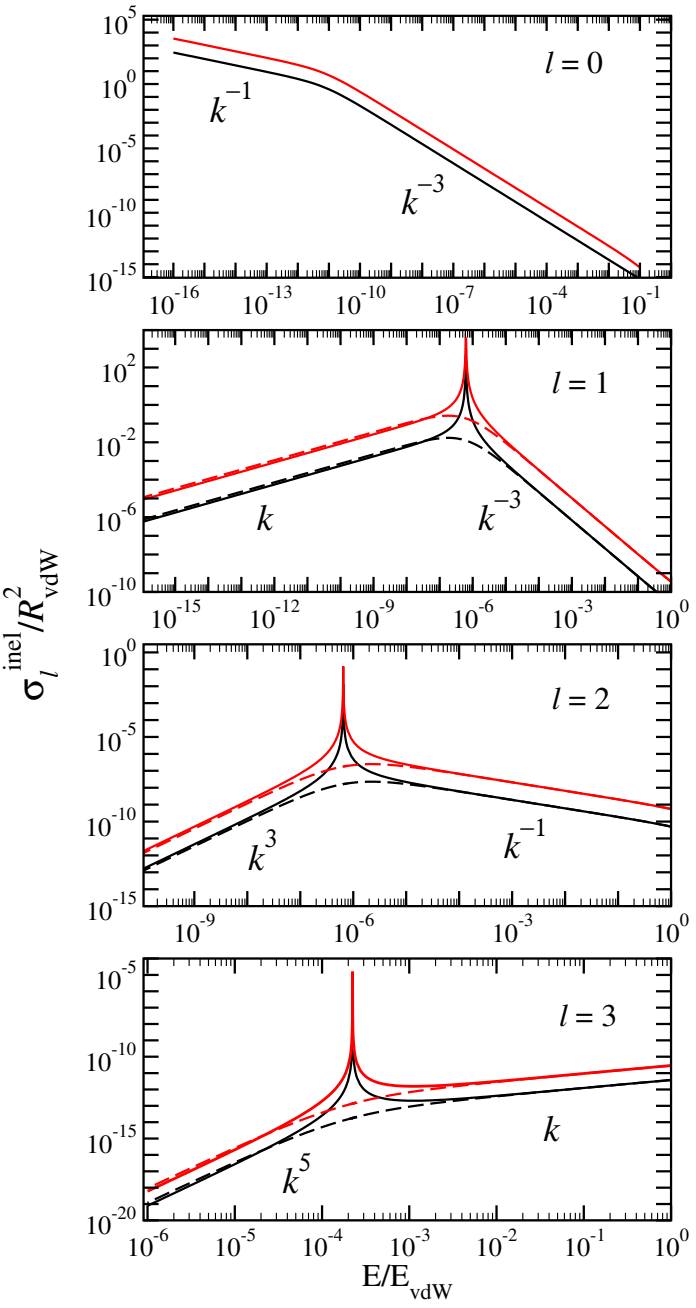

Figure 2.9. Energy dependence of the partial inelastic cross sections for $\ell = 0, 1, 2, 3$. Red and black curves correspond to final channels $f = 2$ and $f = 3$, respectively. Full lines for shape resonance just above the threshold, dashed lines for quasi-bound resonances just below the threshold.

We computed $\sigma_{f\leftarrow 1}^{\mathrm{inel}(\ell)}$ for $\ell = 0, 1, 2, 3$, for final channels $f = 2, 3$, and the results shown in Fig. 2.9 demonstrate that the partial inelastic cross sections for both final channels follow the same behavior, except for their different overall magnitudes. As indicated in each panel in Fig. 2.9, the various power-laws displayed by $\sigma_{f\leftarrow 1}^{\mathrm{inel}(\ell)}(k)$ for both the Wigner and NTR regimes are in agreement with Eq. (2.59) and (2.59) for $\ell = 0$ and $\ell \geq 1$, respectively. The full curves in Fig. 2.9 correspond to the case of a shape resonance just above the threshold, while the dashed curves correspond to the case of a quasi-bound state lying just bellow the threshold. In the former case, the sharp resonant peaks mark the transition between the Wigner and NTR regimes; the narrow widths of the shape resonances are mostly due to slow tunneling through the centrifugal barrier. In the latter case, the transition between the two regimes is rather gradual, as shown by the dashed curves in Fig. 2.9. The absolute value of the binding energy of the quasi-bound resonance corresponds to the transition between the Wigner and NTR regimes.

2.3.2.3 Numerical results of elastic cross sections

While the threshold behavior (including both NTR and Wigner regimes) of the inelastic cross sections is unaffected by the long-range nature of the diagonal potential in the entrance channel, the elastic cross section at low energy can be altered significantly.

Indeed, for single-channel scattering it is well known that the low-energy behavior of the phase-shift δ_ℓ in partial wave ℓ depends on the asymptotic behavior of the potential; e.g., if $V(r) \sim r^{-\alpha}$ when $r \to \infty$, we have the threshold behavior $\delta_\ell(k) \sim k^{\alpha-2}$ for $\ell > \frac{\alpha-3}{2}$, while the "normal" behavior $\delta_\ell(k) \sim k^{2\ell+1}$ is only valid for $\ell < \frac{\alpha-3}{2}$. Accordingly, the threshold behavior for the partial elastic cross section is $\sigma_\ell^{\mathrm{elast}}(k) \sim$

$k^{2\alpha-6}$ for $\ell > \frac{\alpha-3}{2}$, and $\sigma_\ell^{\rm elast}(k) \sim k^{4\ell}$ for $\ell < \frac{\alpha-3}{2}$. However, if a shape resonance is very close to the threshold, it can affect the low energy behavior in a surprising way.

Fig. 2.10 shows the partial elastic cross sections for our three-channel model. For $\ell = 0$ and $\ell = 1$, we find the "normal" behavior for both the Wigner and NTR regimes, see Eqs. (2.61) and (2.63). For $\ell = 2$ the behavior $\sigma_\ell^{\rm elast} \sim k^8$ in Fig. 2.10 also follows Eq. (2.63), even though Wigner's threshold law dictates $\sigma_\ell^{\rm elast} \sim k^{2\alpha-6} = k^6$ for $\ell > \frac{3}{2}$ (recall that $\alpha = 6$ is the inverse power for our diagonal potential). The unexpected behavior $\sigma_\ell^{\rm elast} \sim k^8$ for $\ell = 2$ in Fig. 2.10 can be understood in terms of the single-channel Jost function for a potential behaving asymptotically as an inverse power, $V(r) \sim r^{-\alpha}$, As described in the previous Sec. 2.2.

For $\ell = 3$ (bottom panel in Fig. 2.10), the Wigner regime behavior is the expected one for a long-range potential, but the NTR regime behavior is surprisingly the same as Wigner's law. Hence, the two regimes can no longer be considered as distinct energy domains, and the contribution of partial wave $\ell = 3$ to the scattering process is practically unaffected by the very sharp resonance.

As is well known, inter-atomic potentials do not behave asymptotically as a single inverse power term, $V \sim r^{-\alpha}$, but instead they have a long-range expansion containing several such terms, e.g., $V(r) \approx -\frac{C_6}{r^6} - \frac{C_8}{r^8} - \frac{C_{10}}{r^{10}}$. Although this general (and more realistic) case can be easily tackled numerically, it is less amenable to a theoretical approach. Indeed, threshold behavior has been studied mostly for the simplified case of long-range interaction of the type $V(r) = C_\alpha/r^\alpha$ [27, 28, 29, 30]. Typically, the term with the lowest inverse power is dominant and will dictate threshold behavior; thus we expect our analysis will remain valid in the general case. However, in the unusual case when C_6 is exceedingly small, threshold behavior may be affected by an interplay between two or more terms in the asymptotic expansion of $V(r)$.

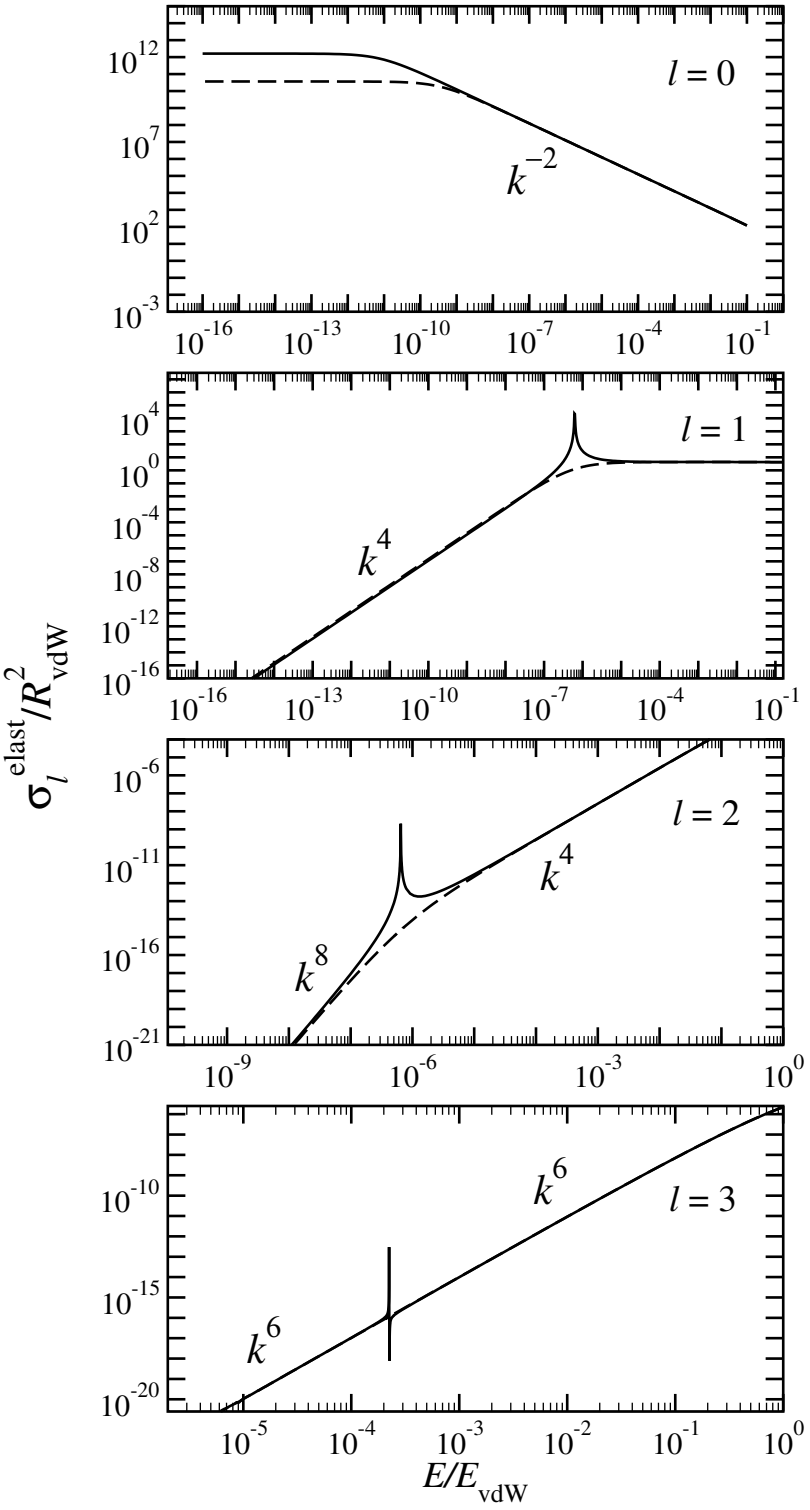

Figure 2.10. Same as Fig. 2.9 for the elastic cross section.

2.3.3 Multi-channel NTR effects explained with Jost function

In order to explain the appearance of the NTR regime we make use of the properties of the S-matrix, which in turn is expressed in Eq. (2.32) in terms of the Jost function. The inverse of the Jost matrix in Eq. (2.32) can be written explicitly,

$$\boldsymbol{\mathcal{J}}^{-1} = \frac{1}{\det(\boldsymbol{\mathcal{J}})} \left(\mathrm{Cof}(\boldsymbol{\mathcal{J}}) \right)^T, \tag{2.37}$$

with $[\mathrm{Cof}(\boldsymbol{\mathcal{J}})]^T$ the transpose of the cofactor matrix of $\boldsymbol{\mathcal{J}}$, and $\det(\boldsymbol{\mathcal{J}})$ the determinant of $\boldsymbol{\mathcal{J}}$. Thus, we rewrite the matrix element $S_{fi}^{(\ell)}$ for the partial cross section $\sigma_{f\leftarrow i}^{(\ell)}$ in Eq. (1.23) as

$$\begin{aligned} S_{fi} &= \frac{k_f^{\frac{1}{2}} k_i^{-\frac{1}{2}}}{\det(\boldsymbol{\mathcal{J}})} \left(\boldsymbol{\mathcal{J}}^* \left[\mathrm{Cof}(\boldsymbol{\mathcal{J}})\right]^T \right)_{fi}, \\ &= \frac{k_f^{\frac{1}{2}} k_i^{-\frac{1}{2}}}{\det(\boldsymbol{\mathcal{J}})} \sum_j \mathcal{J}_{fj}^* C_{ij}, \end{aligned}$$

where the partial-wave superscript (ℓ) was omitted, and $C_{ij} = [\mathrm{Cof}(\boldsymbol{\mathcal{J}})]_{ij}$ are the cofactors of $\boldsymbol{\mathcal{J}}$. Eq. (2.29) yields $\mathcal{J}_{fj}^* = \mathcal{J}_{fj} + 2iB_{fj}$, and we have

$$\begin{aligned} \sum_j \mathcal{J}_{fj}^* C_{ij} &= \sum_j \mathcal{J}_{fj} C_{ij} + 2i \sum_j B_{fj} C_{ij}, \\ &= \delta_{fi} \det(\boldsymbol{\mathcal{J}}) + 2i \sum_j B_{fj} C_{ij}, \end{aligned} \tag{2.38}$$

where we used the properties of a determinant in terms of cofactors. The matrix element S_{fi} now reads

$$S_{fi} = \delta_{fi} + 2i \, \frac{k_f^{\frac{1}{2}} k_i^{-\frac{1}{2}}}{\det(\boldsymbol{\mathcal{J}})} \sum_j B_{fj} C_{ij},$$

which yields the element T_{fi} of the T-matrix,

$$T_{fi} = -2i \, \frac{k_f^{\frac{1}{2}} k_i^{-\frac{1}{2}}}{\det(\boldsymbol{\mathcal{J}})} \sum_j B_{fj} C_{ij}.$$

Thus, the partial cross section $\sigma^{(\ell)}_{f\leftarrow i}$ in Eq. (1.23) reads

$$\sigma_{f\leftarrow i} = \frac{\pi}{k_i^2}|T_{fi}|^2 = 4\pi k_f k_i^{-3}\left|\frac{\sum_j B_{fj}C_{ij}}{\det(\boldsymbol{\mathcal{J}})}\right|^2 . \tag{2.39}$$

Assuming a resonance exists and is due to a quasi-bound state in the entrance channel, i, we separate its contribution and write the determinant as

$$\det(\boldsymbol{\mathcal{J}}) = \sum_n \mathcal{J}_{in}C_{in} = C_{ii}(\mathcal{J}_{ii} + \mathsf{j}_{ii}), \tag{2.40}$$

where

$$\mathsf{j}_{ii} \equiv \frac{1}{C_{ii}}\sum_{n\neq i}\mathcal{J}_{in}C_{in} \ . \tag{2.41}$$

The denominator $|\det(\boldsymbol{\mathcal{J}})|^2$ in Eq. (2.39) can now be written as

$$|\det(\boldsymbol{\mathcal{J}})|^2 = |C_{ii}|^2|D|^2, \qquad D \equiv \mathcal{J}_{ii} + \mathsf{j}_{ii} \ . \tag{2.42}$$

We emphasize that the cofactor C_{ii} includes all but the entrance channel and, based on the assumption that the resonance is in the entrance channel, $C_{ii}(k_i)$ is a well-behaved function almost independent of k_i as $k_i \to 0$ [31]. We shall see that the effect of the resonance is accounted for in $D(k_i)$, mostly via the $\mathcal{J}_{ii}$ contribution. For clarity, we label the entrance channel defining the threshold for the scattering energy by $i = 1$, and simply adopt the notation $k_i = k_1$ and $\ell_i = \ell_1$, such that the partial cross section reads

$$\sigma_{f\leftarrow 1} = 4\pi k_f k_1^{-3}\left|\frac{\sum_j B_{fj}C_{1j}}{C_{11}D}\right|^2 . \tag{2.43}$$

To understand the behavior of $\sigma_{f\leftarrow 1}$ at small values of k_1, we examine the k_1-dependence of $B_{mn}(k_1)$ and $C_{mn}(k_1)$. The latter is in turn expressed using $A_{mn}(k_1)$

and $B_{mn}(k_1)$ obtained from Eq. (2.25) and (2.26). If neither subscript corresponds to the initial channel, we find

$$\left.\begin{array}{l} m \neq 1 \\ n \neq 1 \end{array}\right\} \Rightarrow \begin{array}{l} A_{mn} = A_{mn}^{(0)} + A_{mn}^{(2)} k_1^2 + \ldots, \\ B_{mn} = B_{mn}^{(0)} + B_{mn}^{(2)} k_1^2 + \ldots, \end{array} \tag{2.44}$$

where $A_{mn}^{(s)}$ and $B_{mn}^{(s)}$ are the coefficients of the power series. For $m = n = 1$, we have

$$\begin{aligned} A_{11} &= A_{11}^{(0)} + A_{11}^{(2)} k_1^2 + \ldots, \\ B_{11} &= k_1^{2\ell_1+1}\big(B_{11}^{(0)} + B_{11}^{(2)} k_1^2 + \ldots\big), \end{aligned} \tag{2.45}$$

while for $n = 1$ and $m \neq 1$, we find

$$\begin{aligned} A_{m1} &= k_1^{\ell_1+1}\big(A_{m1}^{(0)} + A_{m1}^{(2)} k_1^2 + \ldots\big), \\ B_{m1} &= k_1^{\ell_1+1}\big(B_{m1}^{(0)} + B_{m1}^{(2)} k_1^2 + \ldots\big), \end{aligned} \tag{2.46}$$

and if $m = 1$ and $n \neq 1$, we have

$$\begin{aligned} A_{1n} &= k_1^{-\ell_1-1}\big(A_{1n}^{(0)} + A_{1n}^{(2)} k_1^2 + \ldots\big), \\ B_{1n} &= k_1^{\ell_1}\big(B_{1n}^{(0)} + B_{1n}^{(2)} k_1^2 + \ldots\big). \end{aligned} \tag{2.47}$$

We obtain the following behavior in leading order

$$\left.\begin{array}{ll} B_{11} & \sim k_1^{2\ell_1+1} \\ B_{f1} & \sim k_1^{\ell_1+1} \\ B_{1j} & \sim k_1^{\ell_1} \\ B_{fj} & \sim \text{const} \end{array}\right\} \text{ and } \quad \left\{\begin{array}{l} C_{11} \sim C_{11}^{(0)} = \text{const} \\ C_{1j} \sim C_{1j}^{(0)} k_1^{\ell_1+1}, \end{array}\right. \tag{2.48}$$

where $f \neq 1$ and $j \neq 1$. Note that both $C_{11}^{(0)}$ and $C_{1j}^{(0)}$ are complex valued constants.

2.3.3.1 Jost function analysis for inelastic cross sections

For $f \neq 1$, Eq. (2.48) yields $\sum_j B_{fj} C_{1j} \sim k_1^{\ell_1+1}$, and using the fact that k_f reaches a finite value as $k_1 \to 0$, we obtain

$$\sigma_{f\leftarrow 1}^{\mathrm{inel}(\ell_1)} \sim k_f k_1^{-3} \frac{k_1^{2\ell_1+2}}{|D(k_1)|^2} \approx \frac{k_1^{2\ell_1-1}}{|D(k_1)|^2}. \tag{2.49}$$

Thus, the threshold behavior of the cross sections will be dictated by $D(k_1)$. We denote $k \equiv k_1$ and $\ell \equiv \ell_1$ to simplify notation, and we now focus our attention on $D(k)$. From Eqs. (2.42) and (2.29) we have

$$D(k) = A_{11} - iB_{11} + \mathsf{j}_{11},$$

with $\mathsf{j}_{11} = C_{11}^{-1} \sum_{n\neq 1} (A_{1n} - iB_{1n}) C_{1n}$, see Eq. (2.41). Using the leading terms in Eq. (2.47) together with $C_{11} \approx C_{11}^{(0)} = \text{constant}$, and $C_{1n\neq 1} \approx C_{1n\neq 1}^{(0)} k^{\ell+1}$ given in Eq. (2.48), we write

$$\begin{aligned}
\mathsf{j}_{11} &= \frac{1}{C_{11}^{(0)}} \sum_{n\neq 1} \Big[k^{-\ell-1} \left(A_{1n}^{(0)} + k^2 A_{1n}^{(2)} + \dots \right) \\
&\qquad -ik^{\ell} \left(B_{1n}^{(0)} + k^2 B_{1n}^{(2)} + \dots \right) \Big] C_{1n}^{(0)} k^{\ell+1}, \\
&= \sum_{n\neq 1} \frac{C_{1n}^{(0)}}{C_{11}^{(0)}} \Big[\left(A_{1n}^{(0)} + k^2 A_{1n}^{(2)} + \dots \right) \\
&\qquad -ik^{2\ell+1} \left(B_{1n}^{(0)} + k^2 B_{1n}^{(2)} + \dots \right) \Big], \\
&\equiv \mathsf{j}_0 + \mathsf{j}_2 k^2 - ik^{2\ell+1} \left(\mathsf{g}_0 + \mathsf{g}_2 k^2 \right) + \dots .
\end{aligned} \tag{2.50}$$

The complex numbers $\mathsf{j}_s \equiv \sum_{n\neq 1} A_{1n}^{(s)} C_{1n}^{(0)} / C_{11}^{(0)}$ and $\mathsf{g}_s \equiv \sum_{n\neq 1} B_{1n}^{(s)} C_{1n}^{(0)} / C_{11}^{(0)}$ have small magnitudes. Using Eq. (2.45), we obtain

$$\begin{aligned}
D(k) = &\left[(A_0 + \mathsf{j}_0) + (A_2 + \mathsf{j}_2) k^2 + \dots \right] \\
&-ik^{2\ell+1} \left[(B_0 + \mathsf{g}_0) + (B_2 + \mathsf{g}_2) k^2 + \dots \right],
\end{aligned} \tag{2.51}$$

where we employed the simpler notation $A_s \equiv A_{11}^{(s)}$ and $B_s \equiv B_{11}^{(s)}$. The exact form of $D(k)$ depends on the value of ℓ, and for this reason we consider $\ell = 0$ and $\ell \geq 1$ separately.

• $\boldsymbol{\ell} = 0$ — For s-wave we have

$$\begin{aligned} D(k) &= \left[(A_0 + \mathsf{j}_0) + (A_2 + \mathsf{j}_2)k^2 + \dots\right] \\ &\quad -ik\left[(B_0 + \mathsf{g}_0) + (B_2 + \mathsf{g}_2)k^2 + \dots\right], \\ &= D_0 + D_1 k + D_2 k^2 + D_3 k^3 + \dots, \end{aligned}$$

where $D_0 = A_0 + \mathsf{j}_0$, $D_1 = -i(B_0 + \mathsf{g}_0)$, $D_2 = (A_2 + \mathsf{j}_2)$, $D_3 = -i(B_2 + \mathsf{g}_2)$, and so on. The expansion of $|D|^2$ takes the form

$$|D(k)|^2 \simeq \Delta_0 + \Delta_1 k + \Delta_2 k^2 + \dots \,, \tag{2.52}$$

with $\Delta_0 = |D_0|^2$, $\Delta_1 = D_0^* D_1 + D_0 D_1^*$, $\Delta_2 = |D_1|^2 + D_0^* D_2 + D_0 D_1^*$, etc. The denominator $|D|^2$ will exhibit the Wigner or NTR scaling depending on the magnitude of A_0. If $|A_0|$ is large, then $|D_0|$ is also large and Δ_0 is the dominant term in Eq. (2.52) at low k. However, if A_0 is vanishingly small, and since j_0 is also small, there will be a range of k where Δ_0 is not the dominant contribution, and since Δ_1 is also proportional to D_0, the dominant term will be $\Delta_2 \approx |D_1|^2$ (since both $D_0 D_2^*$ and $D_0^* D_2$ are also small). This condition gives the NTR scaling for a given range of k. To better distinguish the Wigner and NTR regimes, Δ_1 can be omitted in Eq. (2.52) since it only plays a minor role in the transition between the two regimes. Hence, Eq. (2.49) reads

$$\sigma_{\ell=0}^{\text{inel}} \equiv \sigma_{f\leftarrow 1}^{\text{inel}(\ell=0)} \sim \frac{k^{-1}}{\Delta_0 + k^2 \Delta_2}. \tag{2.53}$$

From Eqs. (2.43) and (2.49) it follows that this k-scaling is the same for any exit channel $f \neq 1$, although the overall magnitude is channel specific. The appearance

of the NTR scaling depends of the relative strength of Δ_0 and Δ_2. From Eq. (2.53), we have

$$\sigma_{\ell=0}^{\rm inel} \sim \begin{cases} k^{-1}, & \text{Wigner:} \quad k \ll \sqrt{|\Delta_0/\Delta_2|} \\ k^{-3}, & \text{NTR:} \quad k \gg \sqrt{|\Delta_0/\Delta_2|} \end{cases} . \tag{2.54}$$

- $\boldsymbol{\ell \geq 1}$ — We first consider the p-wave ($\ell = 1$) case. From Eq. (2.51) we have

$$\begin{aligned} D(k) &= \left[(A_0 + \mathsf{j}_0) + (A_2 + \mathsf{j}_2)k^2 + \dots\right] \\ &\quad -ik^3 \left[(B_0 + \mathsf{g}_0) + (B_2 + \mathsf{g}_2)k^2 + \dots\right], \\ &= D_0 + D_2 k^2 + D_3 k^3 + D_4 k^4 + \dots, \end{aligned}$$

where $D_0 = A_0 + \mathsf{j}_0$ and $D_2 = (A_2 + \mathsf{j}_2)$ as before, $D_4 = A_4 + \mathsf{j}_4$, and $D_3 = -i(B_0 + \mathsf{g}_0)$ which is similar to D_1 in the $\ell = 0$ case. The expansion of $|D|^2$ reads

$$|D(k)|^2 \simeq \Delta_0 + \Delta_2 k^2 + \Delta_3 k^3 + \Delta_4 k^4 + \dots , \tag{2.55}$$

with $\Delta_0 = |D_0|^2$, $\Delta_2 = D_0^* D_2 + D_0 D_2^*$, $\Delta_3 = D_0^* D_3 + D_0 D_3^*$, and $\Delta_4 = |D_2|^2 + D_0^* D_4 + D_0 D_4^*$. Again, when A_0 (and hence D_0) is large, Δ_0 is the dominant term in Eq. (2.55) for small k, corresponding to the Wigner regime. But when A_0 and j_0 are small, then D_0 is small, and there will be a range of k for which Δ_0, Δ_2 and Δ_3 are small compared to $\Delta_4 \approx |D_2|^2$. Similar to $\ell = 0$ case, Δ_2 and Δ_3 play a minor role in the transition between the Wigner (with Δ_0 dominant) and NTR (with Δ_4 dominant) regimes, and can be omitted for clarity, which yields

$$|D(k)|^2 \approx \Delta_0 + \Delta_4 k^4 + \dots . \tag{2.56}$$

For $\ell = 2$, Eq. (2.51) yields in a similar way

$$\begin{aligned} D(k) &= \left[(A_0 + \mathsf{j}_0) + (A_2 + \mathsf{j}_2)k^2 + \dots\right] \\ &\quad -ik^5\left[(B_0 + \mathsf{g}_0) + (B_2 + \mathsf{g}_2)k^2 + \dots\right], \\ &= D_0 + D_2k^2 + D_4k^4 + D_5k^5 \dots, \end{aligned}$$

with D_0, D_2, D_4 as given above, and $D_5 = -i(B_0 + \mathsf{g}_0)$ similar to D_1 in the $\ell = 0$ case. The expansion of $|D|^2$ becomes

$$|D(k)|^2 \simeq \Delta_0 + \Delta_2 k^2 + \Delta_4 k^4 + \dots, \tag{2.57}$$

with Δ_0, Δ_2, Δ_4 the same as for $\ell = 1$. There is no k^3 term, which holds for $\ell \geq 2$ in general. Again, Δ_2 plays only a minor role, and the same expression (2.56) for $|D|^2$ can therefore be used for all $\ell \geq 1$. Finally, combining Eqs. (2.49) and (2.56), we obtain

$$\sigma_{\ell\neq 0}^{\text{inel}} \equiv \sigma_{f\leftarrow 1}^{\text{inel}(\ell\neq 0)} \sim \frac{k^{2\ell-1}}{\Delta_0 + k^4\Delta_4}. \tag{2.58}$$

As mentioned above for $\ell = 0$, the k-dependence in Eq. (2.58) is the same for all exit channels $f \neq 1$, with the cross section for each channel having its specific overall magnitude. The appearance of the NTR scaling depends of the relative magnitude of Δ_0 and Δ_4,

$$\sigma_{\ell\neq 0}^{\text{inel}} \sim \begin{cases} k^{2\ell-1}, & \text{Wigner:} \quad k \ll |\Delta_0\Delta_4^{-1}|^{1/4}, \\ k^{2\ell-5}, & \text{NTR:} \quad k \gg |\Delta_0\Delta_4^{-1}|^{1/4}. \end{cases} \tag{2.59}$$

In summary, the NTR regime appears when $D_0 \approx A_0$ is vanishingly small. The transition between the Wigner and NTR regimes takes place near $k \approx |D_0D_1^{-1}| \approx |A_0B_0^{-1}|$ for $\ell = 0$, or near $k \approx |D_0D_2^{-1}|^{1/2} \approx |A_0A_2^{-1}|^{1/2}$ for $\ell > 0$.

2.3.3.2 Jost function analysis for elastic cross sections

Under the assumption that the interactions are short-range, one can also apply Eq. (2.48) for the elastic cross section, such that Eq. (2.43) yields

$$\sigma_{1\leftarrow 1}^{\text{elast}} \sim \frac{k}{k^3}\frac{k^{4\ell+2}}{|D(k)|^2} \approx \frac{k^{4\ell}}{|D(k)|^2}. \tag{2.60}$$

The denominator $|D(k)|^2$ is the same as in Eq. (2.49), and only the numerator differs. Thus, for $\ell = 0$ we have

$$\sigma_{\ell=0}^{\text{elast}} \sim \frac{1}{\Delta_0 + k^2\Delta_2}, \tag{2.61}$$

leading to

$$\sigma_{\ell=0}^{\text{elast}} \sim \begin{cases} \text{const}, & \text{Wigner:} \quad k \ll \sqrt{|\Delta_0/\Delta_2|}, \\ k^{-2}, & \text{NTR:} \quad k \gg \sqrt{|\Delta_0/\Delta_2|}. \end{cases} \tag{2.62}$$

For $\ell \geq 1$, we obtain

$$\sigma_{\ell\neq 0}^{\text{elast}} \sim \frac{k^{4\ell}}{\Delta_0 + k^4\Delta_4}, \tag{2.63}$$

which yields

$$\sigma_{\ell\neq 0}^{\text{elast}} \sim \begin{cases} k^{4\ell}, & \text{Wigner:} \quad k \ll |\Delta_0/\Delta_4|^{1/4}, \\ k^{4\ell-4}, & \text{NTR:} \quad k \gg |\Delta_0/\Delta_4|^{1/4}. \end{cases} \tag{2.64}$$

We note that the NTR regime for ℓ scales as the Wigner regime for $\ell-1$; in particular, for $\ell = 1$, the NTR regime behavior is $\sigma^{\text{elast}} \sim k^0 = \text{constant}$.

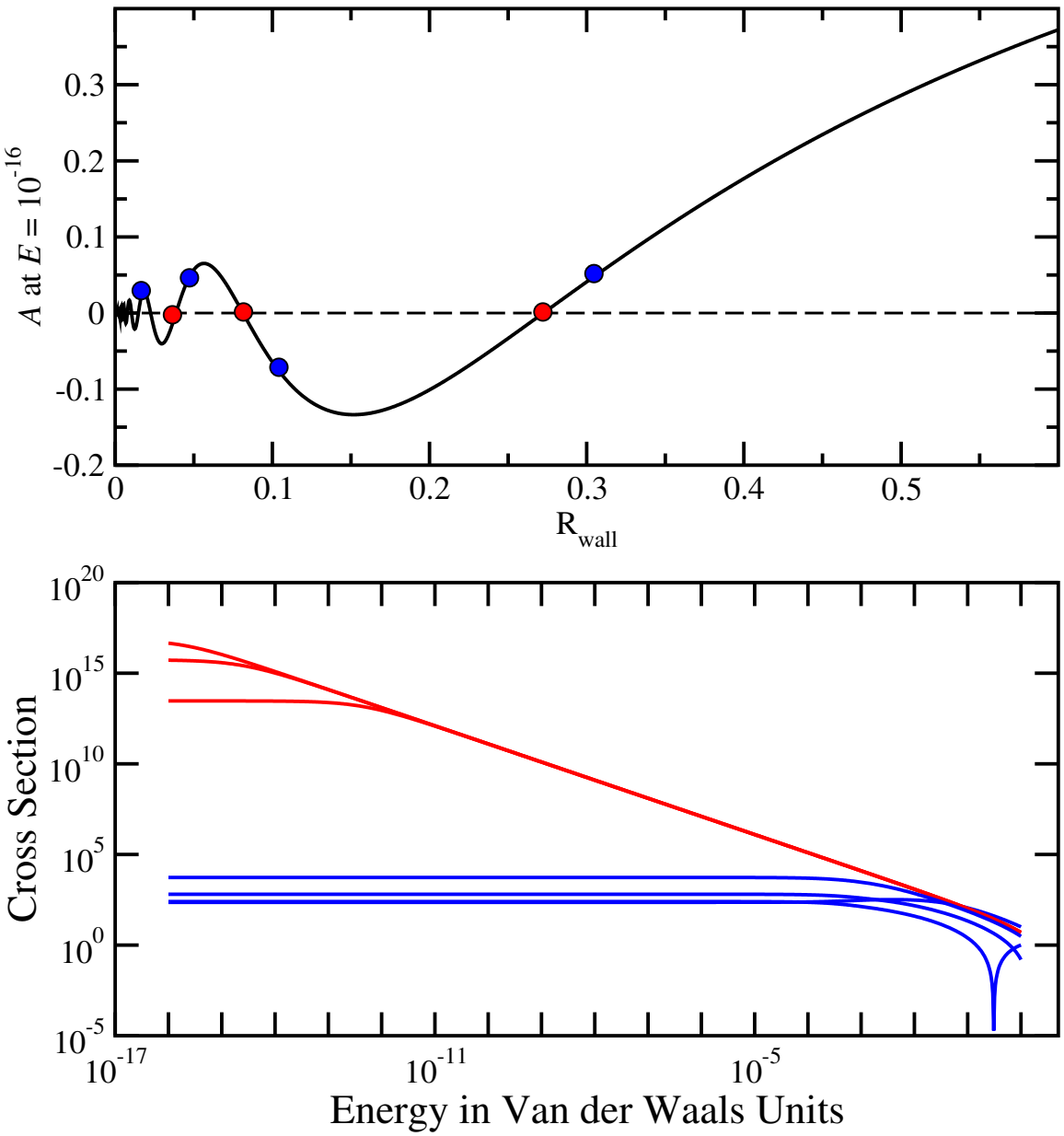

Figure 2.4. Top panel, value of A at $E = 10^{-16}$, which is approximately A_0; 7 specific values of the position of the hard wall are picked and highlighted as red and blue dots. Lower panel, cross sections corresponding to the blue and red dots in the upper panel.

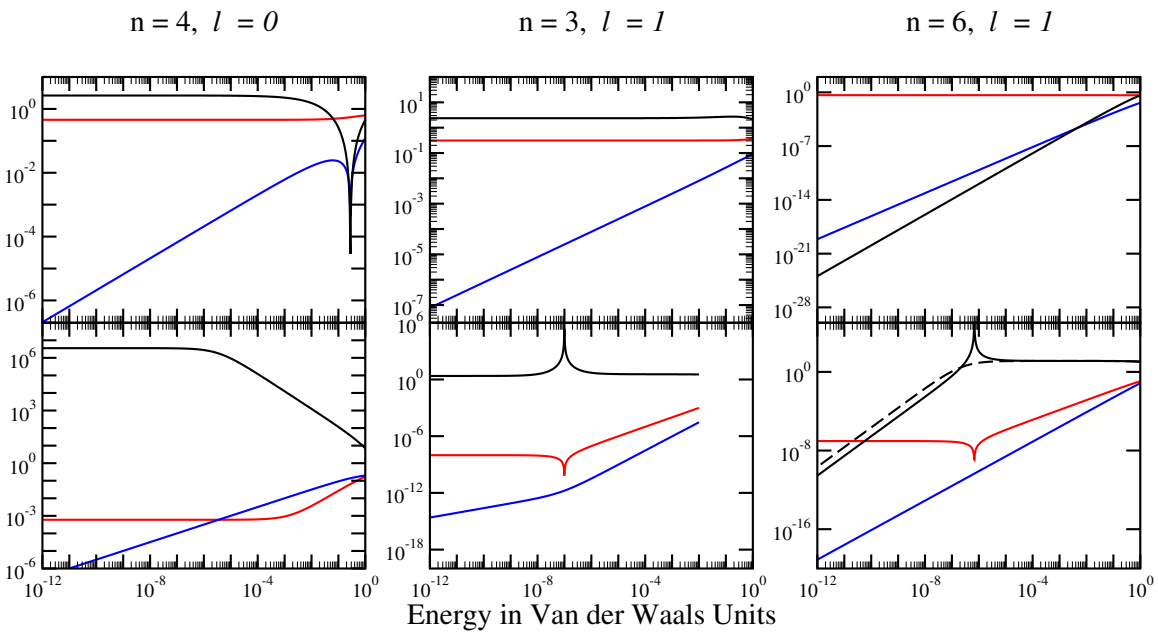

Figure 2.5. Numerical results for the cases $n \neq 2\ell + 3$; top panel, non-resonance case; bottom panel, resonant case. Red curves: $|A(k)|$, blue curves: $B(k)$, black curves: cross section.

Chapter 3
Near Threshold Effects in Efimov Systems

Three-body problems have been studied in a variety of context, such as three-body Coulomb systems [32, 33, 34], and nuclear three-body systems [35, 36, 37]. Efimov predicted that a system with three particles may have a large number of trimer states even when the dimer potential does not posses any bound states [38, 39, 40]. The existence of the Efimov trimer states requires the two-body scattering length a to be much larger than the characteristic range of the two-body interaction R_0. Ultracold gases are ideal candidates for studying Efimov physics since the scattering length a can be tuned using Feshbach resonances. When $a \to -\infty$, an Efimov state near the three-body threshold will give a resonant enhancement for the recombination rate K_3. This enhancement has been experimentally observed as atom loss for a variety of systems [22, 41, 42, 43, 44, 45, 46, 47, 48, 49, 50, 51, 52, 53, 54]. When $a \to +\infty$, a similar enhancement has been observed for the vibrational relaxation rate $K_{\rm rel}$ for collisions between atoms and loosely bound dimers [49, 55, 56, 51, 48]. Resonant peaks for atom loss rates have also been observed for pure ultracold atom gases with $a > 0$ [57, 58, 42], and an avalanche mechanism has been proposed as an explanation in terms of molecule-atom threshold resonances [42, 57], though other experiments have been conducted pointing to different conclusion [59, 60]. For $a \to +\infty$, interference minima as a signature of Efimov states in three atom loss rates have also been observed [58, 42, 57, 43, 61].

Efimov physics has been studied mostly in the zero energy limit, e.g., the recombination and relaxation rates near zero temperature, and only recently the energy dependence of these quantities has received attention [62, 63, 64, 65, 66, 67]. In this chapter, we investigate the energy dependence of the three body recombination rate K_3 and relaxation rate $K_{\rm rel}$, paying special attention to the threshold behavior of $K_3(E)$ for $a < 0$ and $K_{\rm rel}(E)$ for $a > 0$ when an Efimov state is near the threshold. We also explore the behavior of $K_3(E)$ for $a > 0$ for specific values of a leading to large suppression effects.

3.1 Model Potential and Jost Function Approach

We present our study of the Efimov effect for the case of identical bosons, BBB, where B denotes a neutral bosonic atom in its ground state. Our findings are however also applicable to other systems (such as mixtures of the type BBX) which have a similar attractive Efimov potential. In addition, we only consider the case of total angular momentum $J = 0$, which is sufficient at low energy where contributions of higher J values are strongly suppressed.

Although the long range Efimov states seem counterintuitive, their appearance can be explained by the attractive $1/R^2$ behavior of the lowest adiabatic hyperspherical potential for $R_0 \ll R \ll |a|$, where R is the hyperradius, and a and R_0 are the two-body scattering length and characteristic interaction range, respectively. The attractive Efimov potential takes the form [68]

$$V_{\rm Ef}(R) = -\frac{s_0^2 + 1/4}{R^2}\,, \tag{3.1}$$

where $s_0 = 1.00624$ is a universal constant. Following [68], the appropriate reduced mass is implicitly included in $V_{\rm Ef}(R)$; the same is true throughout this chapter for

all potentials. According to Efimov [38], when $a \to \pm\infty$, the number of three-body Efimov states is proportional to $\ln(|a|/R_0)$, and is independent of the sign of a. However, the lowest adiabatic hyperspherical potential depends on the sign of a. Specifically, when $a < 0$, the Efimov potential correlates in the asymptotic region $R \gg |a|$ to the repulsive potential

$$V_{\rm asy}(R) = \frac{\ell_{\rm eff}(\ell_{\rm eff}+1)}{R^2} \,, \tag{3.2}$$

with $\ell_{\rm eff} = \frac{3}{2}$, which is the lowest three-body continuum channel. Again, $V_{\rm asy}$ contains the reduced mass. In this case, the three-body recombination rate K_3 exhibits a resonant enhancement when an Efimov state is near the three-body breakup threshold. When $a > 0$, the effect of the Efimov states on the three-body loss rates is quite different, which is due to the fact that the Efimov potential correlates to the weakly bound dimer channel. Following Esry et al. [68], we employ a simplified model which captures the essential physics of the Efimov effect.

3.1.1 Single-channel model for $a < 0$

For $a < 0$, the entrance channel is the lowest three-body continuum channel, and all other channels corresponding to the three-body continuum can be ignored since their hyperspherical adiabatic potentials are entirely repulsive; their contribution will be highly suppressed at low energy . We assume that the dimer has deeply bound states, which is typical for atom–atom potentials, and we shall use a single channel model to analyze the three-body recombination. The recombination channels corresponding to the deeply bound dimer states are taken into account *a posteriori*, as explained in this section. The fact that the coupling of the entrance channel to the recombination channels takes place at short range ($R < R_0$) allows for a single-channel model of the multi-channel problem that reproduces qualitatively the energy

dependence of K_3 [62]. To extract $K_3(E)$ from the single-channel results, we use an approach based on the Jost function, as opposed to the wave function as used by [62]. Namely, we obtain the single-channel regular solution $\phi_k(R)$ by numerically solving

$$\phi_k''(R) = [V_1(R) - k^2]\phi_k(R), \tag{3.3}$$

where V_1 is the potential curve shown in Fig. 3.1. Note that for $R_0 \ll R \ll |a|$, $V_1(R) \approx V_{\rm Ef}(R)$ and for $R \gg |a|$, $V_1(R) \approx V_{\rm asy}(R)$. Equation (3.3) is supplemented with the initial condition $\phi_k(R_0) = \sin\varphi_0$ and $\phi_k'(R_0) = \cos\varphi_0$, where the phase φ_0 accounts for the contribution of the short range region. As shown in the inset in Fig. 3.1, the parameter φ_0 can be adjusted to obtain agreement with the experimental results for the value of a_1^- of the two-body scattering length corresponding the appearance of first Efimov state. However, in the remainder of this chapter, we employ the simple choice $\varphi_0 = 0$ which corresponds to a hard wall at $R = R_0 = R_{\rm vdW}$. The two-body van der Waals length $R_{\rm vdW}$ is the characteristic length scale for the short range region, with $R_{\rm vdW} = (2\mu_2 C_6/\hbar^2)^{1/4}$, where μ_2 is the two-body reduced mass and C_6 the dispersion coefficient for the van der Waals interaction $(-C_6/R^6)$ between two neutral ground state atoms. $R_{\rm vdW}$ and the corresponding van der Waals energy $E_{\rm vdW} = \hbar^2/2\mu_2 R_{\rm vdW}^2$ are used as units in Fig. 3.1.

We extract the Jost function,

$$\boldsymbol{\mathcal{J}}(k) = A(k) - iB(k), \tag{3.4}$$

from the asymptotic ($R \to \infty$) behavior $k^{\ell_{\rm eff}+1}\phi_k(R) \sim A(k) j_{\ell_{\rm eff}}(kR) + B(k) n_{\ell_{\rm eff}}(kR)$, where $j_{\ell_{\rm eff}}$ and $n_{\ell_{\rm eff}}$ are the Riccati–Bessel spherical functions. Note that $V(R)$ and k are real, and thus ϕ_k, $A(k)$ and $B(k)$ are also real. The physical solution ψ_k, which

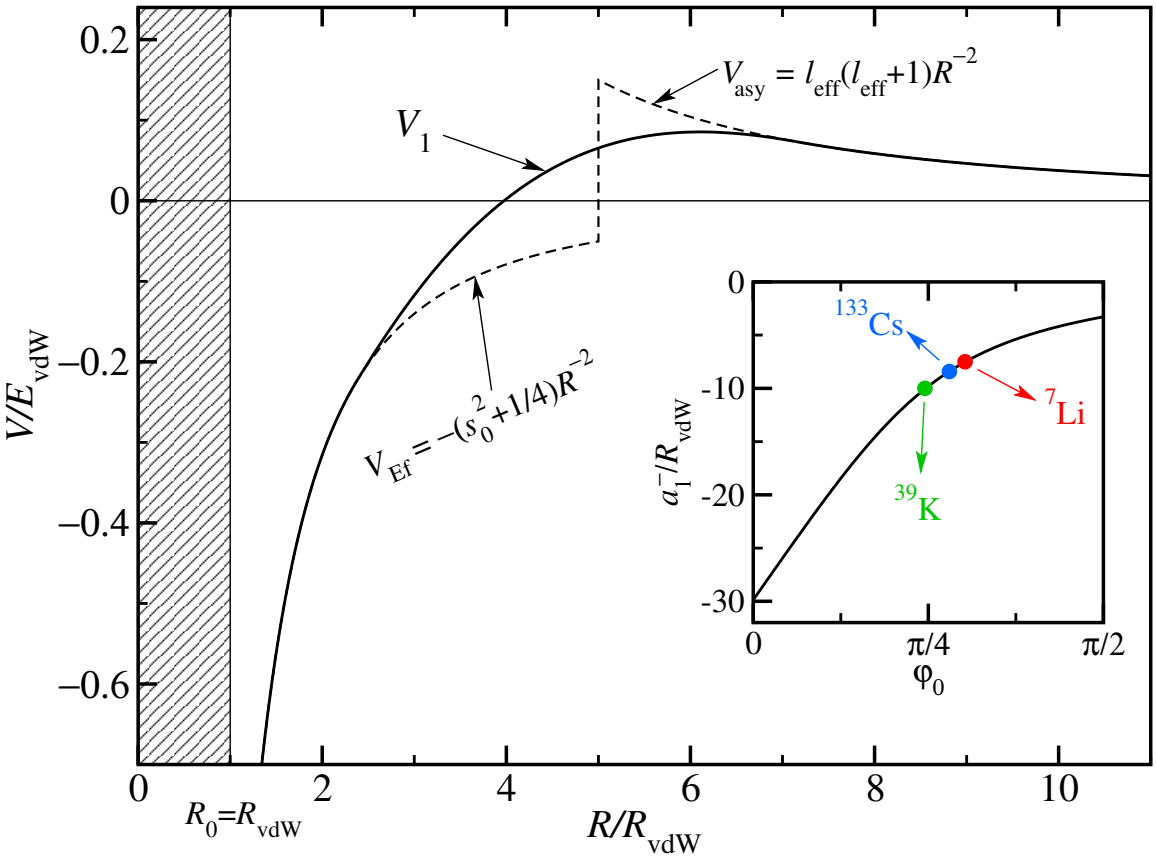

Figure 3.1. Lowest hyperspherical potential for $a = -5R_{\rm vdW}$. Solid line: smooth approximation for the realistic hyperspherical potential $V_1(R)$ in Eq. (3.3). The shaded area represents the short range region $0 < R < R_0$, taken into account via the phase φ_0 appearing as a parameter for the initial condition at $R_0 = R_{\rm vdW}$ for Eq. (3.3). Dotted line: approximate potential (discontinuous at $R = |a|$) used in Sec. 3.2.1. The inset shows the φ_0 dependence of the scattering length a_1^- corresponding to the appearance of the first Efimov state. Also shown are three experimental results for Cs, K and Li [68] illustrating how φ_0 can be adjusted to match experiments.

behaves asymptotically as $\psi_k(R) \sim \frac{i}{2}[h^-_{\ell_{\rm eff}}(kR) - \frac{F^*}{F} h^+_{\ell_{\rm eff}}(kR)]$, where $h^\pm_\ell \equiv n_\ell \pm i j_\ell$, can be expressed as [1]

$$\psi_k = \frac{k^{\ell_{\rm eff}+1}}{\boldsymbol{\mathcal{J}}(k)} \phi_k. \tag{3.5}$$

For very low k, the regular solution is independent of k at short range, $\phi_k(R) \approx \phi_0(R)$. Thus, at short range, we have

$$\psi_k(R)|_{\text{short range}} \approx \frac{k^{\ell_{\rm eff}+1}}{\boldsymbol{\mathcal{J}}(k)} \phi_0(R), \tag{3.6}$$

Returning to the multi-channel problem, and noting that the coupling of the entrance channel to the deeply bound states of the dimer takes place at short range, the entrance channel component $\psi_{1,k}$ of the full wave function can be approximated by the single-channel solution (3.5), i.e.,

$$\psi_{1,k} \approx \psi_k = \frac{k^{\ell_{\rm eff}+1}}{\boldsymbol{\mathcal{J}}(k)} \phi_k. \tag{3.7}$$

Since the couplings are restricted to short range, the single channel result in Eq. (3.6) can be used to obtain the k dependence of the full solution of the coupled-channel problem [31]. Indeed, the k-dependence in Eq. (3.6) will be imprinted via the couplings to all other components of the wave function. We emphasize that, although the entrance-channel component has the k-dependence in Eq. (3.6) only at short range, the other components obey this k-dependence for all R,

$$\psi_{n,k} \sim \frac{k^{\ell_{\rm eff}+1}}{\boldsymbol{\mathcal{J}}(k)} g_n(k_n, R), \tag{3.8}$$

where $g_n(k_n, R)$ is the radial wave function for channel n with momentum k_n. Recalling that only outgoing waves are allowed in the dimer channels n, the corresponding asymptotic ($R \to \infty$) behavior of $\psi_{n,k}$ is

$$\psi_{n,k}(R) \sim \sqrt{\frac{k}{k_n}} S_{n,1}(k) e^{+ik_n R}. \tag{3.9}$$

Together with Eq. (3.8) and substituting $2\ell_{\text{eff}} + 1 = 4$, it leads to the k-dependence of the S-matrix element,

$$|S_{n,1}(k)|^2 \sim \frac{k^4}{|\mathcal{J}(k)|^2}. \tag{3.10}$$

Finally, the total three-body recombination rate [69], $K_3 \sim \frac{1}{k^4} \sum_{n \neq 1} |S_{n,1}|^2$, reads

$$K_3 \sim \frac{1}{|\mathcal{J}(k)|^2} = \frac{1}{A^2(k) + B^2(k)}. \tag{3.11}$$

Thus, the k-dependence of the rate K_3 is dictated by the k-dependence of the Jost function.

3.1.2 Single-channel model for relaxation ($a > 0$)

As shown in Fig. 3.2 for the case $a > 0$, there exists a loosely bound dimer state (channel 2, slightly below the three-body breakup threshold) which correlates to the Efimov potential, while the lowest three-body continuum channel is purely repulsive (channel 1). In channel 2, the three-body system corresponds to an extended weakly bound Feshbach molecule interacting with an atom. Since decay into more deeply bound and compact dimers takes place due to short-range couplings, a single-channel model similar to the case $a < 0$ described in Sec. 3.1.1 above is warranted for the rate of the vibrational relaxation rate K_{rel}, which will thus be expressed in terms of the single channel Jost function.

In this case, we have an atom–dimer scattering problem with relative angular momentum ℓ, so that one simply replaces $\ell_{\rm eff}$ by ℓ in Eqs. (3.7) and (3.8), leading to

$$|S_{fi}(k)|^2 \sim \frac{k^{2\ell+1}}{|\boldsymbol{\mathcal{J}}(k)|^2}. \tag{3.12}$$

We are interested in $\ell = 0$ (ultracold regime), so that, $\sigma = \frac{\pi}{k^2}\sum_{f\neq i}|S_{fi}(k)|^2$, the cross section for this inelastic process gives the relaxation rate $K_{\rm rel} = v_{\rm rel}\sigma$ (with the relative velocity $v_{\rm rel} \propto k$) in terms of the S-matrix as [69]

$$K_{\rm rel}(k) \sim \frac{1}{k}\sum_{f\neq i}|S_{fi}|^2, \tag{3.13}$$

Here, i and f correspond to the entrance (shallow) dimer state, and final (deeply bound) dimer states respectively. The S-matrix is given in term of the Jost function by Eq. (3.12) with $\ell = 0$, i.e.,

$$|S_{fi}(k)|^2 \sim \frac{k}{|\boldsymbol{\mathcal{J}}(k)|^2}. \tag{3.14}$$

Combining the two equations above, we find the k-dependence of the relaxation rate,

$$K_{\rm rel}(k) \sim \frac{1}{|\boldsymbol{\mathcal{J}}(k)|^2} = \frac{1}{A^2(k)+B^2(k)}. \tag{3.15}$$

3.1.3 Two-channel model for $a > 0$

As discussed above for $a > 0$, and as illustrated in Fig. 3.2, there exists a loosely bound dimer state (channel 2) correlated to the Efimov potential, while the lowest three-body continuum channel being purely repulsive (channel 1). Therefore, to in-

vestigate the three-body recombination for the formation of Feshbach molecules, we adopt a model that only includes these two channels:

$$\begin{aligned} \phi_1'' &= [V_{11} - k_1^2]\phi_1 + [V_c\partial_R + \partial_R V_c]\phi_2, \\ \phi_2'' &= [V_{22} - k_2^2]\phi_2 - [V_c\partial_R + \partial_R V_c]\phi_1. \end{aligned} \tag{3.16}$$

According to [68], the coupling between channel 1 and channel 2 is significant only near $R = a$. Thus we employ a simple form for the coupling,

$$V_c(R) = \begin{cases} \frac{0.01}{a}\sin^4\left(\pi\frac{R-R_a}{R_b-R_a}\right), & R_a < R < R_b, \\ 0, & \text{otherwise}, \end{cases} \tag{3.17}$$

with $R_a = 0.5a, R_b = 1.5a$. Note that the scaling $V_c(R) \sim a^{-1}$ follows the realistic coupling, and the value 0.01 for the coefficient controlling the strength of the coupling in Eq. (3.17), chosen arbitrarily, can be adjusted to match experimental data for a particular system [68]. In the region $R_0 \ll R \ll a$ we have

$$V_{11}(R) \approx \frac{s_1^2 - 1/4}{R^2}, \qquad V_{22}(R) \approx V_{\rm Ef} = -\frac{s_0^2 + 1/4}{R^2}\ , \tag{3.18}$$

where $s_1 = 4.4653$ and $V_{\rm Ef}$ is the Efimov potential in Eq. (3.1). In the asymptotic region $R \gg |a|$,

$$V_{11}(R) \approx \frac{\ell_{\rm eff}(\ell_{\rm eff}+1)}{R^2}, \qquad V_{22}(R) \approx E_b, \tag{3.19}$$

where $E_b \propto -1/a^2$ is the binding energy of the shallow dimer. In the region near $R = a$, $V_{11}(R)$ and $V_{22}(R)$ are connected smoothly between the inner and outer regions using high order polynomials; namely, we ensure their continuity and the continuity of their first and second derivatives.

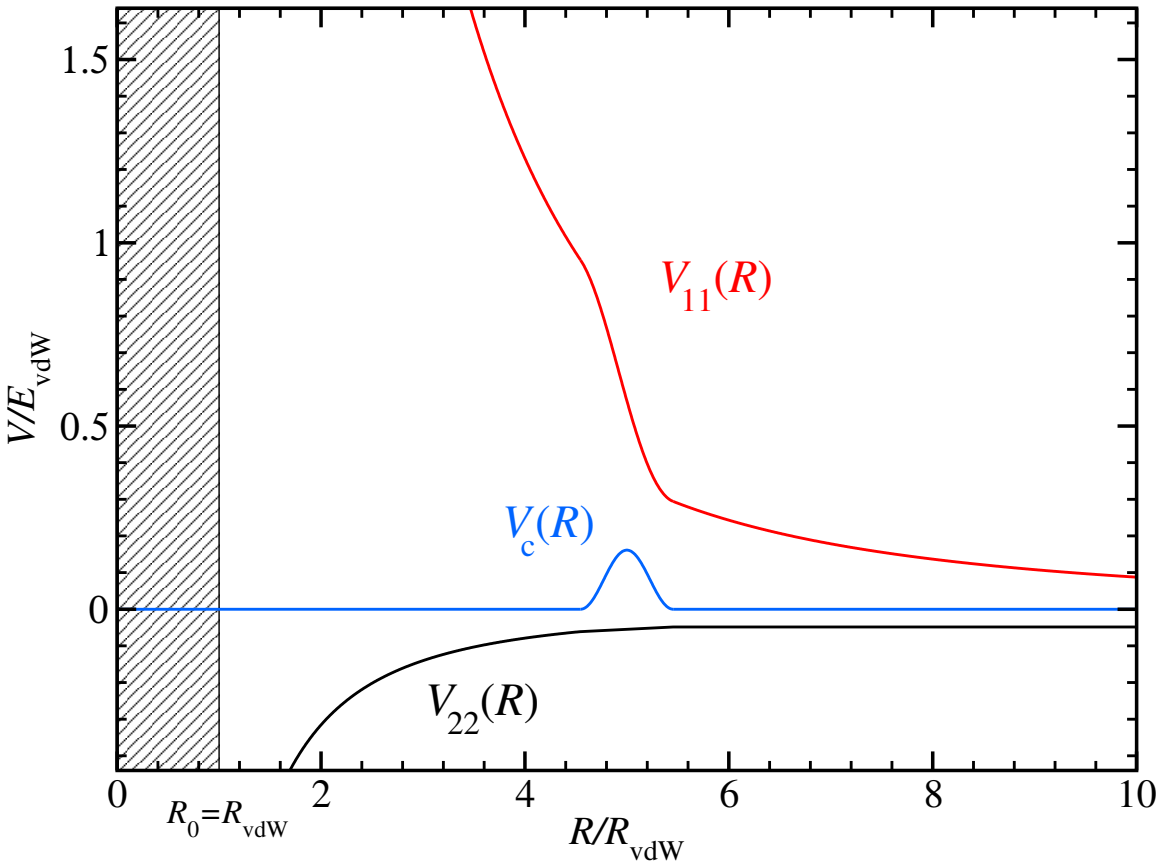

Figure 3.2. Schematic representation of the potentials used in the two channel model, see Eqs. (3.16,3.17). Red curve: hyperspherical potential for channel 1. Black curve: hypershperical potential for channel 2 corresponding to the shallow dimer state. Blue curve: coupling potential V_c which is non-zero only near $R = a$. The shaded area represents the short range region.

3.2 Numerical Results for NTRs in Efimov Systems

3.2.1 Single channel results for $a < 0$

Using the model described in Sec. 3.1.1, we carefully tune the two-body scattering length a such that there is an Efimov state extremely close to the threshold. Here, since there is only one channel corresponding to the three free atoms, the threshold refers to it (see Fig. 3.1). In Fig. 3.3, we show results for the first five Efimov states. Although arbitrary units are used for the three-body recombination rate K_3 in Fig. 3.3, one could introduce a multiplicative parameter on the right hand side of Eqs. (3.10) and (3.11) to adjust the overall magnitude of K_3 to match experimental values. In Fig. 3.3(a), the black curve corresponds to $a_1^-/R_{\rm vdW} = -29.865651$ and displays the first Efimov state as a shape resonance located at very low energy, while the red and blue curves correspond to $a = 2a_1^-$ and $a = a_1^-/2$ respectively. We found that the resonant behavior manifests itself only for values of a within one percent of a_1^-. For values of a outside of this narrow window, the behavior is similar to that shown by the red and blue curves, which we call non-resonant. Although the sharp peak at very low energy is striking, this near threshold resonance (NTR) produces a resonant enhancement for a much wider energy range. More specifically, Fig. 3.3(a) shows that in the resonant case most of the low energy regime is characterized by a new type of behavior; namely, $k^4 K_3$ is constant for energies between the peak and vertical dashed line at $E = E_1$, which we refer to as the NTR regime.

For the subsequent Efimov states corresponding to a_n^- with $n = 2, 3, 4, 5$, an oscillatory regime develops [62] in the energy range $E_n < E < E_0$ between the two vertical dashed lines, as shown in Fig. 3.3(b)–(e). $E_0 = E_{\rm vdW}$ denotes the energy scale associated with short-range physics, while $E_n \equiv E_{a_n^-}$ with $E_a = (R_{\rm vdW}/a)^2 E_{\rm vdW}$ the energy scale given by the centrifugal barrier near $R = |a|$ in Fig. 3.1. With increasing $|a|$, a new Efimov state will appear for each critical value a_n^-, and we confirm the well

known result $a_{n+1}^{-}/a_{n}^{-} = e^{\pi/s_0}$. Our results also confirm that as $|a|$ increases, more oscillations appear at lower energies (reflecting the number of bound states), while the oscillations at higher energy remain unchanged [62], as shown in Fig. 3.3, and summarized in Fig. 3.4.

Although the results in Figs. 3.3 and 3.4 were obtained using the smooth potential shown in Fig. 3.1, the oscillatory behavior can be explained by writing the wavefunction corresponding to the step potential in Fig. 3.1 in terms of Bessel functions. For $R_0 < R < |a|$ the regular solution defined in Sec.3.1.1 can be written as linear combination of Bessel functions of imaginary order,

$$\begin{aligned} \tilde{j}(kR) &\equiv \sqrt{\tfrac{\pi kR}{2}}\mathrm{sech}\left(\tfrac{\pi s_0}{2}\right)\mathrm{Re}[J_{is_0}(kR)], \\ \tilde{n}(kR) &\equiv \sqrt{\tfrac{\pi kR}{2}}\mathrm{sech}\left(\tfrac{\pi s_0}{2}\right)\mathrm{Re}[Y_{is_0}(kR)]. \end{aligned} \tag{3.20}$$

Using the small argument behavior [70] near $R \approx R_0$,

$$\begin{aligned} \tilde{j}(kR) &\sim \left(\tfrac{t_0 kR}{s_0}\right)^{\frac{1}{2}}\cos[s_0\ln(\tfrac{kR}{2}) - \gamma_{s_0}] \\ \tilde{n}(kR) &\sim \left(\tfrac{kR}{t_0 s_0}\right)^{\frac{1}{2}}\sin[s_0\ln(\tfrac{kR}{2}) - \gamma_{s_0}], \end{aligned} \tag{3.21}$$

where $\gamma_{s_0} = \arg[\Gamma(1+is_0)]$ and $t_0 = \tanh(\frac{\pi s_0}{2})$. Thus the suitable linear combination for the regular solution is

$$\begin{aligned} \phi_k(R) = \quad & \left(\tfrac{R_0 t_0}{s_0 k}\right)^{\frac{1}{2}}\Bigg(\cos[s_0\ln(\tfrac{kR_0}{2}) - \gamma_{s_0}]\tilde{j}(kR) \\ & - t_0^{-1}\sin[s_0\ln(\tfrac{kR_0}{2}) - \gamma_{s_0}]\tilde{n}(kR)\Bigg). \end{aligned} \tag{3.22}$$

For $R > |a|$, as mentioned in Sec. 3.1.1, the regular solution can be written as a linear combination of the Riccati–Bessel functions

$$k^{\ell_{\text{eff}}+1}\phi_k(R) = A(k)j_{\ell_{\text{eff}}}(kR) + B(k)n_{\ell_{\text{eff}}}(kR). \tag{3.23}$$

By matching at $R = |a|$, i.e., equating the expressions in Eq. (3.22) and Eq. (3.23) and their derivatives, and using the behavior at large argument [70] near $R = |a|$,

$$\begin{aligned} \tilde{j}(kR) &\sim \cos(kR - \tfrac{\pi}{4}), \\ \tilde{n}(kR) &\sim \sin(kR - \tfrac{\pi}{4}), \end{aligned} \tag{3.24}$$

we obtain

$$\begin{aligned} A(k) &= k^2 \left(\tfrac{R_0}{s_0 t_0}\right)^{\frac{1}{2}} \sin[s_0 \ln(\tfrac{kR_0}{2}) - \gamma_{s_0}], \\ B(k) &= k^2 \left(\tfrac{R_0 t_0}{s_0}\right)^{\frac{1}{2}} \cos[s_0 \ln(\tfrac{kR_0}{2}) - \gamma_{s_0}], \end{aligned} \tag{3.25}$$

where $\gamma_{s_0} = \arg[\Gamma(1 + is_0)]$ and $t_0 = \tanh(\frac{\pi s_0}{2})$. Therefore, inside the oscillatory regime, the three-body recombination rate reads,

$$K_3(k) \sim \frac{1}{k^4} \frac{s_0 t_0}{R_0} \frac{1}{t_0 + (1 - t_0) \sin^2[s_0 \ln(\frac{kR_0}{2}) - \gamma_{s_0}]}. \tag{3.26}$$

Note that the amplitude of the oscillatory term, $1 - t_0 \approx 0.081$, is much smaller than the background term $t_0 \approx 0.92$, which makes it difficult to discern the difference between the NTR regime and the oscillatory regime in Fig. 3.3. For $k \ll |a|^{-1}$, the Jost function can be expanded as a power series, $A(k) \sim A_0 + A_2 k^2 + \mathcal{O}(k^4)$ and $B(k) \sim k^{2\ell_{\text{eff}}+1}(B_0 + B_2 k^2 + \dots) = B_0 k^4 + \mathcal{O}(k^6)$ (since $\ell_{\text{eff}} = 3/2$) [31]. Using Eq. (3.11), we obtained a simple expression of the three-body recombination rate,

$$K_3(k) \sim \frac{1}{(A_0 + A_2 k^2)^2 + B_0^2 k^8}. \tag{3.27}$$

In the Wigner regime, A_0 is dominant, and the zero energy limit of K_3 is a constant. For the resonant case A_0 is very small, which restricts the Wigner regime to the

extreme ultracold. Thus when k increases, the $A_2 k^2$ term quickly becomes dominant and $K_3(k)$ reads,

$$K_3(E) \sim \frac{1}{k^4 A_2^2}, \tag{3.28}$$

which corresponds to the flat NTR regime shown in Fig. 3.4 for $k^4 K_3$. Note that the transition between Wigner and NTR regimes takes place near $k_{\rm NTR} = \sqrt{|A_0/A_2|}$, which can be estimated from the simple parametrizations $A_0(a) \propto a - a_n^-$ and $A_2(a) \approx A_2(a_n^-) =$ const. in the narrow window of values of a near a_n^-. Fig. 3.4(a) and Fig. 3.3 show the Efimov states as shape resonances, which correspond to the case when A_0 and A_2 have opposite sign, such that $A(k) = 0$ at $k_{\rm NTR}$. Note that the very small but finite term $B_0^2 k^8$ in Eq. (3.27) will prevent K_3 from diverging. In Fig. 3.4(b), the Efimov states are bound just below the three-body threshold, which corresponds to the case when A_0 and A_2 have the same sign. Thus $B_0^2 k^8$ can be neglected in Eq. (3.27), and the transition between the Wigner and NTR regimes is smooth. We emphasize that the $K_3 \sim k^{-4}$ behavior in the NTR regime is accidentally identical to the background k-dependence in the oscillatory regime in Eq. (3.26), though the exact values are offset as depicted in Fig. 3.4.

3.2.2 Single channel results for $a > 0$

When $a > 0$, the Efimov potential correlates with the weakly bound dimer channel, defining the scattering threshold $k = 0$. We expect that a near threshold Efimov state will strongly affect the Feshbach-molecule–atom collisions, resulting in vibrational relaxation into deeply bound dimer states. Here we analyze the vibrational relaxation rate using the single-channel model described in Section 3.1.2 , with the vibrational relaxation rate given by Eq. (3.15),

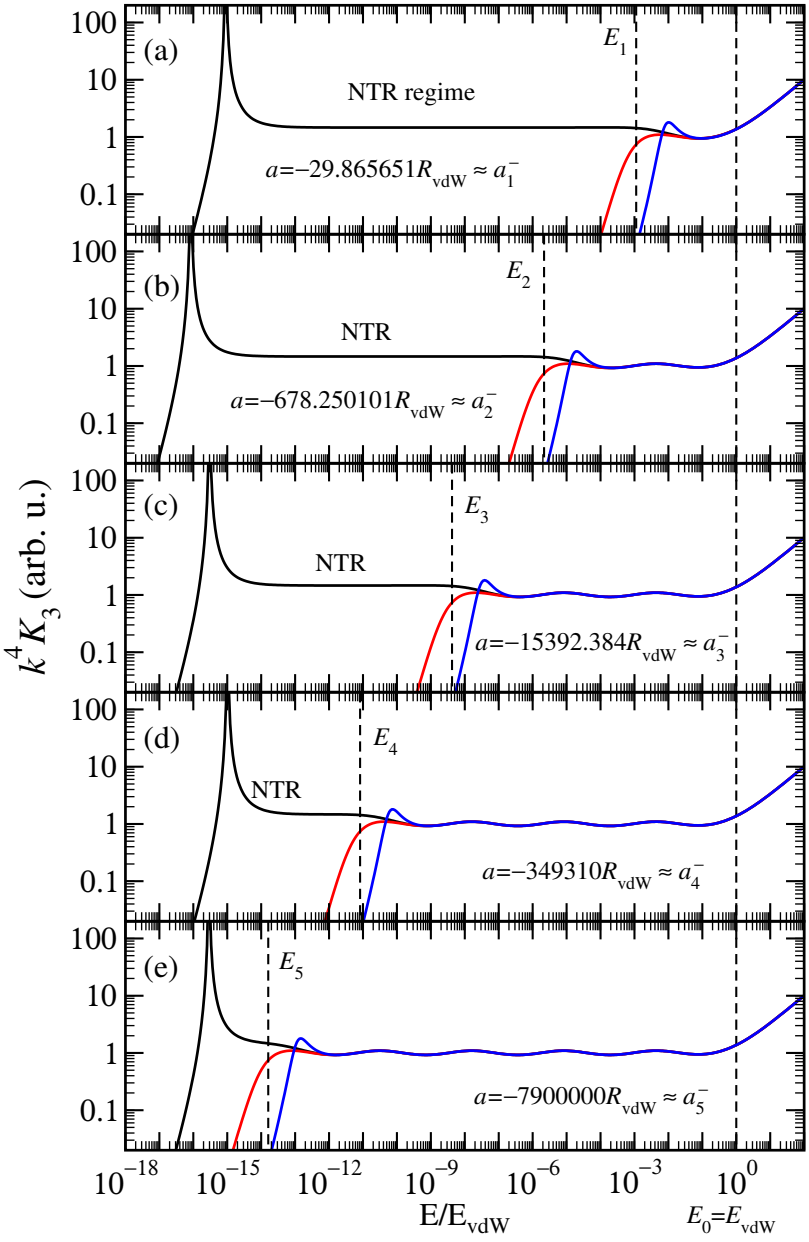

Figure 3.3. Three-body recombination rates for $a < 0$. Black curves: resonant cases for the first five Efimov states (the values of $a \approx a_n^-$ are indicated). Red and blue curves: non-resonant cases corresponding to $a = 2a_n^-$ and $a = a_n^-/2$ respectively. The dashed vertical line at $E_0 = E_{\rm vdW}$ marks the energy scale associated with short range physics. The dashed vertical lines at $E_n \equiv E_{a_n^-} \propto 1/(a_n^-)^2$ mark the boundary between the NTR and oscillatory regimes.

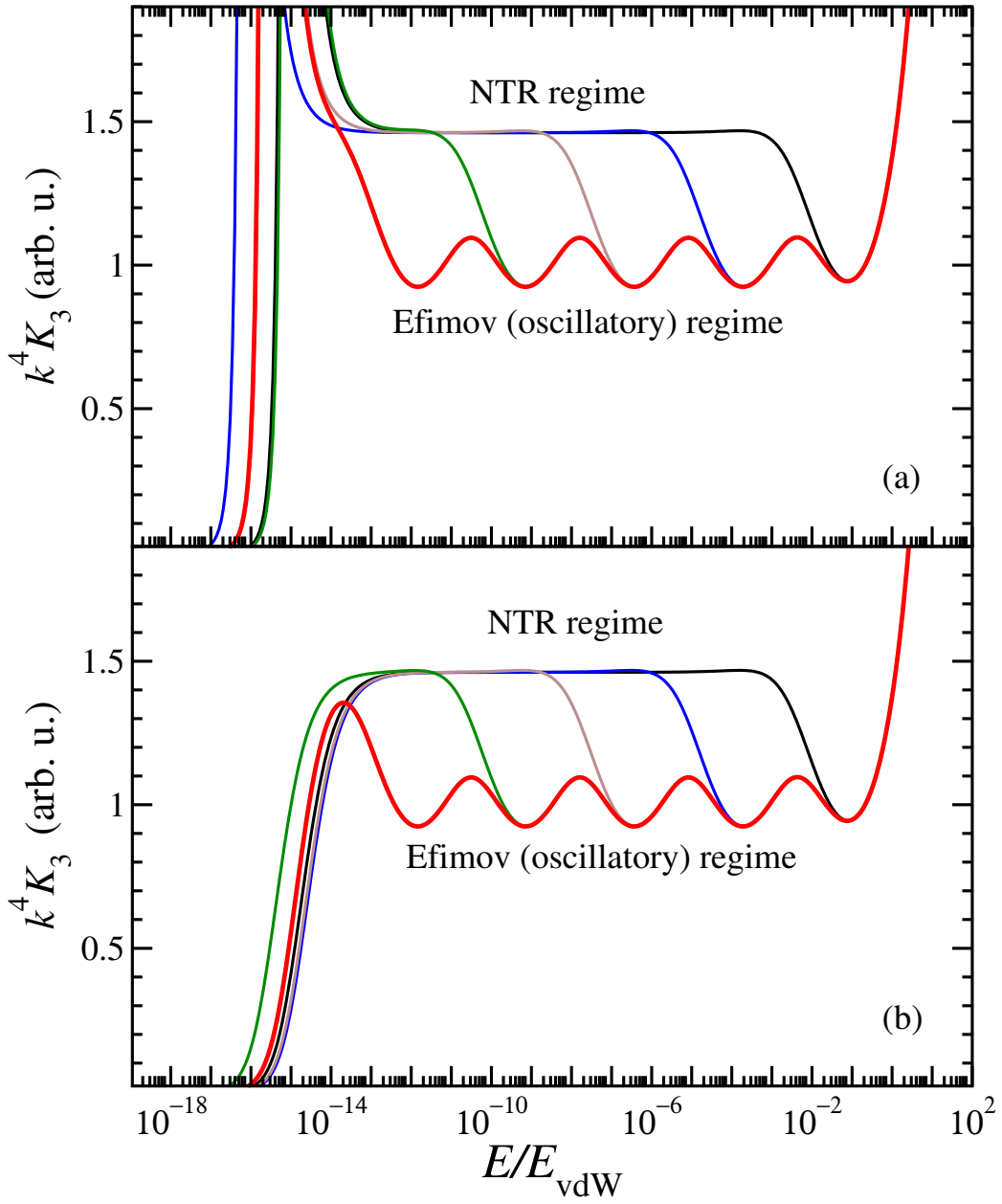

Figure 3.4. Three-body recombination rates for $a < 0$. Black curves: resonant cases for the first five Efimov states (the values of $a \approx a_n^-$ are indicated). Red and blue curves: non-resonant cases corresponding to $a = 2a_n^-$ and $a = a_n^-/2$ respectively. The dashed vertical line at $E_0 = E_{\mathrm{vdW}}$ marks the energy scale associated with short range physics. The dashed vertical lines at $E_n \equiv E_{a_n^-} \propto 1/(a_n^-)^2$ mark the boundary between the NTR and oscillatory regimes.

$$K_{\rm rel}(k) \sim \frac{1}{|\boldsymbol{\mathcal{J}}(k)|^2}. \tag{3.29}$$

Note that $\boldsymbol{\mathcal{J}}(k)$ is the single channel Jost function corresponding to the lower potential curve in Fig. 3.2.

For energies higher than the binding energy of the shallow dimer state, $E_b \sim -1/a^2$, but lower than the short range energy scale $E_0 \sim 1/R_0^2$, i.e., $a^{-1} \ll k \ll R_0^{-1}$, using Eq. (3.22) again, but this time matching it with the asymptotic form of $\phi_k(R)$ for $\ell = 0$, namely

$$k\phi_k(R) = A(k)\sin(kR) + B(k)\cos(kR)\ , \tag{3.30}$$

we obtain

$$\begin{aligned} A(k) = \ & \sqrt{k}\left(\tfrac{R_0 t_0}{2s_0}\right)^{\frac{1}{2}}\Bigg(\cos[s_0\ln(\tfrac{kR_0}{2}) - \gamma_{s_0}] \\ & -\tfrac{1}{t_0}\sin[s_0\ln(\tfrac{kR_0}{2}) - \gamma_{s_0}]\Bigg), \\ B(k) = \ & -\sqrt{k}\left(\tfrac{R_0 t_0}{2s_0}\right)^{\frac{1}{2}}\Bigg(\cos[s_0\ln(\tfrac{kR_0}{2}) - \gamma_{s_0}] \\ & +\tfrac{1}{t_0}\sin[s_0\ln(\tfrac{kR_0}{2}) - \gamma_{s_0}]\Bigg), \end{aligned} \tag{3.31}$$

and thus, $K_{\rm rel}(k)$ reads,

$$K_{\rm rel} \sim \frac{1}{k}\frac{s_0 t_0}{R_0}\frac{1}{t_0^2 + (1-t_0^2)\sin^2[s_0\ln(\frac{kR_0}{2}) - \gamma_{s_0}]}. \tag{3.32}$$

The overall k^{-1} behavior of the relaxation rate in Eq. (3.32) was already mentioned in Ref. [62], where however no oscillatory behavior was found. In our case, we do obtain an oscillatory behavior for $K_{\rm rel}(k)$ similar to that of $K_3(k)$. As shown in Fig. 3.5, this oscillatory behavior resembles the oscillations in Fig. 3.3. The dashed curves in

Fig. 3.5 correspond to non-resonant cases, while the solid curves show the resonant cases for the first three Efimov states near the threshold.

For $k \ll a^{-1}$, $A(k)$ and $B(k)$ can be written as a power series: $A(k) \sim A_0 + A_2 k^2 + \mathcal{O}(k^4)$ and $B(k) = k^{2\ell+1}(B_0 + B_2 k^2 + \dots) \sim B_0 k + \mathcal{O}(k^3)$ (with $\ell = 0$). As a result the relaxation rate reads

$$K_{\rm rel}(k) \sim \frac{1}{(A_0 + A_2 k^2)^2 + B_0^2 k^2}. \tag{3.33}$$

A_0 is very small for the resonant case and thus the competition between A_0 and $B_0^2 k^2$ gives the Wigner and NTR regimes. In the Wigner regime, A_0 is dominant and $K_{\rm rel}$ is a constant when k goes to zero, while in the NTR regime $K_{\rm rel} \sim 1/B_0^2 k^2$ since $B_0^2 k^2$ becomes dominant in the denominator of Eq. (3.33) as we increase k. In contrast to Eq. (3.27), the $A_2 k^2$ term no longer plays a significant role and we omit it from Eq. (3.33); indeed, $A_2^2 k^4$ is a higher order term which can be neglected, while the cross term $2A_0 A_2 k^2$ can be combined with $B_0^2 k^2$ which is equivalent to altering B_0 very slightly. Hence we obtain

$$K_{\rm rel}(k) \sim \frac{1}{A_0^2 + B_0^2 k^2}. \tag{3.34}$$

This equation captures the transition between the Wigner and NTR regimes. The transition is smooth whether or not the Efimov state is just above or below the threshold.

3.2.3 Two channel results for $a > 0$

When the atom-atom scattering length a is positive and large, there is a shallow dimer state just below the threshold, and we use the 2-channel model introduced in Sec. 3.1.3 to compute the three-body recombination rate for the process $B + B + B \to$

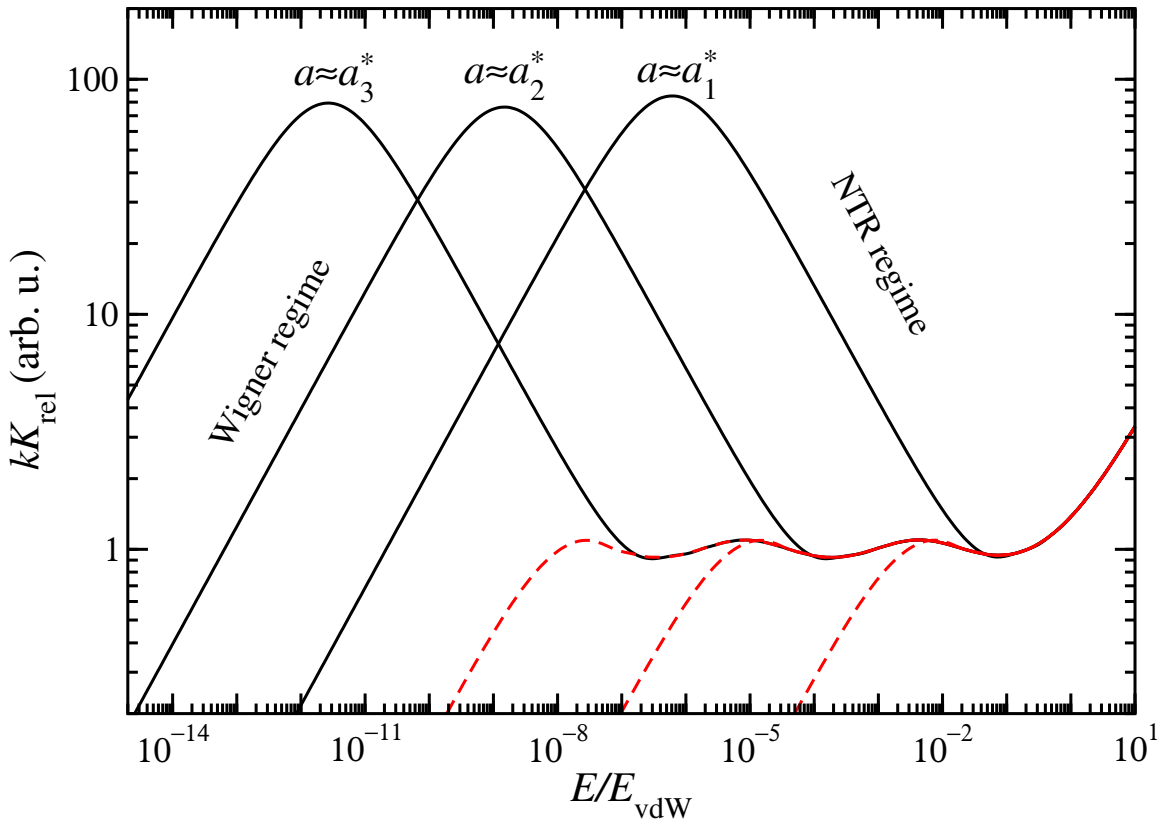

Figure 3.5. Black curves: vibrational relaxation rate for three values of $a = a_n^*$ as indicated, corresponding to the first, second and third Efimov state near the threshold, with $a_1^* = 11.45\ R_{\rm vdW}$, $a_2^* = 260.0\ R_{\rm vdW}$, and $a_3^* = 5902.0\ R_{\rm vdW}$, respectively . Red curves: relaxation rate for the non-resonant cases with $a = 3a_n^*$ for each curve, respectively.

$B + B_2$(shallow). As is well known [40], the zero energy limit of the three-body recombination rate K_3 is a log-periodic function of the dimer scattering length a, as shown in Fig. 3.6(a). Each maximum in Fig. 3.6(a) corresponds to an Efimov state at the dimer-atom threshold [40], which does not affect the energy dependence of K_3. However, each minimum in Fig. 3.6(a) corresponds to a critical value of a for which the energy dependence of K_3 is dramatically modified as shown in Fig. 3.6(b). The dashed line in Fig. 3.6(b) corresponds to a non-critical case, when $K_3(k)$ follows Wigner's threshold law for $k \ll a^{-1}$. The other three curves in Fig. 3.6(b) correspond to the three minima in Fig. 3.6(a), for which the three-body recombination rate displays a strongly suppressed behavior $K_3(k) \sim k^4$ for $k_{\rm NTS} \ll k \ll a^{-1}$, that we label the *Near Threshold Suppression* (or NTS) regime.

The numerical solution for the 2-channel model is obtained as follows. The regular matrix solution Φ is initialized at $R = R_0$ using boundary conditions corresponding to a hard wall, $\Phi(R_0) = 0$ and $\Phi'(R_0) = \mathbf{I}$, where $\mathbf{I}$ is the 2×2 unit matrix. After propagation, and recalling that $\ell = \ell_{\rm eff}$ for channel 1, and $\ell = 0$ for channel 2, the regular solution is matched to asymptotic solutions,

$$\Phi \mathbf{k}^{\ell+1} = \mathbf{f}\mathbf{A} + \mathbf{g}\mathbf{B}, \tag{3.35}$$

where $\mathbf{k}^{\ell+1} = \mathrm{diag}(k_1^{\ell_{\rm eff}+1}, k_2)$ and $\mathbf{f}$ and $\mathbf{g}$ are diagonal matrices containing the single channel asymptotic solutions $f_1 = j_{\ell_{\rm eff}}(k_1 R)$, $g_1 = n_{\ell_{\rm eff}}(k_1 R)$, $f_2 = \sin(k_2 R)$ and $g_2 = \cos(k_2 R)$. The matrices $\mathbf{A}$ and $\mathbf{B}$ are the real and imaginary parts of the Jost matrix $\boldsymbol{\mathcal{J}} = \mathbf{A} - i\mathbf{B}$. The expression of the S-matrix in terms of the Jost matrix reads

$$S_{21} = \sqrt{\frac{k_2}{k_1}}(\boldsymbol{\mathcal{J}}^* \boldsymbol{\mathcal{J}}^{-1})_{21} = 2i\sqrt{\frac{k_2}{k_1}}\frac{A_{22}B_{21} - A_{21}B_{22}}{\det(\boldsymbol{\mathcal{J}})}. \tag{3.36}$$

Using the power series of the Jost matrix elements when $k \ll a^{-1}$, we obtain

$$S_{21}(k_1) = k_1^2 \frac{C_0 + C_2 k_1^2}{D_0 + D_2 k_1^2}. \tag{3.37}$$

Recalling Eq. (3.11), we find

$$K_3 \sim \frac{1}{k_1^4} |S_{21}|^2 = \left| \frac{C_0 + C_2 k_1^2}{D_0 + D_2 k_1^2} \right|^2 . \tag{3.38}$$

For the values of a corresponding to the strongly suppressed NTS cases shown in Fig. 3.6(b), the Efimov states are not near the threshold. This implies that the S-matrix does not exhibit a resonant structure, i.e., it has no nearby pole, or equivalently, $\det(\boldsymbol{\mathcal{J}}) \neq 0$ or simply $D_0 \neq 0$ in the limit $k_1 \to 0$. Hence the low k_1 behavior of the three-body recombination rate K_3 is determined by the competition between C_0 and $C_2 k_1^2$ in Eq. (3.38). In the Wigner regime, C_0 is dominant and thus K_3 is nearly constant. Note that normally, the Wigner regime behavior is valid for $k_1 \ll a^{-1}$, while in the NTS case C_0 is vanishingly small and the Wigner regime is restricted to $k_1 \ll k_{\rm NTS} = \sqrt{|C_0/C_2|}$. As Fig. 3.6(b) clearly shows, there is a new type of behavior for $k_{\rm NTS} \ll k_1 \ll a^{-1}$, where $C_2 k_1^2$ in Eq. (3.37) is dominant, and thus $K_3 \sim k_1^4$. Note that the NTS regime is essentially an effective Wigner regime defined in Chap2.

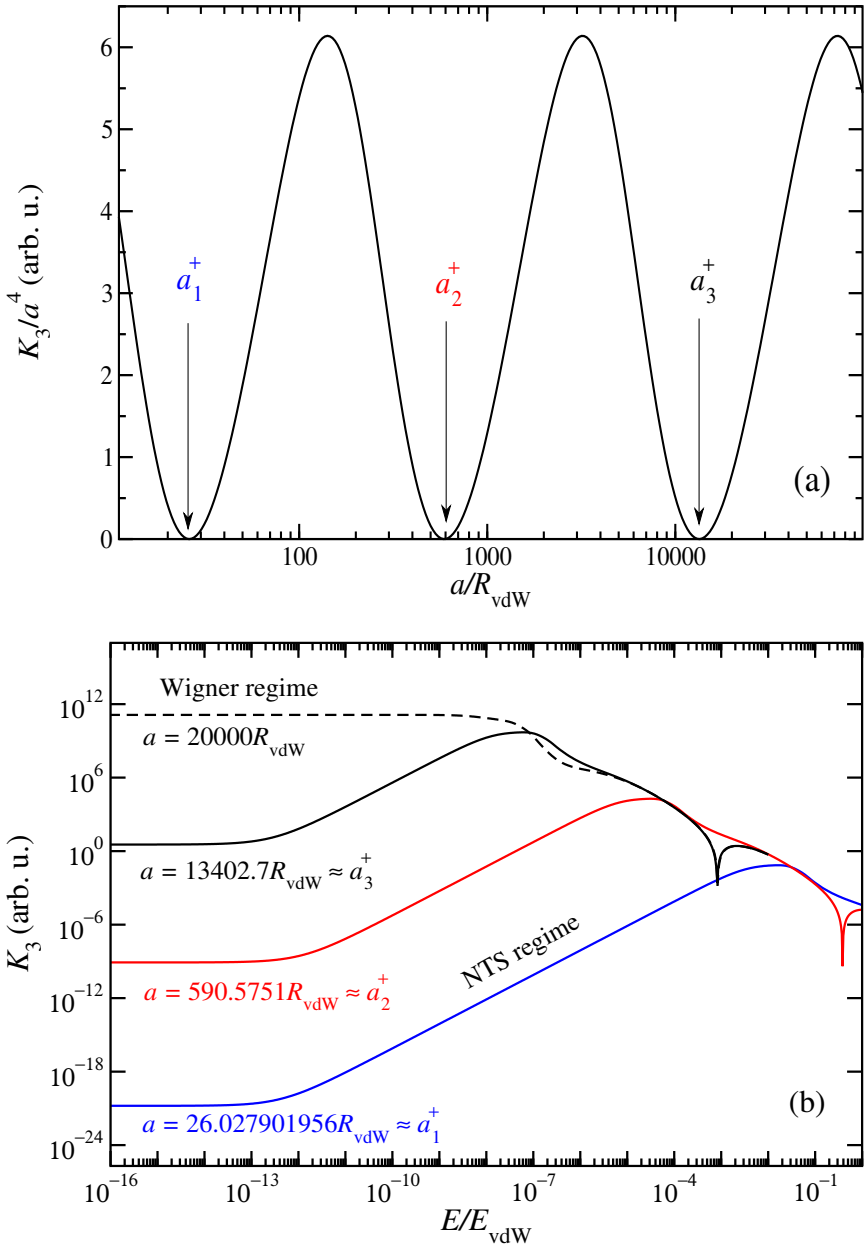

Figure 3.6. (a) K_3 in the limit $E \to 0$ as function of a. The positions a_n^+ of the minima are indicated and their values are given in the lower panel. (b) Dashed line: $K_3(E)$ for non-critical case, which displays only the Wigner regime behavior at low energy. Solid lines: first three critical cases corresponding to the minima in the upper panel. The minima of $K_3(E)$ appearing at energies between $E/E_{\rm vdW} = 10^{-4}$ and $E/E_{\rm vdW} = 1$ are due to destructive interference as explained in Ref. [63].

Chapter 4

Phase-Amplitude Approach for Two-body Scattering, Single-Channel without Barrier

4.1 Introduction for Milne's Equation

The phase–amplitude approach for Schrödinger's radial (or one-dimensional) equation was pioneered by Milne [71], and has since been used extensively in atomic and molecular physics [72, 73, 74, 75, 76, 77, 78, 79, 80, 81, 82, 83, 84], in chemical physics [85, 86], and in other areas of physics [87, 88, 89, 90, 91, 92, 93, 94, 95, 96, 97]. Although it was originally intended for tackling bound states, the phase–amplitude method is also applicable for scattering problems; indeed, Milne's approach is especially suitable in the framework of many-channel quantum defect theory [98, 99, 77, 100] because it makes it possible to construct optimal reference functions in each scattering channel.

The virtues of Milne's approach stem from the fact that phases and amplitudes are quantities which are well behaved in the energy domain, even across channel thresholds. Moreover, the phase–amplitude method allows for highly efficient numerical implementations, because the direct computation of highly oscillatory wave functions can be avoided entirely; instead, any solution of the radial equation is evaluated accurately in terms of the amplitude and phase functions, which have a simple radial dependence.

We consider the radial Schrödinger equation for a spherically symmetric potential $V(R)$,

$$\psi'' = U\psi, \qquad U = 2\mu\big(V_{\rm eff} - E\big), \tag{4.1}$$

where $V_{\rm eff}(R) = V(R) + \frac{\ell(\ell+1)}{2\mu R^2}$ is the effective potential, μ is the reduced mass of the two particles undergoing scattering, and $E > 0$ is the energy in the center-of-mass frame. Atomic units are used throughout. According to Milne [71], the *general* solution ψ of the radial equation (4.1) can be expressed in terms of an amplitude y and a phase θ,

$$\psi(R) = c\, y(R) \sin[\theta(R) + \theta_0], \tag{4.2}$$

where c and θ_0 are arbitrary constants. The amplitude satisfies the nonlinear equation

$$y'' = Uy + \frac{q^2}{y^3}, \tag{4.3}$$

and the phase $\theta(R)$ is constructed by integrating

$$\theta' = \frac{q}{y^2}. \tag{4.4}$$

In the equations above, q is arbitrary; the only restriction is $q^2 > 0$ in the amplitude Eq. (4.3).

4.2 Envelope Equation and its Basic Properties

We emphasize that the amplitude and phase appearing in Milne's parametrization (4.2) are not unique; indeed, any solution y of Eq. (4.3) together with the asso-

ciated phase θ will give a valid representation of ψ. This undermines the advantage of Milne's method in numerical applications, because the general solution $y(R)$ of Milne's nonlinear equation may have an oscillatory behavior in classically allowed regions, and the unique smooth amplitude is very difficult to find [74, 101, 102]. In order to overcome the difficulties and fully take advantage of the phase-amplitude parametrization, some of the important properties of Milne's equation are essential. In this section, its most important properties are presented.

4.2.1 Envelope equation

Despite this difficulty, Milne's nonlinear Eq. (4.3) has long been used for computational work. We remark that an *equivalent* formulation based on a *linear* equation exists [103, 104],

$$\rho''' = 4U\rho' + 2U'\rho, \tag{4.5}$$

but it remained overlooked in the physics community until recently [105].

We present here two different derivations of the envelope Eq. (4.5). The first derivation is very brief; namely, we substitute $y = \sqrt{\rho}$ in Eq. (4.3) and find

$$\rho'' = 2U\rho + \frac{1}{\rho}\left[\tfrac{1}{2}(\rho')^2 + 2q^2\right].$$

Next, we multiply both sides by ρ to obtain

$$\rho\rho'' = 2U\rho^2 + \frac{1}{2}(\rho')^2 + 2q^2, \tag{4.6}$$

which is still a nonlinear equation. However, we now take the derivatives of both sides,

$$\rho\rho''' = 4U\rho\rho' + 2U'\rho^2,$$

and we divide by ρ to finally obtain Eq. (4.5).

The second approach is similar to Milne's derivation [71] of Eq. (4.3). Namely, we consider two solutions (ϕ and χ) of the radial Schrödinger Eq. (4.1), and try to find a differential equation for their product

$$p \equiv \phi\chi.$$

Making use of Eq. (4.1) for ϕ and χ, we obtain

$$p'' = 2Up + 2\phi'\chi',$$

and we now evaluate its derivative,

$$p''' = 2U'p + 2Up' + 2U(\phi\chi' + \phi'\chi),$$

where we recognize $p' = \phi\chi' + \phi'\chi$, and we find again the envelope Eq. (4.5),

$$p''' = 4Up' + 2U'p.$$

Although Eq. (4.5) is of third order, its linearity makes it much more convenient than Milne's nonlinear Eq. (4.3). However, finding the non-oscillatory solution is still a difficult task. To overcome this obstacle, we devised a computational strategy for scattering problems ($E > 0$) which yields the smooth envelope in the asymptotic region, see Sec. 4.2.4, and an optimization scheme for searching the non-oscillatory solution in any classically allowed region Sec. 5.2.

4.2.2 Constraint for the envelope equation

The parameter q appears explicitly in Milne's nonlinear Eq. (4.3). However, q is absent from the envelope Eq. (4.5), even though it is used when integrating Eq. (4.16) to obtain the phase θ. This creates some ambiguity, which stems from the fact Eq. (4.3) is a second order differential equation, while the Eq. (4.5) is of third order. We now try to dispel the ambiguity and show that the two equations are equivalent. We first remark that although q does not appear in Eq. (4.5), it should be assumed implicitly; indeed, if we recast Eq. (4.6) in the form

$$\frac{1}{2}\rho\rho'' - U\rho^2 - \frac{1}{4}(\rho')^2 = q^2, \tag{4.7}$$

the expression on the left hand side can be interpreted as an invariant of the envelope Eq. (4.5), and any solution ρ will also obey Eq. (4.7) with a particular value of q^2. Recall that the equation above is equivalent with Milne's Eq. (4.3), which can thus be regarded as a constraint for the envelope equation. Indeed, as we discuss below, Eq. (4.7) should be used to enforce the correct initial conditions for ρ, such that they correspond to a fixed value for q.

To fully clarify the equivalence of Eqs. (4.3) and (4.5), let us compare the sets of initial conditions required in each case. When we initialize ρ at $R = R_0$, the following quantities are given

$$\rho(R_0), \qquad \rho'(R_0), \qquad \rho''(R_0),$$

which can be used in the constraint Eq. (4.7) evaluated at $R = R_0$ to obtain the value of q. Conversely, if q is considered given, we have

$$\rho(R_0), \qquad \rho'(R_0), \qquad q = \text{fixed},$$

which we commonly employ in practice. Eq. (4.7) is now used to obtain $\rho''(R_0)$, and thus initialize the solution of the envelope equation. Equivalently, for Milne's amplitude equation we consider the quantities as given

$$y(R_0), \qquad y'(R_0), \qquad q = \text{fixed}.$$

Moreover, the families of solutions for different values of q are all equivalent. Indeed, if y_1 is a solution of Eq. (4.3) for a given parameter q_1, then $y_2 = (q_2/q_1)^{\frac{1}{2}} y_1$ is a solution for q_2. Similarly, we have $\rho_2/q_2 = \rho_1/q_1$, and $\theta_2' = \theta_1'$. Varying the parameter q is entirely redundant, as the phase θ remains unchanged, therefore justifying the convenient choice $q = k$ used throughout this chapter.

Finally, we make use of the constraint in Eq. (4.7) to show that the choice $q = k$ is consistent with the initial condition $\rho = 1$ at $R = \infty$, which gives a convenient normalization for the envelope. Indeed, when $R \to \infty$, we have $V_{\text{eff}}(R) \to 0$ and thus $U(R) \approx U(\infty) = -k^2$ and $U' \approx 0$, while for the envelope we have

$$\rho(R) \approx \rho(\infty), \qquad \rho'(R) \approx 0, \qquad \rho''(R) \approx 0.$$

Substituting these asymptotic values in Eq. (4.7) we obtain

$$-U(\infty)\rho^2(\infty) = q^2,$$

and using $U(\infty) = -k^2$, we find the parameter q,

$$q = k\rho(\infty).$$

Conversely, if one prefers to choose a certain value for q, the equation above yields $\rho(\infty) = q/k$. However, as shown above, the normalization constant $\rho(\infty)$ is irrelevant; indeed, we have

$$\theta'(R) = \frac{q}{\rho(R)} = k\frac{\rho(\infty)}{\rho(R)},$$

which ensures

$$\theta'(R) \approx k, \qquad \text{when } R \to \infty,$$

and thus the phase function suitable for scattering problems has the desired behavior:

$$\theta(R) \approx kR, \qquad \text{when } R \to \infty.$$

4.2.3 Proof of the linear independence of ϕ^2, χ^2, $\phi\chi$

The product of any two solutions (ϕ, χ) of the radial equation obeys the envelope equation, and thus ϕ^2 and χ^2 are also valid solutions. We recall that Milne [71] derived his nonlinear equation for the amplitude y starting with the ansatz

$$y = \sqrt{\phi^2 + \chi^2},$$

and it was later observed by Pinney [106] that the general solution can be written as

$$y = \sqrt{a\phi^2 + b\chi^2 + 2c\phi\chi}.$$

The equation above reads as a simple linear combination, when expressed in terms of the envelope:

$$\rho = a\phi^2 + b\chi^2 + 2c\phi\chi. \tag{4.8}$$

Assuming ϕ and χ are linearly independent, we now show that the triplet $\{\phi^2, \chi^2, \phi\chi\}$ is a basis in the three-dimensional space spaned by the solutions of Eq. (4.5). In order to prove that $\{\phi^2, \chi^2, \phi\chi\}$ are linear independent solutions of Eq. (4.5), we will show that their linear combination vanishes if and only if $a = b = c = 0$.

Using Eq. (4.8), we substitute the expressions of ρ, ρ' and ρ'' in terms of ϕ and χ in Eq. (4.6), which yields after a straightforward but tedious manipulation,

$$W^2(ab - c^2) = q^2, \tag{4.9}$$

where $W = \phi\chi' - \phi'\chi$ is the Wronskian of ϕ and χ. Moreover, as shown in our previous section, any solution of the envelope equation obeys the invrariant/constraint:

$$\frac{1}{2}\rho\rho'' - U\rho^2 - \frac{1}{4}(\rho')^2 = q^2.$$

Thus, if the linear comibation in Eq. (4.8) vanishes, the invariant yields $q = 0$. However, due to the linear independence of ϕ and χ, we have $W \neq 0$, and Eq. (4.9) yields

$$ab = c^2.$$

We now consider the two possible cases: $c = 0$ and $c \neq 0$. In the trivial case ($c = 0$) we have $ab = 0$, i.e., either $a = 0$ or $b = 0$. Hence, $\rho = 0$ in Eq. (4.8) will imply the vanishing of the remaining coefficient (b or a, respectively). When $c \neq 0$, we substitute $c = \mathrm{sgn}(c)(ab)^{\frac{1}{2}}$ in Eq. (4.8), and obtain

$$\rho = \pm\psi^2,$$

where ψ is the linear combination

$$\psi = |a|^{\frac{1}{2}}\phi \pm \mathrm{sgn}(c)|b|^{\frac{1}{2}}\chi.$$

The algebraic sign ($\pm$) in the two expressions above is $\mathrm{sgn}(a) = \mathrm{sgn}(b)$. If $\rho = 0$, we have $\psi = 0$, which implies $a = b = 0$, because ϕ and χ are linearly independent. This contradicts the assumption $c^2 = ab \neq 0$ in the second case, which completes our proof. Thus, Eq. (4.8) does represent the general solution of the envelope equation.

4.2.4 The mapping $x = 1/R$

Phase-amplitude approaches are useful in numerical applications only if the solutions ρ and θ are well behaved. Specifically, the envelope should behave in a non-oscillatory fashion, which in turn ensures the smoothness of the phase function. In practice, there is considerable difficulty in finding the smooth envelope [74, 101], because the general solution of the envelope equation has an oscillatory behavior, as mentioned in Sec. 4.2. In this section, a novel computational strategy for obtaining the *smooth* envelope in the asymptotic region is presented. We emphasize that finding the unique, smooth solution is critically important for the efficiency and accuracy of numerical schemes for using the phase–amplitude method in general.

For clarity, we assume that $V(R)$ vanishes faster than R^{-1} asymptotically. As discussed in Sec. 4.3.1 (see also Sec. 4.2.2), we employ the initial condition $\rho = 1$ at $R = \infty$ when solving Eq. (4.5). However, rather than using the radial variable, it is highly advantageous to reformulate the envelope equation by *mapping* the asymptotic radial domain onto a finite interval. We developed a convenient and efficient numerical implementation based on a simple change of variable,

$$x = \frac{1}{R},$$

which allows to take fully into account the long-range tail of any potential. Thus, the *infinite* radial interval $R_1 < R < \infty$ is now mapped on a compact interval, $x_1 > x > 0$, with $x_1 = \frac{1}{R_1}$. The boundary R_1, i.e., the size of the interval $[0,\ x_1]$, will be chosen to ensure the desired level of accuracy.

We now regard the envelope as an x-dependent function, and we present the computational approach for finding the smooth solution of the envelope equation inside the interval $[0,\ x_1]$. First, we rewrite Eq. (4.5) using $x = \frac{1}{R}$ as the independent variable,

$$x^4\dddot{\rho} + 6x^3\ddot{\rho} + 6x^2\dot{\rho} - 4U\dot{\rho} - 2\dot{U}\rho = 0, \tag{4.10}$$

where dots above symbols denote derivatives with respect to x, e.g., $\dot{\rho} = d\rho/dx$. Recall that $U = 2\mu V_{\text{eff}} - k^2$. Next, we define

$$u \equiv \dot{\rho},$$

and we regard it as the unknown function. Making use of the initial condition $\rho = 1$ at $x = 0$, we write

$$\rho(x) = 1 + \int_0^x dt\, u(t),$$

which we substitute in the last term of Eq. (4.10) to obtain

$$\Big(4k^2 - 8\mu V_{\text{eff}} + x^4 D_x^2 + 6x^3 D_x + 6x^2 - 4\mu\dot{V}_{\text{eff}} S_x\Big)u = 4\mu\dot{V}_{\text{eff}}. \tag{4.11}$$

The operators D_x and S_x read

$$D_x u = \dot{u} = \frac{du}{dx}, \qquad S_x u = \int_0^x dt\, u(t).$$

We solve Eq. (4.11) using a spectral Chebyshev method [107, 108, 109, 110, 111, 112], i.e., we employ a small number of Chebyshev polynomials $T_n(x)$ with $n = 0, 1, 2, \ldots, N-1$, which are mapped onto the interval $[0, x_1]$. We expand the unknown function $u(x)$ in the Chebyshev basis, and the operators D_x and S_x are represented as finite $(N \times N)$ matrices [109, 110]. Thus, Eq. (4.11) becomes a simple linear system,

$$\mathbf{MA} = \mathbf{B}, \tag{4.12}$$

where the column $\mathbf{A}$ contains the Chebyshev coefficients of our unknown function,

$$u(x) = \sum_{n=0}^{N-1} A_n T_n(x),$$

$\mathbf{B}$ contains the Chebyshev coefficients for the expansion

$$4\mu \dot{V}_{\text{eff}}(x) = \sum_{n=0}^{N-1} B_n T_n(x),$$

and $\mathbf{M}$ is the matrix of the operator in Eq. (4.11),

$$M = 4k^2 - 8\mu V_{\text{eff}} + x^4 D_x^2 + 6x^3 D_x + 6x^2 - 4\mu \dot{V}_{\text{eff}} S_x.$$

Although the operator M is singular, its associated matrix ($\mathbf{M}$) in the finite Chebyshev basis is well conditioned and yields highly accurate solutions; indeed, the matrix $\mathbf{M}$ does admit an inverse, and the solution of Eq. (4.12) reads $\mathbf{A} = \mathbf{M^{-1}B}$. Fig. 4.1 depicts the error $\Delta\rho = \left|\rho^{(N)}(x_1) - \rho^{(N_{\max})}(x_1)\right|$ for the envelope evaluated at $x_1 = 0.04$. We varied the size of the Chebyshev basis from $N = 5$ to $N_{\max} = 200$, as shown in Fig. 4.1, which makes it readily apparent that the convergence with respect to N is robust. The smooth envelope is thus obtained as the unique solution; indeed, all the

other solutions oscillate infinitely fast near $x = 0$ ($R \to \infty$) and they are eliminated simply because highly oscillatory behavior cannot be accommodated by the finite number of polynomials.

We emphasize that the linearity of the envelope equation is crucially important for the feasibility of the approach presented here. Finally, the solution obtained inside the interval $[0,\ x_1]$ can now be used to initialize the propagation for $x > x_1$, i.e., $R < R_1$.

4.3 Integral Representation

4.3.1 Integral representation for the *full* phase shift

We now derive an expression for δ_ℓ which does not rely on the explicit evaluation of wave functions; instead, the phase shift will be extracted from an R-dependent phase function. We emphasize that the *true* value of δ_ℓ will be obtained, despite the modulo π ambiguity inherent in its customary definition.

We first introduce the envelope function

$$\rho = f^2 + g^2, \tag{4.13}$$

with f and g exact solutions of the radial Eq. (4.1) obeying the asymptotic behavior,

$$f(R) \xrightarrow{R\to\infty} \sin(kR - \ell\tfrac{\pi}{2}), \tag{4.14}$$

$$g(R) \xrightarrow{R\to\infty} \cos(kR - \ell\tfrac{\pi}{2}). \tag{4.15}$$

The phase function θ is constructed by integrating

$$\theta' \equiv \frac{d\theta}{dR} = \frac{k}{\rho}. \tag{4.16}$$

We remark that $\theta(R)$ is defined up to an integration constant, which can be chosen freely.

As shown by Milne [71], the general solution of the radial Eq. (4.1) can be represented exactly in terms of ρ and θ. In particular, the physical solution reads

$$\psi(R) = \sqrt{\rho(R)}\sin[\theta(R) - \theta(0)]. \tag{4.17}$$

Note that $\psi(R)$ vanishes explicitly at $R = 0$, while Eqs. (4.14), and (4.15) ensure a very simple asymptotic behavior for ρ and θ,

$$\rho(R) \xrightarrow{R\to\infty} 1, \tag{4.18}$$

$$\theta(R) \xrightarrow{R\to\infty} kR + \text{const.} \tag{4.19}$$

We now define the reduced phase

$$\tilde{\theta}(R) \equiv \theta(R) - kR, \tag{4.20}$$

and use Eqs. (4.18), and (4.19) to find the asymptotic behavior of Milne's parametrization (4.17),

$$\psi(R) \xrightarrow{R\to\infty} \sin[kR + \tilde{\theta}(\infty) - \theta(0)],$$

which is identical to the asymptotic behavior of ψ

$$\psi(R) \xrightarrow{R\to\infty} \sin(kR - \ell\tfrac{\pi}{2} + \delta_\ell), \tag{4.21}$$

where $k = \sqrt{2\mu E}$ is the momentum for the relative motion (in a.u.). Consequently, we obtain

$$\delta_\ell - \ell\tfrac{\pi}{2} = \tilde{\theta}(\infty) - \theta(0). \tag{4.22}$$

Making use of Eq. (4.20) we have $\theta(0) = \tilde{\theta}(0)$, and Eqs. (4.16) and (4.20) yield $\tilde{\theta}' = \frac{k}{\rho} - k$. Hence, Eq. (4.22) can be recast as an integral representation,

$$\begin{aligned} \delta_\ell - \ell\tfrac{\pi}{2} &= \tilde{\theta}(\infty) - \tilde{\theta}(0), \\ &= k\int_0^\infty dr \left[\frac{1}{\rho(r)} - 1\right]. \end{aligned} \tag{4.23}$$

We remark that the reduced phase $\tilde{\theta}(R)$ defined in Eq. (4.20) cannot be regarded as the nontrivial phase contribution, as it also includes the Bessel contribution (due to the centrifugal term). Therefore, strictly speaking, the equation above yields the *full* phase shift $(\delta_\ell - \ell\frac{\pi}{2})$.

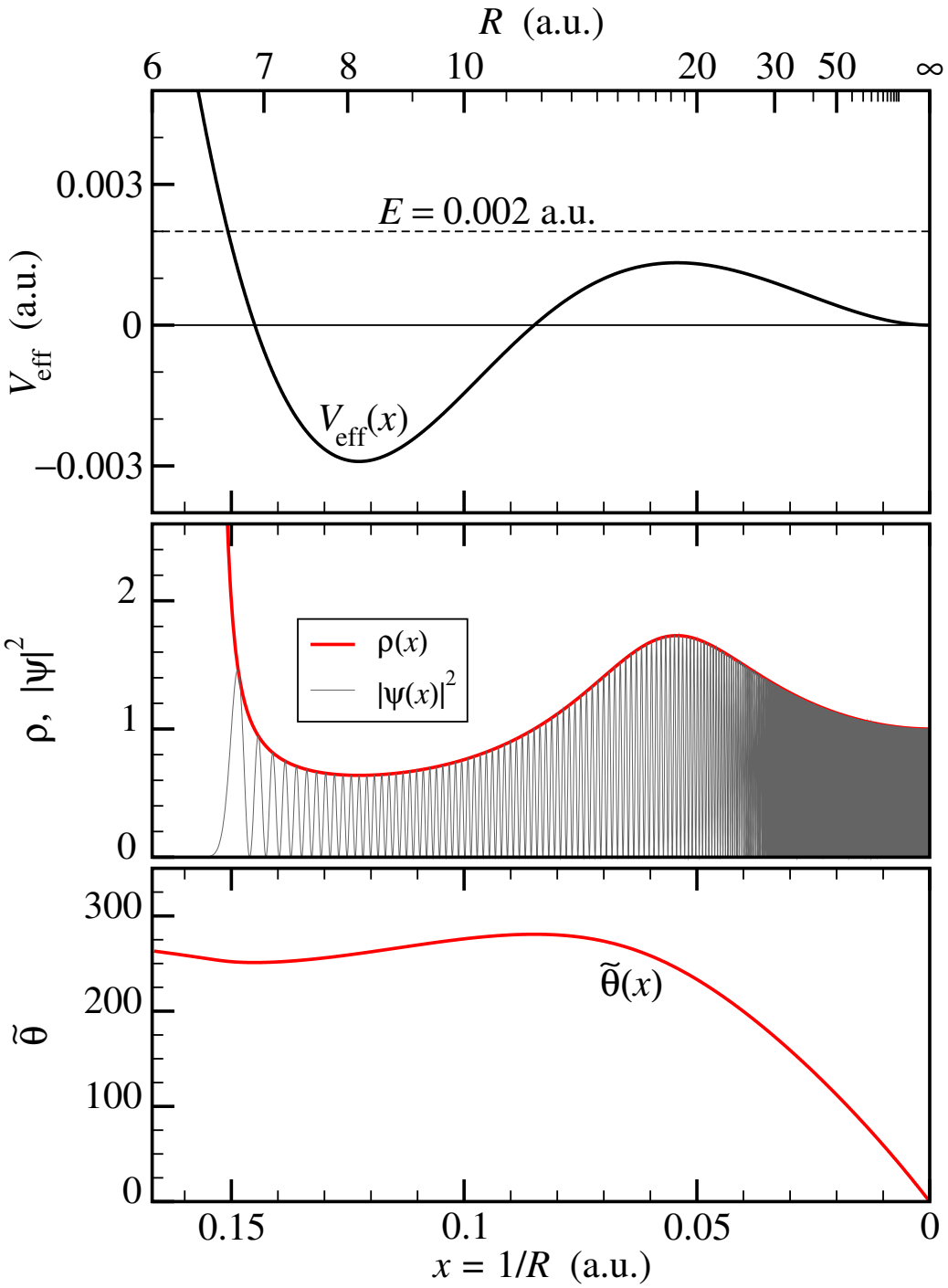

Figure 4.2. Upper: effective potential (for $\ell = 475$) as a function of $x = \frac{1}{R}$. $V(R)$ is given in Eq. (4.47). The values of R are indicated at the top. The horizontal dashed line marks the energy E. Middle: thin line (gray) for the wave function, thick line (red) for the envelope. Lower: reduced phase $\tilde{\theta}(x)$.

The advantage of the phase–amplitude method combined with the change of variable $x = \frac{1}{R}$ is readily apparent in Fig. 4.2, where we show the x-dependence of the reduced phase $\tilde{\theta}(x)$ and the envelope $\rho(x)$ along with $|\psi|^2$ for $\ell = 475$ and $E = 0.002$ a.u., for the potential energy used in Sec. 4.4.2, see Eq. (4.47). Note that the wave function in Fig. 4.2 was evaluated numerically using Eq. (4.17), i.e., $\psi = \sqrt{\rho}\sin(\theta - \theta_{R=0})$.

When the potential has a repulsive wall at short range, the formulation of the phase–amplitude approach based on the change of variable $x = \frac{1}{R}$ can be employed for the entire radial domain, as shown in Fig. 4.2. Indeed, the repulsive wall makes it possible to stop the inward propagation at $R_{\min} > 0$, which corresponds to a finite value $x_{\max} = \frac{1}{R_{\min}}$. We remark that, when the inward propagation of the reduced phase $\tilde{\theta}$ approaches the repulsive wall, it is convenient to convert it to the full phase θ using Eq. (4.20) at a point R_0 just outside the inner wall; for the remainder of the radial domain ($R < R_0$), one should propagate $\theta(R)$ instead of $\tilde{\theta}(R)$, because the former converges much faster than the latter. Indeed, if $V_{\text{eff}} \to +\infty$ when $R \to 0$, we have $\rho \to \infty$ and $\theta' \to 0$, while $\tilde{\theta}' \to -k$. In other words, $\theta(0)$ should be computed as

$$\theta(0) = kR_0 + k\int_{R_0}^{\infty} dr\, \frac{\tilde{\rho}(r)}{\rho(r)} - k\int_{R_{\min}}^{R_0} \frac{dr}{\rho(r)}, \tag{4.24}$$

which is independent of R_0. We remark that the integration need not extend fully to $R = 0$, because $R_{\min}$ is chosen inside the repulsive wall to ensure the contribution of the interval $0 < R < R_{\min}$ is entirely negligible. Consequently, the radial domain can be safely restricted to $R_{\min} < R < \infty$, which is mapped onto the compact interval $x_{\max} > x > 0$.

4.3.2 Generalization to potentials with a Coulomb term

So far, we assumed that the potential $V(R)$ vanishes faster than R^{-1} asymptotically. In this section we consider the general case when $V(R)$ contains a Coulomb term,

$$V_C(R) = \frac{Z_1 Z_2}{R}. \tag{4.25}$$

with $Z_{1,2}$ the electric charges of the two colliding particles. The remainder $(V - V_C)$ of the interaction potential is responsible for the phase shift δ_ℓ, which is obtained from the well known asymptotic behavior

$$\psi(R) \xrightarrow{R\to\infty} \sin\left[kR - \tfrac{C}{k}\ln(2kR) + \eta_\ell - \ell\tfrac{\pi}{2} + \delta_\ell\right], \tag{4.26}$$

where $\eta_\ell = \arg\Gamma(\ell + 1 + i\frac{C}{k})$ is the Coulomb phase shift [113], and $C \equiv \mu Z_1 Z_2$. Following the same steps as in the previous section, we use again Milne's parametrization (4.17) for the physical wave function, namely $\psi(R) = \sqrt{\rho(R)}\sin[\theta(R) - \theta(0)]$, with the phase θ behaving asymptotically as

$$\theta(R) \xrightarrow{R\to\infty} kR - \tfrac{C}{k}\ln(2kR) + \text{const}, \tag{4.27}$$

which is the generalized version of Eq. (4.19). Accordingly, the reduced phase is again defined such that it is finite asymptotically,

$$\tilde{\theta}(R) \equiv \theta(R) - kR + \tfrac{C}{k}\ln(2kR), \tag{4.28}$$

and thus the full phase shift reads

$$\delta_\ell - \ell\tfrac{\pi}{2} + \eta_\ell = \tilde{\theta}(\infty) - \theta(0), \tag{4.29}$$

which is the general form of Eq. (4.22).

In the Coulomb case, an integral representation can only be written if we divide the radial domain in two intervals. Indeed, unlike the previous section, $\tilde{\theta}$ now diverges logarithmically when $R \to 0$. Thus, we shall employ $\theta(R)$ for $R \leq R_0$ and $\tilde{\theta}(R)$ for $R \geq R_0$, with R_0 fixed arbitrarily. Specifically, we have

$$\begin{aligned} \theta(R_0) - \theta(0) &= k \int_0^{R_0} \frac{dr}{\rho(r)}, \\ \tilde{\theta}(\infty) - \tilde{\theta}(R_0) &= k \int_{R_0}^{\infty} dr \left[\frac{1}{\rho(r)} - 1 + \frac{C}{k^2 r} \right]. \end{aligned}$$

Adding the two equations above, and making use of Eq. (4.28) at $R = R_0$, we find

$$\begin{aligned} \delta_\ell - \ell \tfrac{\pi}{2} + \eta_\ell &= \tilde{\theta}(\infty) - \theta(0), \\ &= k \int_0^{R_0} dr \left[\frac{1}{\rho(r)} - 1 \right] + \tfrac{C}{k} \ln(2kR_0), \\ &+ k \int_{R_0}^{\infty} dr \left[\frac{1}{\rho(r)} - 1 + \frac{C}{k^2 r} \right], \end{aligned} \tag{4.30}$$

which represents the generalization of Eq. (4.23). Indeed, in the absence of the Coulomb term, i.e., setting $C = 0$ in the equations above, we have $\eta_\ell = 0$, and we recover the results of Sec. 4.3.1. We emphasize that the expression in Eq. (4.30) is independent of R_0, which we illustrate with numerical results in Sec. 4.4.1. Finally, we remark that Eqs. (4.23, 4.30) yield the true value of δ_ℓ unambiguously (not modulo π), and in the case of a purely Coulombic potential, Eq. (4.30) yields the true value of η_ℓ.

4.3.3 Envelope and phase functions

In order to use the approach outlined above in numerical applications, it is necessary to devise a reliable method for computing the envelope directly, rather than using Eq. (4.13). As shown in Sec. 4.2.1, ρ obeys a linear differential equation,

$$\rho''' - 4U\rho' - 2U'\rho = 0. \tag{4.31}$$

Therefore, we now regard the envelope $\rho = f^2+g^2$ in Eq. (4.13) as a particular solution of Eq. (4.5). Namely, we impose the asymptotic boundary condition $\rho(R) \to 1$, which makes the solution unique. As we shall see in Sec. 4.2.4, we initialize the envelope at $R = \infty$ and propagate it inward; accordingly, we also propagate the reduced phase $\tilde{\theta}$ inward from $R = \infty$.

Recall that Eq. (4.16) allows for an integration constant to be chosen freely when constructing the phase $\theta(R)$ or $\tilde{\theta}(R)$. The integration constant can be fixed, e.g., by setting the value of $\theta(0)$, or the value of $\tilde{\theta}(\infty)$. We prefer the latter, which is suitable when employing the inward propagation mentioned above; specifically, we choose

$$\tilde{\theta}(\infty) = 0,$$

and thus Eq. (4.22) reads

$$\delta_\ell = \ell\tfrac{\pi}{2} - \theta(0). \tag{4.32}$$

The reduced phase is constructed by direct integration; in the absence of a Coulomb interaction term, we have

$$\tilde{\theta}(R) = k\int_R^\infty dr\, \frac{\tilde{\rho}(r)}{\rho(r)}, \tag{4.33}$$

where $\tilde{\rho}$ denotes the reduced envelope

$$\tilde{\rho} \equiv \rho - 1.$$

In the Coulomb case we make use of $\tilde{\theta}'(r) = \frac{k}{\rho(r)} - k + \frac{C}{kr}$, see Eqs. (4.16) and (4.28), and thus the reduced phase reads

$$\tilde{\theta}(R) = k\int_R^\infty dr\,\left[1 - \frac{1}{\rho(r)} - \frac{C}{k^2 r}\right]. \tag{4.34}$$

In order to show that the integral above is well defined and yields a reduced phase obeying $\tilde{\theta}(\infty) = 0$, and also to justify that the full phase $\theta(R)$ has the asymptotic behavior (4.27), we write the envelope as an asymptotic series,

$$\rho(R) = 1 + \sum_{n\geq 1} \frac{b_n}{R^n}. \tag{4.35}$$

Assuming the potential has the long-range behavior

$$V(R) = \sum_{n\geq 1} \frac{C_n}{R^n}, \qquad \text{with} \;\; C_1 = C = \mu Z_1 Z_2,$$

we substitute the ansatz (4.35) in Eq. (4.5), and we obtain the coefficients b_n. In particular, for $n = 1$ we have $b_1 = C/k^2$, and thus the asymptotic behavior of the envelope reads

$$\rho(R) \approx 1 + \frac{C}{k^2 R} + \frac{b_2}{R^2} + \cdots .$$

Substituting the result above in Eq. (4.16) yields $\theta' \approx k - \frac{C}{kR} + \mathcal{O}(\frac{1}{R^2})$, which upon integration confirms Eq. (4.27), while the reduced phase in Eq. (4.34) has the asymptotic behavior

$$\tilde{\theta}(R) \approx \frac{\tilde{b}_1}{R} + \frac{\tilde{b}_2}{R^2} + \cdots \xrightarrow{R\to\infty} 0,$$

where the coefficients $\tilde{b}_n$ are expressed in terms of b_n, e.g., $\tilde{b}_1 = b_2 - b_1^2$.

For computational purposes, it is advantageous to employ the reduced envelope

$$\tilde{\rho} \equiv \rho - 1 - \tfrac{C}{k^2 r}. \tag{4.36}$$

Thus, we recast Eq. (4.34) in terms of $\tilde{\rho}$,

$$\tilde{\theta}(R) = k\int_R^\infty dr \frac{1}{\rho(r)} \left[\left(1 - \tfrac{C}{k^2 r}\right) \tilde{\rho}(r) - \left(\tfrac{C}{k^2 r}\right)^2 \right]. \tag{4.37}$$

The full phase shift in Eq. (4.30) can now be expressed in a form suitable for computation,

$$\begin{aligned} \delta_\ell &- \ell\tfrac{\pi}{2} + \eta_\ell = -\theta(0), \\ &= k\int_0^{R_0} \frac{dr}{\rho(r)} - kR_0 + \tfrac{C}{k}\ln(2kR_0) - \tilde{\theta}(R_0). \end{aligned} \tag{4.38}$$

We emphasize that $\tilde{\theta}$ should be computed using Eq. (4.37), because the integrand in Eq. (4.34) suffers from cancellation at large r. Thus, in the asymptotic region, $\tilde{\rho}$ should be obtained directly, rather than ρ itself; namely, we substitute $\rho = \tilde{\rho} + 1 + C/k^2R$ in Eq. (4.5) which becomes an equation for $\tilde{\rho}$. The numerical approach for solving the envelope equation is described in Sec. 4.2.4, where we show that the entire asymptotic region can be treated in a numerically exact fashion by mapping it onto a finite interval and using a spectral Chebyshev method.

4.3.4 Two-envelope formula for phase shifts

We now derive a formula involving two scattering potentials; if one of them is used as a reference case, this two-envelope integral representation makes it possible to compute the phase shift δ_ℓ directly. Recall that the simple integral representations (4.23) and (4.30) yield the *full* phase shift (including Bessel and Coulomb contributions). As shown in Sec. 4.4.2, accurate values of δ_ℓ at high ℓ cannot be obtained

using Eq. (4.23). Thus, in this section we formulate a two-envelope approach which can be used to compute accurate phase shifts for all partial waves. For the sake of generality, we consider two different potentials V_1 and V_2, each containing the same Coulomb interaction term (if present). For a given scattering energy, $E > 0$, and a partial wave ℓ, we make use of Eq. (4.29) for each potential, and we employ the convenient choice $\tilde{\theta}_1(\infty) = \tilde{\theta}_2(\infty)$ to find

$$\delta_\ell^{(2)} - \delta_\ell^{(1)} = \theta_1(0) - \theta_2(0), \tag{4.39}$$

Using $\theta'_{1,2} = k/\rho_{1,2}$, see Eq. (4.16), the phase difference above can be recast as an integral,

$$\delta_\ell^{(2)} - \delta_\ell^{(1)} = k \int_0^\infty dr \Big[\frac{1}{\rho_2(r)} - \frac{1}{\rho_1(r)} \Big]. \tag{4.40}$$

Although both $\theta_{1,2}(R)$ diverge when $R \to \infty$, the integral above is finite because the phase difference $\theta_1(R) - \theta_2(R) = \tilde{\theta}_1(R) - \tilde{\theta}_2(R)$ vanishes asymptotically. Note that in the asymptotic region we have $\rho_1 \approx \rho_2$, which can also hold in the inner region if $V_1 \approx V_2$. Thus, Eq. (4.40) will suffer from catastrophic cancellation, rendering it unsuitable for numerical applications. Nevertheless, we show next that a computationally robust integral representation based on the two-envelope approach can be formulated.

We choose $V_1 \equiv V_{\rm ref}$ as a reference potential (with the corresponding effective potential including both the centrifugal and Coulomb terms, see below), while $V_2 \equiv V = V_{\rm ref} + \hat{V}$ is the full interaction potential. The reduced envelope and phase are now defined relative to the corresponding reference quantities,

$$\begin{aligned} \hat{\rho} &= \rho - \rho_{\rm ref}, \\ \hat{\theta} &= \theta - \theta_{\rm ref}. \end{aligned} \tag{4.41}$$

We employ a nontrivial reference problem by setting

$$U_{\rm ref}(R) = -k^2 + \frac{\ell(\ell+1)}{R^2} + \frac{2C}{R}, \qquad C = \mu Z_1 Z_2, \tag{4.42}$$

and we use of Eqs. (4.39) and (4.40) with $U_1 = U_{\rm ref}$ given above and $U_2 = U = U_{\rm ref} + 2\mu\hat{V}$. Thus, the Bessel phase shift $(-\ell\frac{\pi}{2})$ and the Coulomb phase shift η_ℓ are both eliminated, and the phase shift δ_ℓ reads

$$\begin{aligned} \delta_\ell &= -\hat{\theta}(0), \\ &= -k\int_0^\infty dr \frac{\hat{\rho}(r)}{\rho(r)\rho_{\rm ref}(r)}. \end{aligned} \tag{4.43}$$

The reference envelope is the solution of Eq. (4.5),

$$\rho'''_{\rm ref} - 4U_{\rm ref}\,\rho'_{\rm ref} - 2U'_{\rm ref}\,\rho_{\rm ref} = 0, \tag{4.44}$$

with $U_{\rm ref}(R)$ given in Eq. (4.42), while the reduced envelope obeys a non-homogeneous differential equation,

$$\hat{\rho}''' - 4U\hat{\rho}' - 2U'\hat{\rho} = 4\hat{U}\rho'_{\rm ref} + 2\hat{U}'\rho_{\rm ref}, \tag{4.45}$$

which was obtained by combining Eqs. (4.5) and (4.44). In the equation above we used the notation $\hat{U} \equiv U - U_{\rm ref} = 2\mu\hat{V}$. Note that in the absence of a Coulomb term, we use $U_{\rm ref} = -k^2 + \frac{\ell(\ell+1)}{R^2}$, with $V_{\rm ref} = 0$ and $\hat{V} = V$, which is illustrated with numerical results in Sec. 4.4.2. Finally, we remark that in the absence of a Coulomb term one can also use the trivial choice $U_{\rm ref} = -k^2$ with $\theta_{\rm ref}(R) = kR$, which yields $\hat{\theta}$ identical to $\tilde{\theta}$ in Eq. (4.20), thus recovering the integral representation of the full phase shift given in Sec. 4.3.1.

In practical applications, one first solves Eq. (4.44) for the reference envelope, which is subsequently used in Eq. (4.45). The latter is solved to obtain $\hat{\rho}$, and thus the full envelope is obtained: $\rho = \rho_{\text{ref}} + \hat{\rho}$. We remark that the numerical approach used for the homogeneous envelope equation, see Sec. 4.2.4, can also be employed for the non-homogeneous differential Eq. (4.45). The two-envelope approach is fully general, but is especially useful when $\hat{U} = 2\mu\hat{V}$ is small, such that $|\hat{\rho}| \ll \rho \approx \rho_{\text{ref}}$, and thus $\hat{\theta}$ and δ_ℓ will also be small.

4.4 Numerical Examples

We now apply the integral representations and show that they yield highly accurate results. Our first example is the Coulomb potential, which we use as a test case for the integral representation (4.38). The two-envelope formula, see Eqs. (4.39) and (4.43), will be employed and tested in Sec. 4.4.2.

4.4.1 The Coulomb potential

In the case of a purely Coulombic potential, Eq. (4.38) yields the Coulomb phase shift,

$$\eta_\ell = \ell\tfrac{\pi}{2} - kR_0 + \tfrac{C}{k}\ln(2kR_0) + k\int_0^{R_0}\frac{dr}{\rho(r)} - \tilde{\theta}(R_0), \tag{4.46}$$

with $\tilde{\theta}$ given Eq. (4.37). The result above is independent of R_0, as depicted in Fig. 4.3. Indeed, we show that our approach is robust and accurate by comparing the value of η_ℓ obtained using Eq. (4.46) with the exact value $\eta_\ell^\Gamma \equiv \arg\Gamma(\ell + 1 + i\frac{C}{k})$ for $C = -1$, $k = 0.1$ and $\ell = 5$. Our integral representation yields the value $\eta_\ell = -20.22421961527$, while the analytical expression gives its value modulo 2π, namely $\eta_\ell^\Gamma = -1.3746636937335435$. Their difference equals an integer multiple of 2π to a

high degree of precision: $(\eta_\ell - \eta_\ell^\Gamma)/2\pi = -3(1 \pm 10^{-13})$. Fig. 4.3 depicts the relative error $|(\eta_\ell - \eta_\ell^\Gamma + 6\pi)/\eta_\ell|$ as a function of R_0.

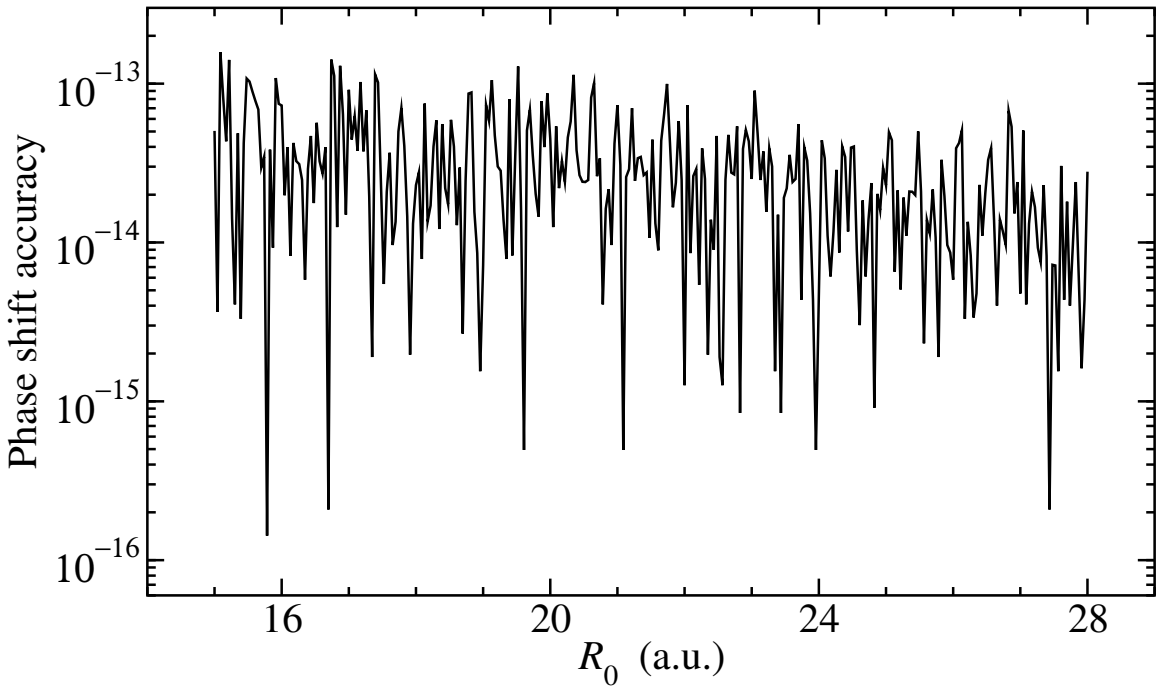

Figure 4.3. Relative error of the computed Coulomb phase shift η_ℓ for $C = -1$, $k = 0.1$ and $\ell = 5$. Eq. (4.46) yields a highly accurate result that is independent of R_0.

4.4.2 Results for an inter-atomic potential with long-range behavior of the type $V(R) \sim -\frac{C_3}{R^3}$

For our second example we use both integral representations, i.e., Eq. (4.23) for the full phase shift and the two-envelope formula (4.43) which yields the phase shift directly. We employ the potential energy, which mimics the potential of the $^1\Sigma_u^+$ state of Sr_2,

$$V(R) = C_{\rm wall} \exp\left(-\frac{R}{R_{\rm wall}}\right) - \frac{C_3}{R^3 + R_{\rm core}^3}, \tag{4.47}$$

with $C_{\text{wall}} = 10$, $R_{\text{wall}} = 1$, $R_{\text{core}} = 5$ and $C_3 = 18$ (all in atomic units), and the reduced mass $\mu = \frac{m}{2}$, where m is the mass of ^{88}Sr. We computed phase shifts for $E = 0.01$ a.u. ≈ 0.272 eV for a wide range of partial waves. The upper panel in Fig. 4.4 depicts the ℓ dependence of the phase shift, while the lower panel shows the partial-wave terms of the elastic cross section, $\sigma_\ell = \frac{4\pi}{k^2}(2\ell+1)\sin^2\delta_\ell$. An exceedingly large number of partial waves contribute to the cross section; note that the dominant contribution stems from very high partial waves ($\ell > 5000$). For a fully converged value of the elastic cross section, we have computed phase shifts up to $\ell = 10^5$.

Recall that our integral representations yield the true value of the phase shift (not modulo π) which has a rather simple ℓ-dependence; this suggests that interpolation schemes could be used to drastically reduce the number of partial waves for which phase shifts need to be computed. This added advantage is illustrated in Fig. 4.5, where we compare the true phase shift with its modulo π version. Moreover, our approach is not restricted to integer values of ℓ, and makes it possible to use non-integer values of ℓ as interpolation points; thus, highly accurate interpolation methods with non-uniform grids, such as Chebyshev interpolation, can be employed.

Regarding the practical aspects of the computation, some remarks are in order. We first emphasize that, using the computational approach presented in Sec. 4.2.4, the simple integral representation (4.23) and the two-envelope formula (4.43) can be implemented numerically such that they both yield accurate results. However, when using the integral representation (4.23) for the *full* phase shift, the value of δ_ℓ obtained from Eq. (4.32) will gradually lose precision at very high ℓ. Indeed, for $\ell \to \infty$ we have $\delta_\ell \to 0$ while $\theta(0) \approx \ell\frac{\pi}{2}$. Therefore, the simple integral representation (4.23) must be avoided at high ℓ because of the catastrophic cancellation in Eq. (4.32), even though $\theta(0)$ can still be computed accurately. Consequently, when ℓ becomes extremely large, δ_ℓ should instead be computed using the two-envelope formula derived in Sec. 4.3.4.

Although the two-envelope formula is highly accurate for all partial waves, Eq. (4.23) has the advantage of much greater simplicity and could be used at low ℓ, provided that it is sufficiently accurate. A simple rule of thumb exists for finding the highest partial wave for which Eqs. (4.23) and (4.32) yield accurate results. Namely, the two-envelope formula needs to replace the simple formula only if ℓ is high enough for the centrifugal term to become dominant over $V(R)$. We show next that the simple formula is indeed accurate at low ℓ; moreover, it is less expensive computationally compared to the two-envelope approach, which requires twice the amount of numerical work. The highest partial wave, $\ell_{\max}$, for which the simple formula is still accurate can be estimated as follows; we extract $\ell_{\max}$ by equating the depth of the potential well, $V_D = |V(R_{\text{bottom}})|$, which sets the energy scale at short range, with the centrifugal term evaluated at R_{bottom}, the location of the minimum of $V(R)$. Namely, we have $\ell_{\max}(\ell_{\max}+1) = 2\mu R^2_{\text{bottom}} V_D$. Thus, for the potential used in our example we estimate the simple formula to maintain high accuracy for $\ell \lessapprox 460 = \ell_{\max}$, which we confirm below. Note that in the high energy limit we have $|V(R)| \ll E$, and the two-envelope formula should be used for all partial waves ℓ, because all phase shifts δ_ℓ are vanishingly small when $E \to \infty$.

We first performed a test for the Bessel case, $V_{\text{eff}} = \frac{\ell(\ell+1)}{2\mu R^2}$, with $V = 0$, in order to show that the two-envelope formula is robust and accurate even for very high ℓ. Namely, we computed directly the vanishingly small difference between the Bessel phase shifts for ℓ_1 and ℓ_2 which are nearly equal. We used $\ell_1 = \ell$ and $\ell_2 = \ell - \frac{1}{\ell^2}$, for which the exact value of $\delta_\ell = \delta_B(\ell_2) - \delta_B(\ell_1)$ is $\delta_\ell = \frac{\pi}{2\ell^2}$, where $\delta_B(\ell) = -\ell\frac{\pi}{2}$ denotes the Bessel phase shift. The relative error of the numerical value δ_ℓ obtained with the two-envelope formula is shown in Fig. 4.6, confirming that high accuracy is preserved at high ℓ, despite the smallness of δ_ℓ. In contrast, if the *exact* values of $\delta_B(\ell_{1,2})$ are subtracted numerically, the loss of accuracy is significant and becomes catastrophic

at very high ℓ, see Fig. 4.6. This also illustrates that the failure of Eq. (4.32) at high ℓ cannot be avoided, as it is due to the cancellation of nearly equal quantities. Nevertheless, Eq. (4.32) is sufficiently accurate at low ℓ. Indeed, we performed a test for the simple integral representation (4.23). Assuming the two-envelope formula is numerically exact, the relative error for δ_ℓ computed using Eqs. (4.23) and (4.32) for the nontrivial potential energy (4.47) is shown in Fig. 4.7, which makes it readily apparent that the simple formula is highly accurate for partial waves $\ell \lessapprox 460$, while significant loss of precision only occurs for much higher ℓ.

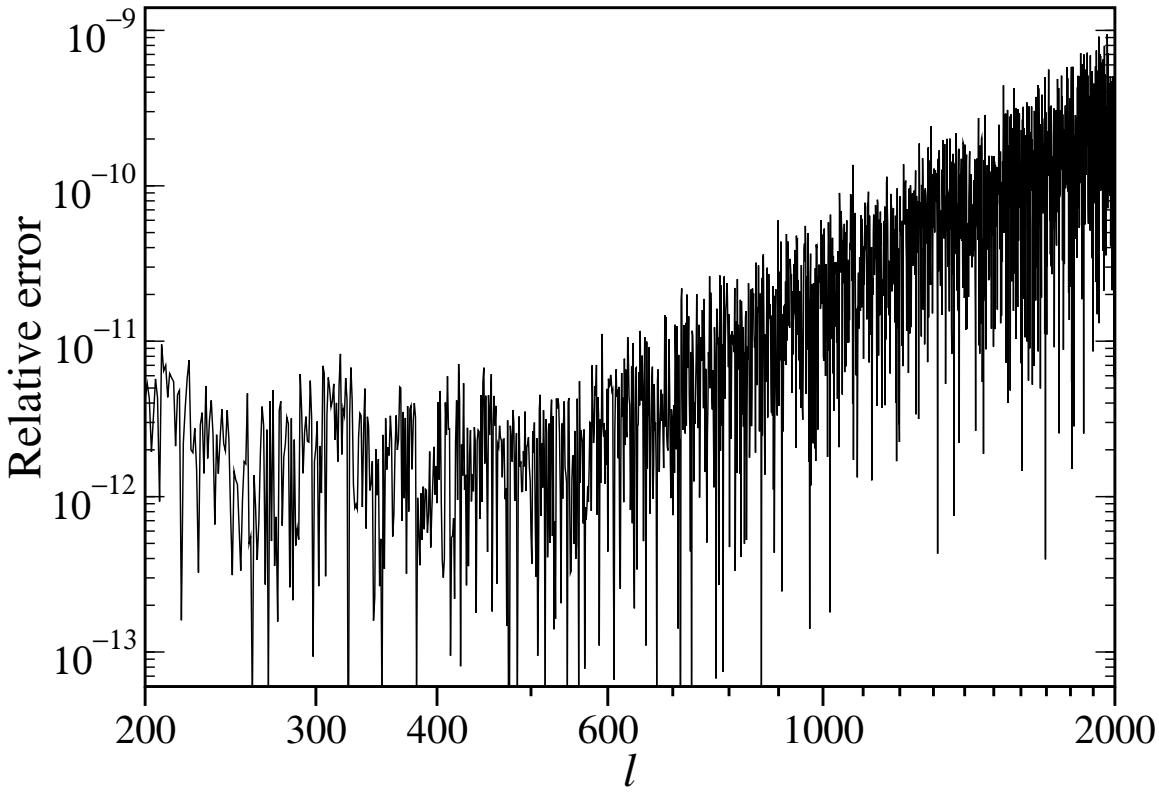

Figure 4.7. Comparison of the simple integral representation (4.23) and the two-envelope formula (4.43). The simple integral representation is highly accurate for $\ell \lessapprox 460$, and then gradually loses accuracy for higher ℓ.

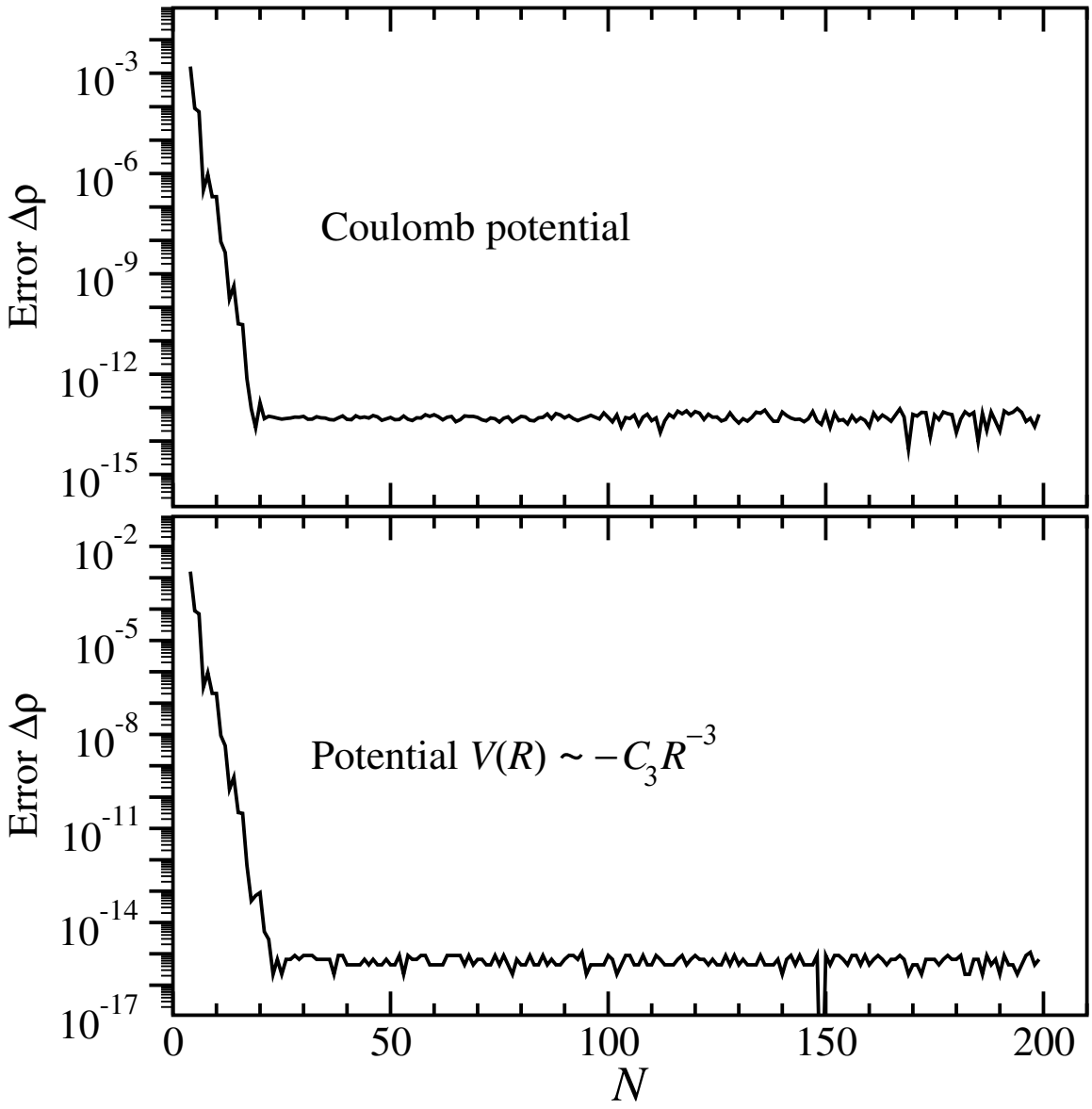

Figure 4.1. Upper: convergence test for an attractive Coulomb potential with $C = -1$, for $\ell = 5$ and $k = 0.1$ a.u. The horizontal axis is the size N of the Chebyshev basis, while the the vertical axis is the error for the envelope. Lower: same as the upper panel, for the potential $V(R)$ given in Eq. (4.47), for $\ell = 475$ and $E = 0.002$ a.u.

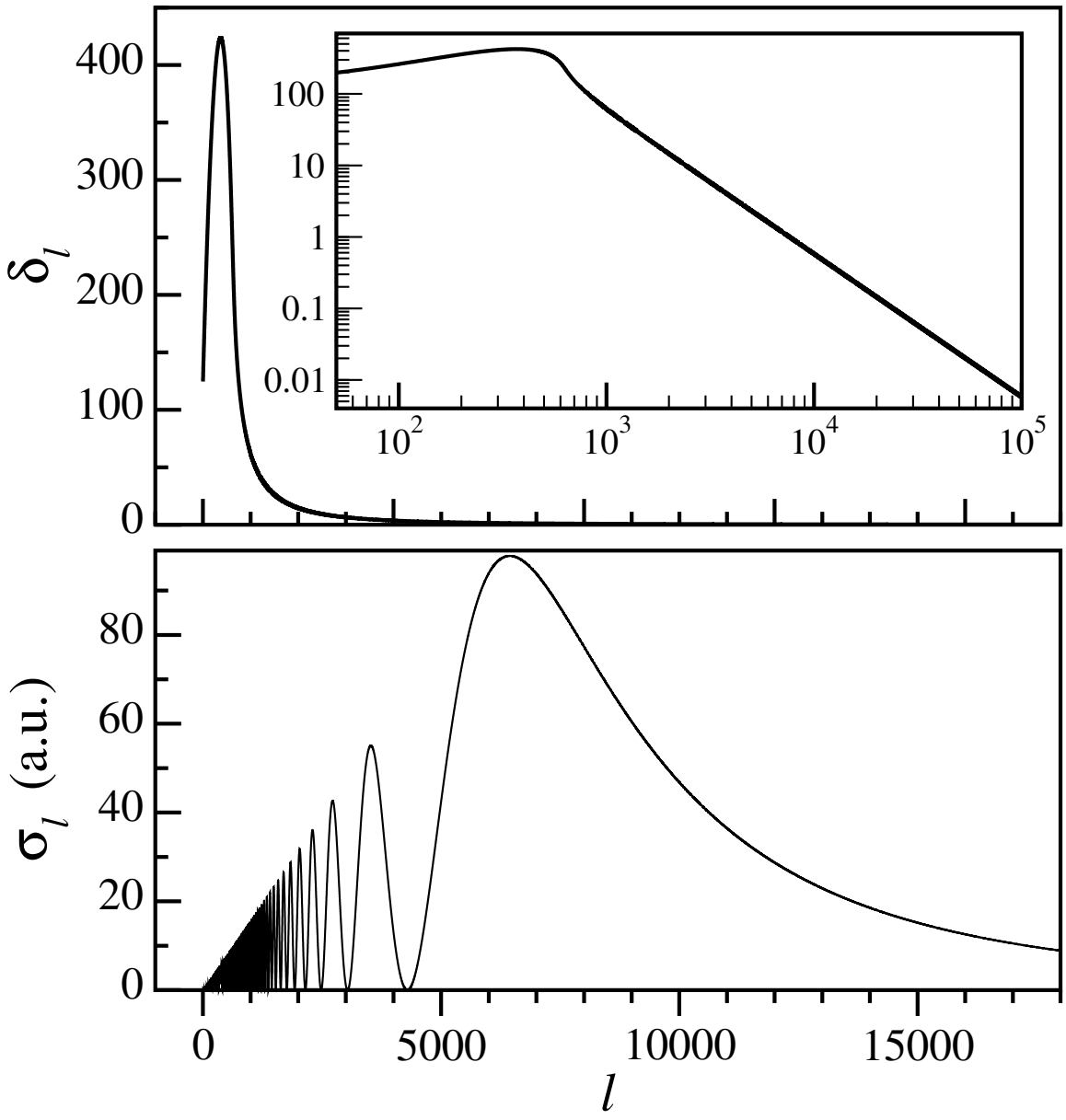

Figure 4.4. Phase shifts and cross section terms $\sigma_\ell = \frac{4\pi}{k^2}(2\ell+1)\sin^2\delta_\ell$ for the potential energy in Eq. (4.47) for $E = 0.01$ a.u.

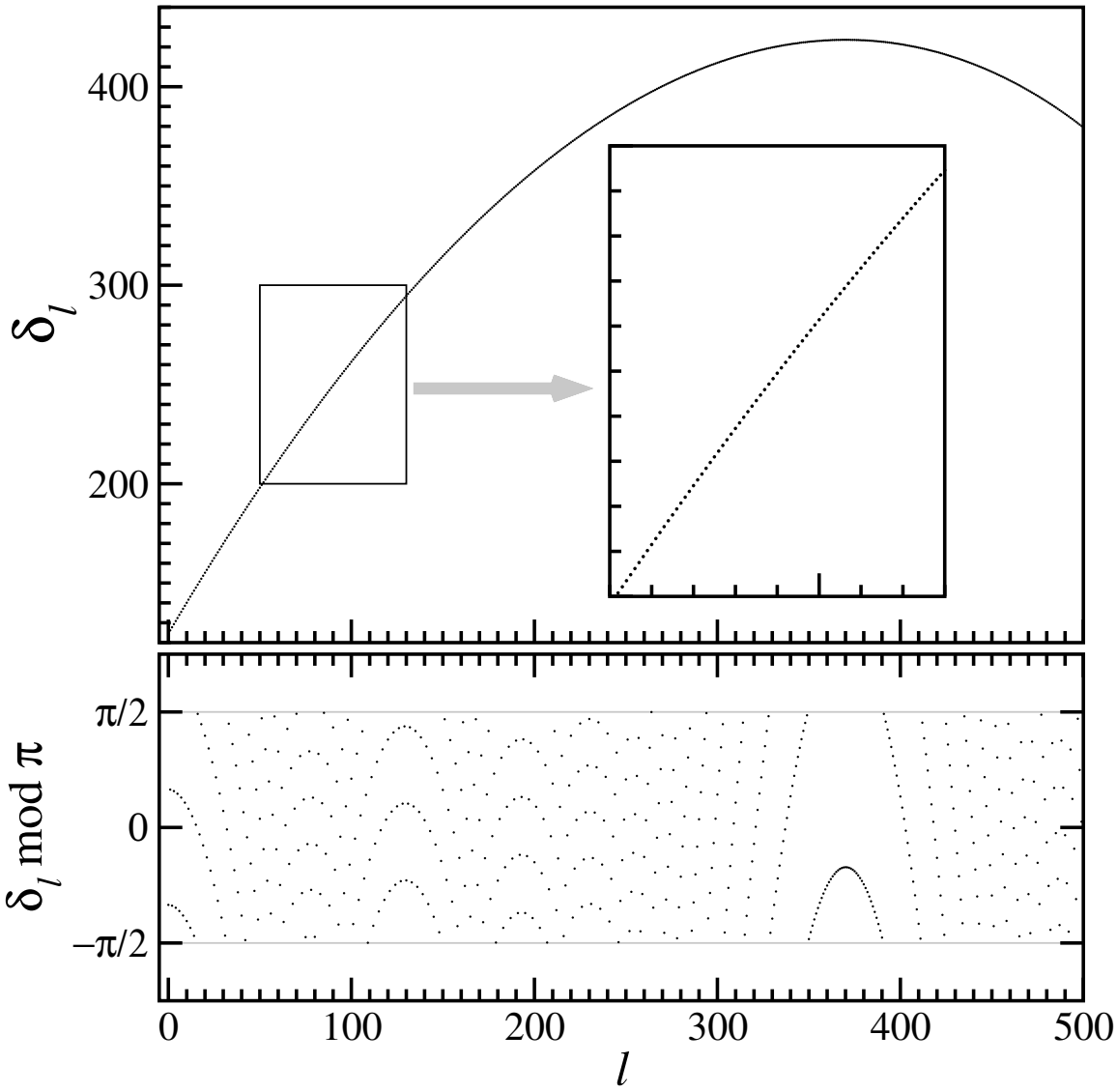

Figure 4.5. Phase shift δ_ℓ corresponding to the R^{-3} potential in Eq. (4.47) and $E = 0.01$ a.u., for discrete integer values of ℓ. Upper: true value of δ_ℓ. Inset: zoom on discrete values. Lower: δ_ℓ mod π. Note the vastly different scales used for the vertical axis in the two panels.

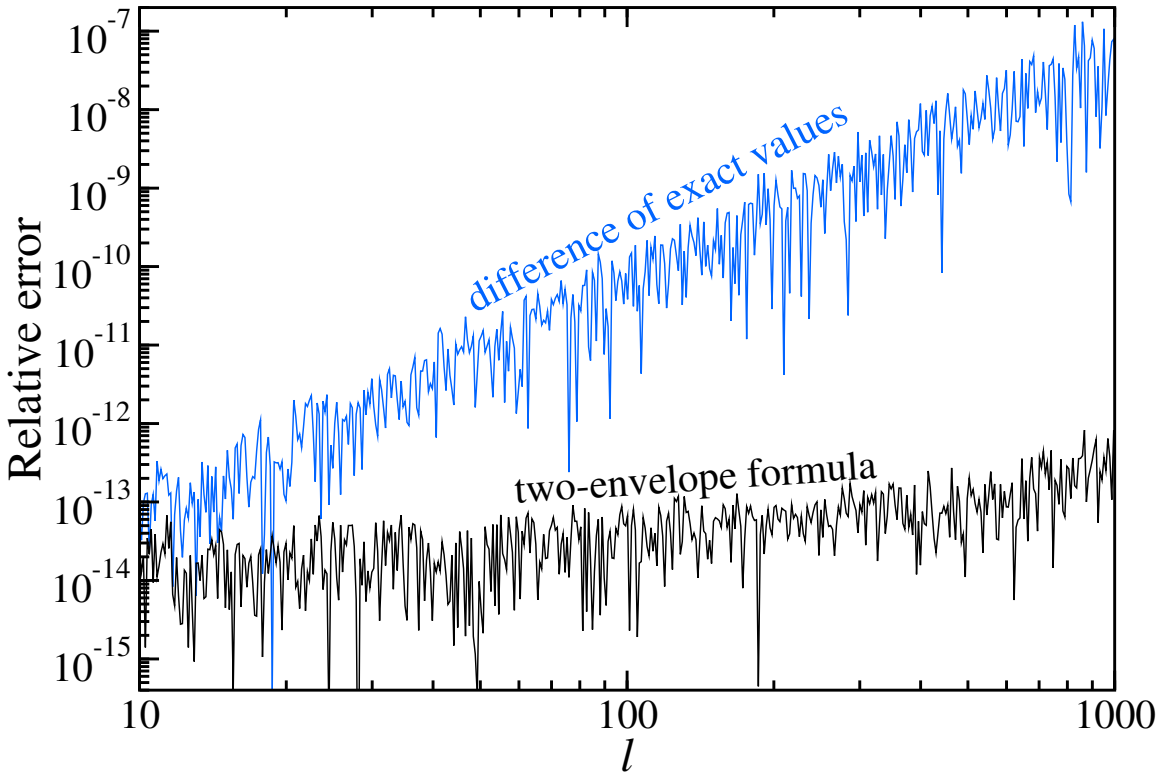

Figure 4.6. Relative error for the Bessel test. Blue line for the difference of the exact Bessel phase shifts, see text; black line for the two-envelope formula.

Chapter 5

Phase-Amplitude Approach for Two-body Scattering, Single-Channel through Barrier

5.1 Introduction

In Chapter 4,we derived an integral representation for scattering phase shifts based on Milne's phase-amplitude formalism [71]. Although the main result is fully general, our computational approach was limited to the case of a single classically allowed region; thus, if the (effective) potential had a barrier, our simple approach was restricted to scattering energies above the top of the barrier. In this chapter we extend our formalism to the much more interesting case of scattering at energies below the top of the barrier. Namely, we consider the scattering problem for an effective potential with a large barrier separating two classically allowed regions, and we develop an approach which makes possible the continuation of Milne's phase function $\theta(R)$ from the asymptotic region through the barrier and into the inner region. As shown in the previous chapter, the value of $\theta(R)$ at $R = 0$ yields the scattering phase shift δ_ℓ, which will be expressed in terms of quantities obeying a simple energy dependence; this will allow the extraction of highly accurate resonance widths, and will prove especially useful for ultra-narrow resonances.

5.2 Optimization

We now introduce a simple optimization method for finding the smooth envelope in any classically allowed region. Recall that in Sec. 4.2 we rewrite the most general solution of the envelope Eq. (4.5),

$$\rho = A\phi^2 + B\chi^2 + 2C\phi\chi \ , \tag{5.1}$$

where A, B, C are regarded as arbitrary constants.

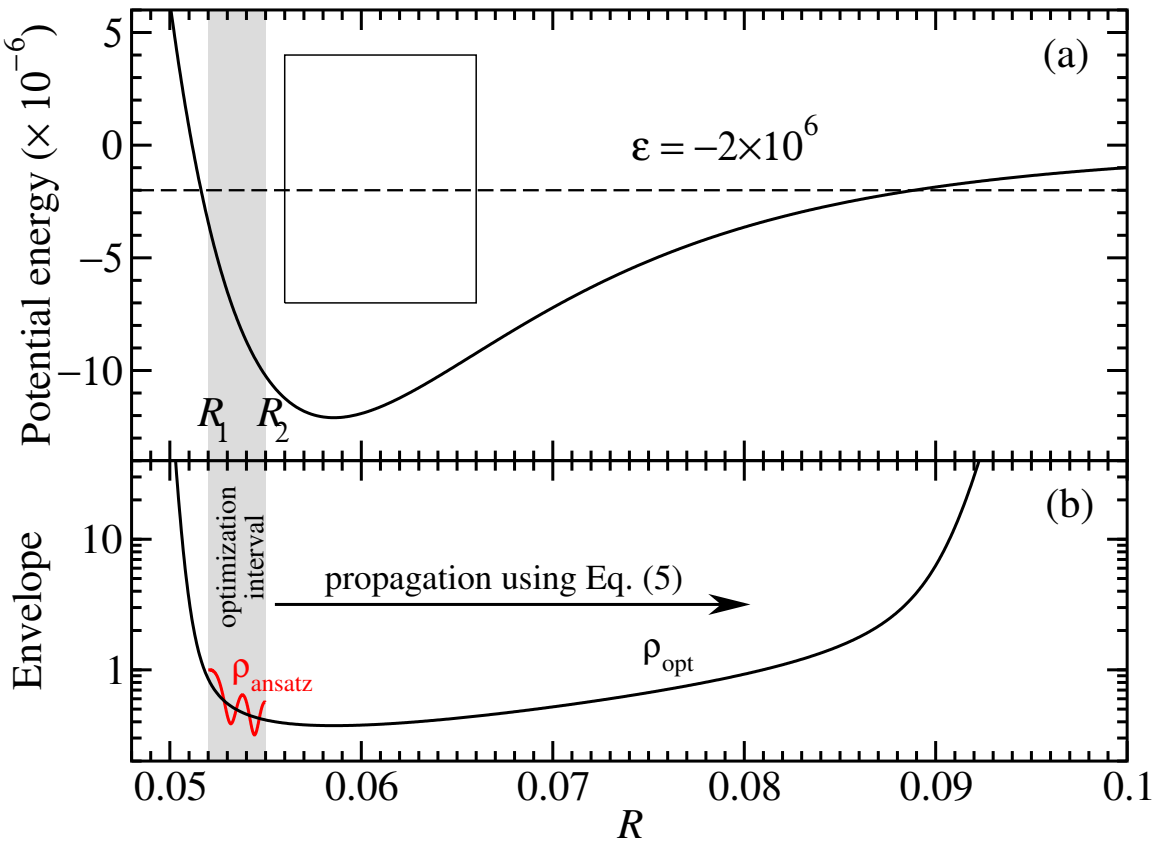

Figure 5.1. (a) Potential energy, Eq. (5.3), used for optimization. Rectangle corresponds the ranges of R and ε in Fig. 5.2. Shaded area marks the optimization interval. (b) Red line for $\rho_{\text{ansatz}} = \phi^2 + \chi^2$, corresponding to $A = B = 1$, $C = 0$, and black line for $\rho_{\text{opt}} = A\phi^2 + B\chi^2 + 2C\phi\chi$ with $A = 0.8533850906254$, $B = 1.245534003812$, $C = -0.2508388899674$, which was propagated outside the optimization interval using Eq. (4.5).

We first compute two linearly independent solutions ϕ and χ of Eq. (4.1) within a narrow interval $[R_1, R_2]$ inside a classically allowed region. Note that, for the optimization to be effective, the interval $[R_1, R_2]$ should cover one or two oscillations of ϕ and χ. Moreover, by computing $\phi(R)$ and $\chi(R)$ with high accuracy, we ensure that $\rho(R)$ in Eq. (5.1) is numerically exact within $[R_1, R_2]$, and we labeled it $\rho_{\rm exact}(R)$. We emphasize that for arbitrary parameters A, B, C, the envelope will be oscillatory. Next, we expand the exact envelope over the interval $[R_1, R_2]$ in a *small* polynomial basis of size $N \lessapprox 20$, such that it cannot reproduce the oscillations of $\rho_{\rm exact}$, in effect downgrading it to an approximate envelope, $\rho_{\rm approx}$. For arbitrary parameters (A, B, C), the latter will be a poor approximation, i.e., the error $\delta\rho = \|\rho_{\rm exact} - \rho_{\rm approx}\|$ will be large. However, when the parameters are precisely optimized such that the envelope has a non-oscillatory behavior, the error $\delta\rho$ vanishes because the small basis is sufficient to accurately reproduce the smooth envelope. A standard optimization subroutine is used to minimize the error function,

$$\delta\rho \equiv \max_{x\in[R_1,R_2]} \big|\rho_{\rm exact}(Q;R) - \rho_{\rm approx}(Q;R)\big|, \tag{5.2}$$

over the parameter space $Q \equiv (A,\, B,\, C|q)$. We remark that Eq. (4.9) represents a constraint for A, B, C, because q is assumed fixed, and thus the parameter space $Q \equiv (A,\, B,\, C|q)$ is only two dimensional as described in Sec. 4.2. Our implementation uses Chebyshev polynomials, $T_n(R) = \cos[n\,\mathrm{acos}(R)]$, for the interpolation $\rho_{\rm approx} = \sum_{n=0}^{N-1} c_n(Q) T_n(R)$. The optimized (smooth) envelope is then used as an initial condition for Eq. (4.5), and $\rho(x)$ is propagated on both sides of the initial working interval, to cover the entire R-domain.

As a first application, we consider the time-independent radial Schrödinger equation (4.1), with $0 < R < \infty$ and $U(x) = \frac{2\mu}{\hbar^2}[V(R) - E] + \ell(\ell+1)/R^2$, where μ is the reduced mass, $V(R)$ the interaction potential, and $\ell(\ell+1)/R^2$ the centrifugal term

for a given partial wave ℓ. To simplify notations, we use the van der Waals units with $E_{\rm vdW} = (2\mu|C_n|/\hbar^2)^{\frac{1}{n-2}}$. As an illustrative example, we use $U(R) = -\varepsilon + V(R)$ with

$$V(R) = -\frac{1}{R^6} + V_0 e^{-\gamma R}, \tag{5.3}$$

where $V_0 = 1.55 \times 10^{12}$ and $\gamma = 200$, which mimics the $a^3\Sigma_u^+$ potential curve for Cs_2. The shaded area in Fig. 5.1a between $R_1 = 0.052$ and $R_2 = 0.055$ marks the optimization interval for scaled energy $\varepsilon = -2 \times 10^6$. The solutions ϕ and χ are initialized at R_1 with $\phi = 0,\ \phi' = k_1 = \sqrt{-U(R_1)}$ and $\chi = 1,\ \chi' = 0$, such that ϕ and χ are similar to sine and cosine respectively. Thus a good choice for the initial ansatz is $\rho_{\rm ansatz} = \phi^2 + \chi^2$, shown as the oscillatory red curve in Fig. 5.1b. Finally, we minimize $\delta\rho$ and find the optimal values for A, B, C which give the smooth envelope $\rho_{\rm opt}(R)$ shown as the black curve in Fig. 5.1b. We emphasize that this procedure is very robust with respect to the size of the optimization interval; namely, we obtain the same values of $A, B, C,$ when the interval is enlarged to contain up to three oscillations.

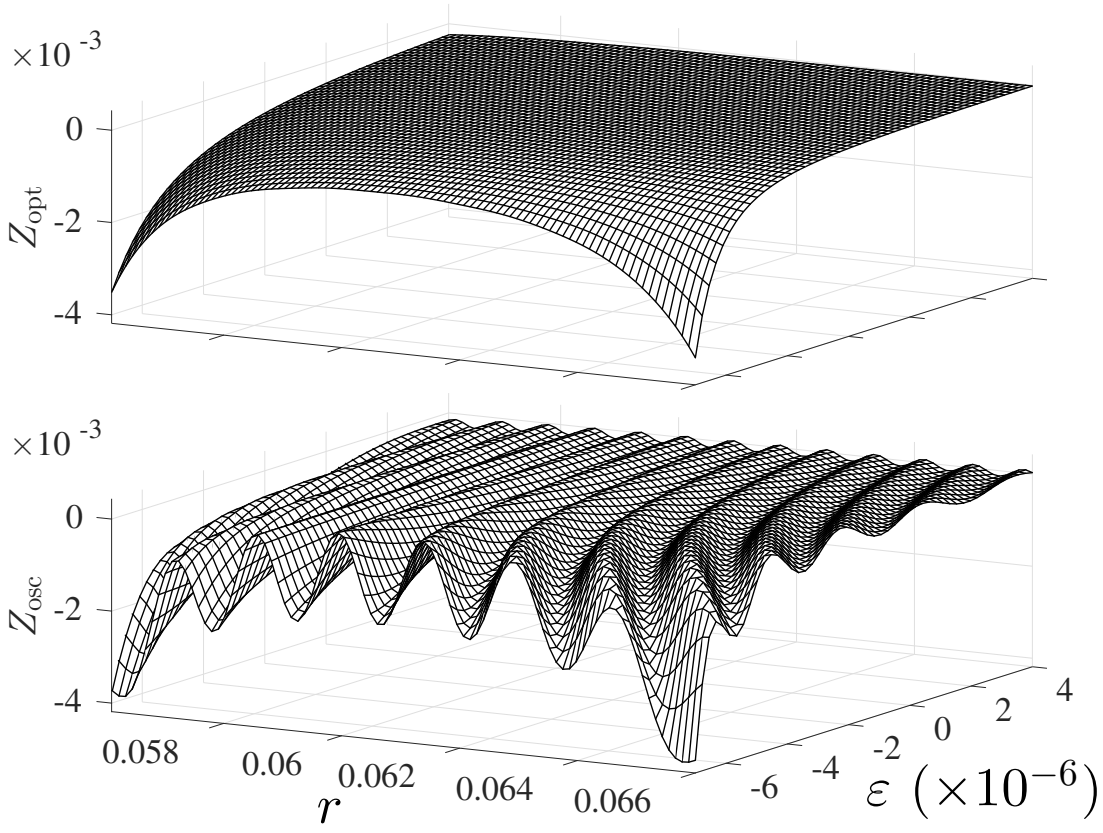

Figure 5.2. $Z(\varepsilon, R)$ using optimization (upper) and using the WKB-initialization (lower). See text for details. The range of the surface plot corresponds to the rectangle in Fig. 5.1(a).

Fig. 5.2 compares our optimization procedure with the standard WKB-initialized scheme [77], which relies on using the WKB approximation to impose the initial condition for ρ at the bottom of the potential ($R_0 \approx 0.05856$). We use Eq. (4.5) to compute both the optimal envelope, $\rho_{\rm opt}(R)$, and WKB-initialized envelope denoted as $\rho_{\rm osc}(R)$ for a range of energies corresponding to $-7\times10^6 < \varepsilon < 4\times10^6$. For clarity, we make use of the WKB approximation $\rho_{\rm wkb}(R) \equiv q|U(R)|^{-1/2}$ to rescale both $\rho_{\rm opt}(R)$ and $\rho_{\rm osc}(R)$. Thus, we define $Z_{\rm opt}$ and $Z_{\rm osc}$ according to $Z(\varepsilon, R) = \frac{\rho(R)}{\rho_{\rm wkb}(R)} - 1$, and plot them in Fig. 5.2. Note the oscillatory behavior of $Z_{\rm osc}$, while $Z_{\rm opt}$ obtained using our $\rho_{\rm opt}(R)$ is smooth.

The optimization method described above is applicable for all clasically allowed regions, and it provides a smooth envelope which can be propagated efficiently by solving Eq. (4.5). Note that when the propagation enters a classically forbidden region, the envelope will take on an increasing behavior, e.g., for $\varepsilon = -\kappa^2 < 0$ and $R \to \infty$, $y(R) \sim e^{\kappa R}$. Thus, the solution $\psi = y(R)\sin\theta(R)$, with $\theta(R) = q\int_0^R \frac{d\tau}{\rho(\tau)}$, will diverge when $R \to \infty$, unless $\theta(\infty)$ is an integer number of π, in which case, $\sin\theta(R) \sim e^{-2\kappa R}$ guarantees that ψ has the correct behavior of an eigenfunction corresponding to a bound state.

5.3 Quantum Reflection and Wavefunction Matching

When two classically allowed regions are separated by a classically forbidden region due to a barrier, it is well known [85] that a global envelope which is smooth in all regions cannot exist. In fact, this lack of global smoothness can also manifest within a single classically allowed region. Indeed, when the asymptotically optimized envelope is propagated inwards, it may develop oscillations at short range, as shown in Fig. 5.3(a). Conversely, if the envelope is first optimized at short range, it may develop oscillations when propagated outwards into the asymptotic region, see Fig. 5.3(b). This type of oscillatory behavior is directly related to quantum reflection[114, 115, 116, 117, 118, 119], which is very pronounced at low energy, but diminishes and eventually disappears at high energy. The results shown in Figs. 5.3(a) and (b) correspond to $\ell = 0$ and $V(R) = -\frac{1}{R^n}$ with $n = 1, 3, 4, 6$. Note that the oscillations are more pronounced for high n, due to the more abrupt behavior of $V(R)$, while $n = 1$ (Coulomb) is a special case which admits a globally smooth envelope for all energies.

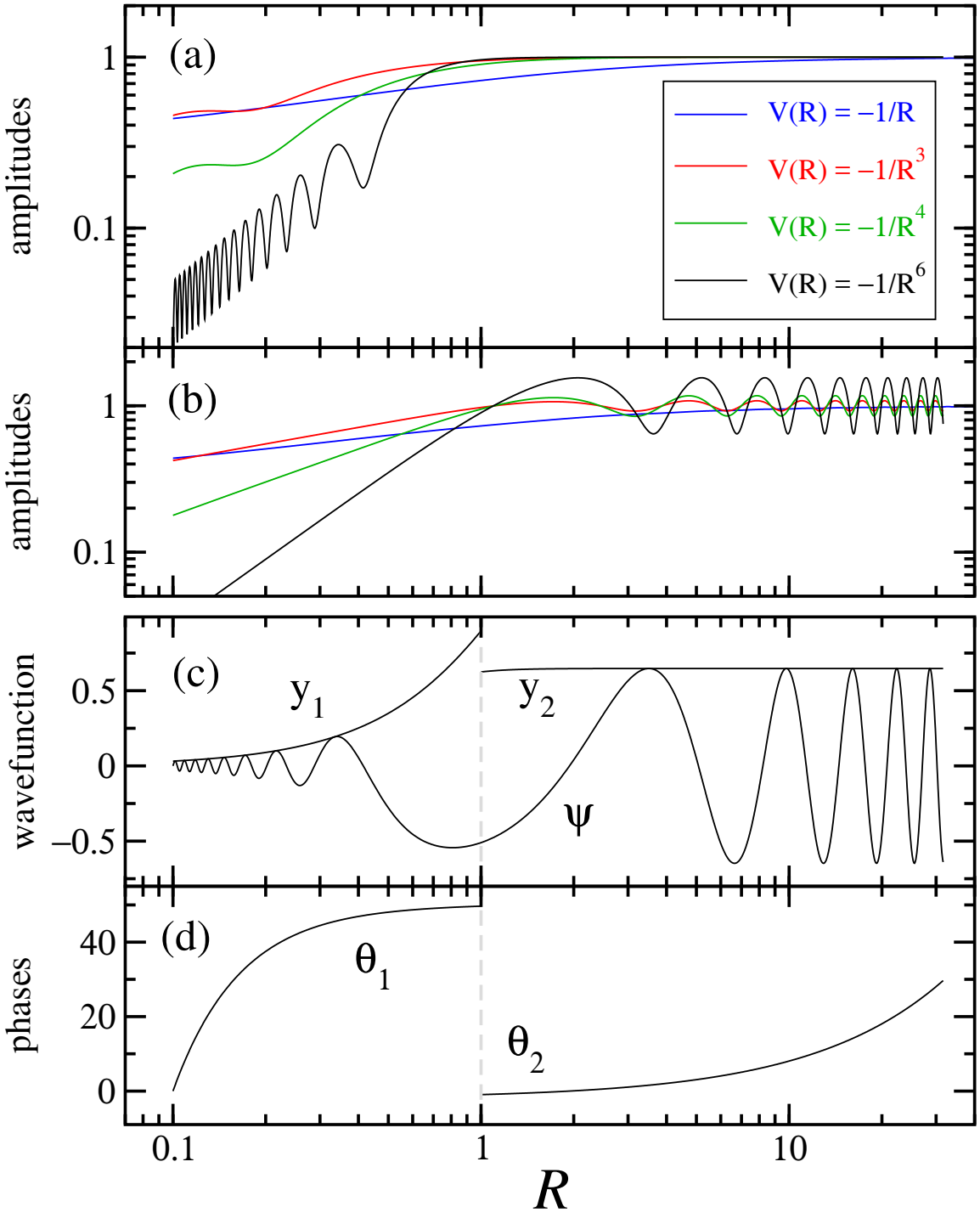

Figure 5.3. (a) Asymptotically optimized amplitudes for $\varepsilon = 1$ and $V(R) = -1/R^n$, with $n = 1, 3, 4, 6$. (b) Amplitudes optimized at short range for the same cases. (c) Regular solution $\psi = y_1 \sin\theta_1 = y_2 \sin\theta_2$ for $V(R) = -1/R^6$. (d) Phases $\theta_{1,2}$ corresponding to amplitudes $y_{1,2}$. See text for details.

In the absence of a globally smooth envelope, a simple partitioning scheme can be used to take advantage of regionally smooth phases and envelopes. To illustrate such an approach, we use $V(R) = -1/R^6$ with $\ell = 0$ and $\varepsilon = 1$. In the first region ($R \leq 1$) we employ the short range optimization to obtain $\psi = y_1 \sin\theta_1$, with $\theta_1 = 0$ at $R_0 = 0.1$, where we placed a hard wall. In the asymptotic region ($R \geq 1$) we construct the solution $\psi = y_2 \sin\theta_2$ with $y_2 = cy_\infty$ and $\theta_2 = \theta_\infty + \delta$. Matching for ψ and ψ' is imposed at $R = 1$ to determine c and δ. The amplitudes $y_1(R)$ and $y_2(R)$ are shown in Fig. 5.3c and the phases $\theta_1(R)$ and $\theta_2(R)$ are shown in Fig. 5.3d. Note that $\theta_1' \neq \theta_2'$ and $\theta_1 \neq \theta_2 \pmod{\pi}$ at $R = 1$. Thus, despite quantum reflection, any wavefunction $\psi(R)$ can still be parametrized economically by judiciously partitioning the R domain and computing separately a smooth envelope and the corresponding phase for each region.

Finally, we impose the matching conditions at the boundary $R = 1$ between the two regions,

$$\begin{aligned} y_1 \sin\theta_1 &= c\, y_{\text{asy}} \sin(\theta_{\text{asy}} + \delta), \\ \frac{d}{dR}\big[y_1 \sin\theta_1\big] &= c\, \frac{d}{dR}\big[y_{\text{asy}} \sin(\theta_{\text{asy}} + \delta)\big], \end{aligned}$$

and we extract the phaseshift δ and the constant c.

5.4 PhaseAmplitude Formalism for Ultra-Narrow Shape Resonances

Matching the two sets of phases and amplitudes, y_1, θ_1 and y_{asy} θ_{asy}, allows us to extract phase shift δ as shown in Sec. 5.3, but the phase shift is of modular π and we lose the advantage of obtaining the true phase shift as in Chapter. 4. In this section, we present a scheme to directly match the envelope and phase functions. We

will see that this approach also allows us to extract the width of ultra-narrow shape resonances.

5.4.1 Matching equations

As an illustrative example, we consider again the potential energy employed in the last Chapter 4,

$$V(R) = C_{\rm wall} \exp\left(-\frac{R}{R_{\rm wall}}\right) - \frac{C_3}{R^3 + R_{\rm core}^3}, \tag{5.4}$$

with $C_{\rm wall} = 10$, $R_{\rm wall} = 1$, $R_{\rm core} = 5$ and $C_3 = 18$ (all in atomic units), and the reduced mass $\mu = \frac{m}{2}$, where m is the mass of ^{88}Sr. The effective potential, $V_{\rm eff} = V + \frac{\ell(\ell+1)}{2\mu R^2}$, has a centrifugal barrier if $0 < \ell \lessapprox 557$, as shown in Fig. 5.4. Hence, there is a regime of scattering energies ($E > 0$) for which there are two classically allowed regions separated by the barrier. The potential well at short range may hold resonances (and also bound states, if deep enough). As is well known, a deep potential well delimited by a large barrier allows for shape resonances which can be extremely narrow. Although various methods have been developed for tackling this problem [120, 121, 122], it is still surprisingly difficult to obtain accurate values for resonance widths which are vanishingly small. We now present a phase-amplitude formalism adapted for large barriers, which will prove suitable for ultra-narrow resonances.

As depicted in Fig. 5.4, the radial domain is divided in two regions; the inner region is defined as $0 < R < R_{\rm m}$, where $R_{\rm m}(E)$ is the turning point on the inner side of the barrier, while the outer region ($R_{\rm m} < R < \infty$) includes the barrier and the entire asymptotic region. The envelope ρ employed in the outer region is obtained by solving the envelope Eq. (4.5) together with the asymptotic boundary condition

$$\rho(R) \xrightarrow{R\to\infty} 1.$$

As discussed in Ref. [123], the asymptotic normalization of ρ to unity corresponds to $q = k$. The phase $\theta(R)$ is found by integrating Eq. (4.4) which now reads

$$\theta' = \frac{k}{\rho}. \tag{5.5}$$

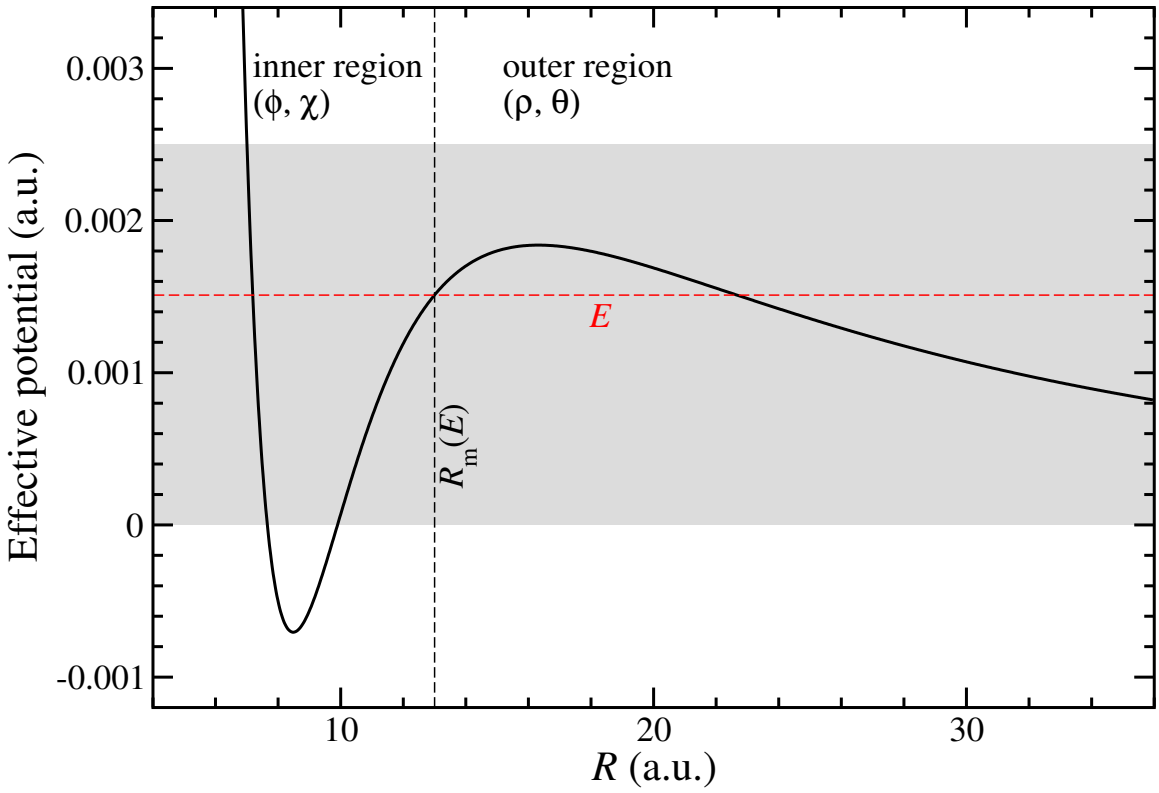

Figure 5.4. The effective potential $V_{\text{eff}}(R) = V(R) + \frac{\ell(\ell+1)}{2\mu R^2}$ with $V(R)$ given in Eq. (5.4) and $\ell = 500$. The vertical span of the shaded area represents the energy range explored in our study.

The numerical approach for computing $\rho(R)$ and $\theta(R)$ was described in our previous work [123], where it was shown that the arbitrary additive constant implicit in the integration of the phase can be adjusted to ensure the asymptotic behavior

$\theta(R) \sim kR$. In Ref. [123] we used Milne's parametrization for the physical solution of the radial equation,

$$\psi(R) = \sqrt{\rho(R)}\sin[\theta(R) - \theta(0)], \tag{5.6}$$

to obtain the scattering phase shift,

$$\delta_\ell = \ell\tfrac{\pi}{2} - \theta(0), \tag{5.7}$$

which is usually extracted from the well known asymptotic behavior of the wave function, $\psi(R) \sim \sin(kR - \ell\frac{\pi}{2} + \delta_\ell)$.

The smooth envelope and phase are initialized at $R = \infty$ and are propagated inward through the asymptotic region and through the barrier, but not into the inner region. Indeed, if the envelope is propagated to $R < R_{\rm m}$, it no longer remains smooth; instead, $\rho(R)$ behaves in a highly oscillatory fashion in the *inner* well, and consequently the phase $\theta(R)$ follows a staircase behavior with very sharp features which cannot be handled numerically. Thus, we need to develope a different approach for the inner region.

Inside the inner region ($0 < R < R_{\rm m}$) we consider two linear independent solutions ($\phi,\ \chi$) of the radial Eq. (4.1). One of them (ϕ) is chosen as the regular solution, i.e., we need to ensure $\phi(R) \to 0$ when $R \to 0$. We also need to ensure that both ϕ and χ have a well defined energy dependence. Making use of Eq. (5.1), we now express the *outer* envlope ρ as a linear combination of ϕ^2, χ^2 and $\phi\chi$,

$$a\,\phi^2(R) + b\,\chi^2(R) + 2c\,\phi(R)\chi(R) = \rho(R). \tag{5.8}$$

The coefficients a, b and c will be obtained from the following matching conditions which are imposed at $R = R_{\rm m}$,

$$\begin{aligned} a\phi^2 + b\chi^2 + 2c\phi\chi &= \rho \\ a\phi\phi' + b\chi\chi' + c\big(\phi\chi' + \phi'\chi\big) &= \tfrac{1}{2}\rho' \\ a\big(\phi'\big)^2 + b\big(\chi'\big)^2 + 2c\phi'\chi' &= \tfrac{1}{2}\rho'' - \rho U. \end{aligned} \tag{5.9}$$

We remark that Eq. (5.8) is valid for all R, and thus the vaules of a, b, c are independent of the matching point $R_{\rm m}$, which in principle could be located anywhere. However, in practice, $R_{\rm m}$ should be very close to the turning point on the inner side of the barrier. Indeed, as mentioned above, the outer phase θ cannot be propagated in the inner well. Conversely, ϕ and χ should not be propagated outside the inner well, because they would increase through the barrier and would become linearly dependent. The most convenient choice for the matching point $R_{\rm m}$ is clearly the turning point itself, as shown in Fig. 5.4.

5.4.2 Explicit solution of the matching equations

The 3×3 linear system of equations (5.9) can be solved in an elementary way; first, its determinant Δ can be expressed in closed form, $\Delta = W^3 \neq 0$, where W is the (nonvanishing) Wronskian of ϕ and χ, and then the coefficients a, b and c are obtained as the unique solution,

$$\begin{aligned} a &= \frac{\rho}{W^2}\left(\chi' - \frac{\rho'}{2\rho}\chi\right)^2 + \frac{k^2\chi^2}{W^2\rho} \\ b &= \frac{\rho}{W^2}\left(\phi' - \frac{\rho'}{2\rho}\phi\right)^2 + \frac{k^2\phi^2}{W^2\rho} \\ c &= -\frac{\rho}{W^2}\left(\phi' - \frac{\rho'}{2\rho}\phi\right)\left(\chi' - \frac{\rho'}{2\rho}\chi\right) - \frac{k^2\phi\chi}{W^2\rho}. \end{aligned} \tag{5.10}$$

Using the expressions above one can verify that a, b, c do indeed obey the constraint

$$ab - c^2 = \frac{k^2}{W^2}. \tag{5.11}$$

Due to this constraint, which was employed in evaluating the integrals in the previous section, only the coefficients a and c appear in Eq. (5.18), while b does not. However, we shall see that b is directly related to the Jost function, while c yields the widths of the shape resonances trapped by the barrier.

Before we begin to develop our extended phase-amplitude formalism, we remark that the explicit solution (5.10) of the matching equations (5.9) allows us to anticipate certain results. Indeed, except for the case of a broad resonance near the top of the barrier, the analysis is greatly simplified for all narrow resonances which are located far below the top of the barrier. First, we recall that ϕ, χ and ρ in Eq. (5.10) are evaluated at the matching (turning) point $R_{\rm m}$. The value of $\rho(R_{\rm m})$ is extremely large due to the propgation through the barrier, and we thus have $\rho \ggg \frac{1}{\rho}$. Therefore, we can safely neglect the last term in Eq. (5.10), which simplifies the expresions of a, b and c. In particular, it becomes clear that the coefficient $b(E)$ will (nearly) vanish if

$$\frac{\phi'}{\phi} = \frac{\rho'}{2\rho} \qquad (\text{at } R = R_{\rm m}),$$

which can be regarded as the resonance condition ($E = E_{\rm res}$). Indeed, according to Eq. (5.10), $c(E)$ will also vanish when $b(E)$ vanishes, and Eq. (5.8) will reduce to

$$a\phi^2(R) = \rho(R), \qquad \text{when } E = E_{\rm res},$$

which holds not only inside the inner region, but also through most of the barrier. The behavior of the envelope in the classically forbidden region ensures an exponential

decreasing tail for the regular solution ϕ through the barrier, as expected for a quasi-bound state, which justifies the resonance condition above.

5.4.3 Extending Milne's phase outside its domain of smoothness

Making use of Eq. (5.8), we now extend the outer phase $\theta(R)$ to $R < R_{\rm m}$ by integrating Eq. (5.5). We emphasize that we do so formally rather than numerically,

$$\theta(R_{\rm m}) - \theta(R) = k\int_R^{R_{\rm m}} \frac{dr}{\rho(r)}, \tag{5.12}$$

$$= k\int_R^{R_{\rm m}} dr\big[a\phi^2 + b\chi^2 + 2c\phi\chi\big]^{-1}. \tag{5.13}$$

Taking advantage of $dW/dR = 0$, where W is the Wronskian of χ and ϕ, we rewrite the integral above,

$$\theta(R_{\rm m}) - \theta(R) = \frac{k}{W}\int_R^{R_{\rm m}} dr \frac{\phi'\chi - \phi\chi'}{a\phi^2 + b\chi^2 + 2c\phi\chi}, \tag{5.14}$$

with $W = \phi'\chi - \phi\chi' \neq 0$. Next, we define a new variable,

$$z(r) = \frac{\phi(r)}{\chi(r)}, \tag{5.15}$$

and we recast the integrand in Eq. (5.14) as

$$\frac{\phi'\chi - \phi\chi'}{a\phi^2 + b\chi^2 + 2c\phi\chi} = \frac{1}{az^2 + b + 2cz}\,\frac{dz}{dr}.$$

Without loss of generality, we assume that both $\phi(R)$ and $\chi(R)$ are positive when $R \to 0$, which ensures $W > 0$ and thus $dz/dr = W\chi^2$ is always positive. We now change the integration variable in Eq. (5.14) from r to z, but we do so only after we partition the inner region in sub-intervals delimited by the nodes of χ, such that $z(r)$ is a one-to-one mapping inside each interval.

Recall that we are especially interested in evaluating the outer phase at $R = 0$. Thus, setting $R = 0$ in Eq. (5.14), we have

$$\theta(R_{\rm m}) - \theta(0) = k \sum_{j=0}^{N_{\rm m}} \int_{R_j}^{R_{j+1}} \frac{dr}{\rho(r)}, \tag{5.16}$$

$$= \frac{k}{W} \left[\int_0^{\infty} \frac{dz}{az^2+2cz+b} + (N_{\rm m} - 1) \int_{-\infty}^{+\infty} \frac{dz}{az^2+2cz+b} + \int_{-\infty}^{z_{\rm m}} \frac{dz}{az^2+2cz+b} \right], \tag{5.17}$$

where $z_{\rm m}$ is the upper limit of the last integral,

$$z_{\rm m} = \frac{\phi(R_{\rm m})}{\chi(R_{\rm m})}.$$

In Eq. (5.16), $R_0 = 0$ and $R_{N_{\rm m}+1} = R_{\rm m}$ are the boundaries of the inner region, while $R_1, R_2, \ldots, R_{N_{\rm m}}$ are the nodes of $\chi(R)$ inside the inner region. Except for the first and last interval, all other $(N_{\rm m} - 1)$ intervals give identical contributions, as is made clear by the new integration variable z in Eq. (5.17).

Making use of the constraint $(ab - c^2)W^2 = k^2$, the integral appearing repeatedly in Eq. (5.17) takes a simple form,

$$\frac{k}{W} \int \frac{dz}{az^2 + 2cz + b} = \arctan \left[\frac{W}{k} (az + c) \right],$$

which we now evaluate for each interval. The contribution of the first interval is

$$k \int_0^{R_1} \frac{dr}{\rho(r)} = \frac{k}{W} \int_0^{\infty} \frac{dz}{az^2 + b + 2cz} = \frac{\pi}{2} - \arctan \left(\frac{cW}{k} \right),$$

while the last interval yields

$$\begin{aligned} k \int_{R_{N_{\rm m}}}^{R_{\rm m}} \frac{dr}{\rho(r)} &= \frac{k}{W} \int_{-\infty}^{z_{\rm m}} \frac{dz}{az^2 + b + 2cz}, \\ &= \arctan \left[\frac{W}{k} (c + az_{\rm m}) \right] + \frac{\pi}{2}. \end{aligned}$$

As mentioned above, the $(N_{\rm m}-1)$ remaining intervals give identical contributions; namely, for $1 \leq j \leq N_{\rm m}-1$, we have

$$k\int_{R_j}^{R_{j+1}} \frac{dr}{\rho(r)} = \frac{k}{W}\int_{-\infty}^{+\infty} \frac{dz}{az^2+b+2cz} = \pi.$$

We now add the contributions from all intervals to obtain

$$\theta_{\rm m} - \theta(0) = N_{\rm m}\pi - \arctan\left(\frac{cW}{k}\right) + \arctan\left[\frac{W}{k}(c+az_{\rm m})\right], \tag{5.18}$$

where $\theta_{\rm m} = \theta(R_{\rm m})$. The result above remains valid when $N_{\rm m} = 0$. Indeed, if $\chi(R)$ has no zeros inside the inner region, the partitioning is no longer needed; thus, Eq. (5.17) reduces to

$$\begin{aligned} \theta_{\rm m} - \theta(0) &= \frac{k}{W}\int_0^{z_{\rm m}} \frac{dz}{az^2+b+2cz} && (5.19)\\ &= \arctan\left[\frac{W}{k}(c+az_{\rm m})\right] - \arctan\left(\frac{cW}{k}\right), && (5.20) \end{aligned}$$

which is identical to Eq. (5.18) when $N_{\rm m} = 0$. Finally, we remark that the integrals above were evaluated assuming $a > 0$, which is justified as follows; we recall that Eq. (5.8) is valid for all R. In particular, when $\chi(R)$ vanishes, Eq. (5.8) yields $\rho = a\phi^2$; hence, $\rho > 0$ implies $a > 0$.

5.4.4 Locally adapted solutions

Although ϕ and χ can be obtained as numerical solutions of the radial equation, we prefer instead to employ the phase-amplitude method in the inner region, as well as in the outer region. This will allow us to express the coefficients a, b, c in terms of an inner region phase; the latter has a smooth energy dependence, which we ensure with a simple optimization procedure as described in Sec. 5.2.

Let $\rho_{\rm in}$ denote the optimized (i.e., smooth) envelope in the innner region, and β the corresponding phase function,

$$\beta(R) \equiv q \int_0^R \frac{dr}{\rho_{\rm in}(r)}, \tag{5.21}$$

where q is the parameter used in obtaining the inner envelope. We now use $\rho_{\rm in}$ and β to construct ϕ and χ,

$$\begin{aligned} \phi &= \sqrt{\rho_{\rm in}}\sin\beta, \\ \chi &= \sqrt{\rho_{\rm in}}\cos\beta. \end{aligned} \tag{5.22}$$

Eq. (5.21) ensures $\beta = 0$ at $R = 0$; thus, ϕ is regular, as desired. The expressions above yield $W = \phi'\chi - \phi\chi' = q$, and the coefficients in Eq. (5.10) now read

$$\begin{aligned} \bar{a} &= (1+u^2)\cos^2(\beta+\Delta) + \epsilon^2\cos^2\beta, \\ \bar{b} &= (1+u^2)\sin^2(\beta+\Delta) + \epsilon^2\sin^2\beta, \\ \bar{c} &= -(1+u^2)\sin(\beta+\Delta)\cos(\beta+\Delta) - \epsilon^2\sin\beta\cos\beta, \end{aligned} \tag{5.23}$$

with β evaluated at the matching point $R_{\rm m}$. Note that we have rescaled the coefficients according to

$$a = \bar{a}\frac{\rho(R_{\rm m})}{\rho_{\rm in}(R_{\rm m})}, \tag{5.24}$$

and similar for b and c. The additional parameters in Eq. (5.23) read

$$u = \frac{1}{2q}\left(\rho'_{\rm in} - \rho_{\rm in}\frac{\rho'}{\rho}\right), \qquad \cot\Delta = u, \qquad \epsilon = \frac{k\rho_{\rm in}}{q\rho},$$

with $\rho_{\rm in}$ and ρ evaluated at $R_{\rm m}$. We remark that the scaled coefficients $(\bar{a},\ \bar{b},\ \bar{c})$ do depend on the location of $R_{\rm m}$, even though the unscaled coefficients (a, b, c) do not. Therefore, in order to ensure that the quantities introduced above have a well defined energy behavior, the matching point itself should have a well defined energy dependence, which is ensured by imposing the matching conditions at the turning point $R_{\rm m}(E)$, as discussed in Sec. 5.4.3; see also Fig. 5.4.

We emphasize that the rescaling (5.24) is only necesary in the case of a large barrier, and only for energies deep below the top of the barrier, when the outer envelope itself has to be rescaled during its inward propagation, in order to avoid numerical overflow due to its quasi-exponential behavior through the barrier. Finally, we remark that in Eq. (5.23) all quantities $(u, \Delta, \beta, \epsilon)$ are independent of the choice of q, and so are the scaled coefficients. Since the parameter q can be chosen freely, we shall use $q = k$, which yields $W = k$ and thus simplifies Eq. (5.18),

$$\theta_{\rm m} - \theta(0) = N_{\rm m}\pi - \arctan(c) + \arctan(c + a z_{\rm m}). \tag{5.25}$$

The scattering phase shift is obtained from Eqs. (5.7) and (5.25),

$$\delta_\ell = \ell\frac{\pi}{2} - \theta_{\rm m} + N_{\rm m}\pi + \arctan\left(c + a\, z_{\rm m}\right) - \arctan(c). \tag{5.26}$$

According to the definitions (5.15) and (5.22), $z_{\rm m} = \tan\beta(R_{\rm m})$. Moreover, it can be easily verified that the number of nodes of $\chi(R)$ in the inner region is $N_{\rm m} = {\rm nint}[\beta(R_{\rm m})/\pi]$, where ${\rm nint}[\cdots]$ stands for nearest integer. Thus, the expression above contains only quantities derived from the phase-amplitude formalism.

5.4.5 Results and discussion

We now present results for the potential energy given in Eq. (5.4), which is used as an illustrative example for discussing the physical interpretation of the formalism

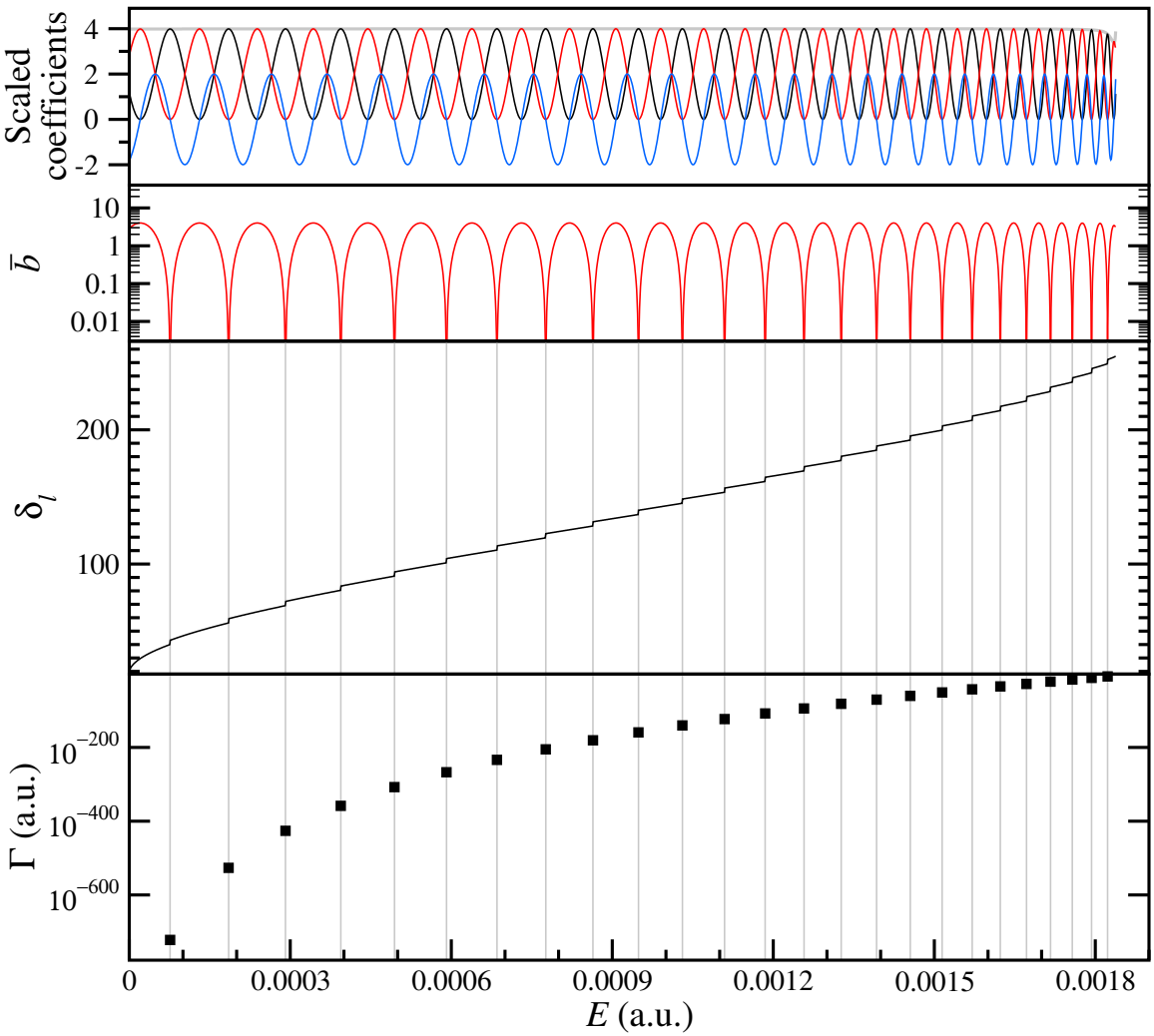

Figure 5.5. Scaled coefficients (top), $\bar{b}(E)$, $\delta_\ell(E)$, $\Gamma_{\rm res}$ vs. Energy.

presented above. We are especially interested in the case of a large barrier, which allows for long lived resonances. Thus, we employ a sufficiently high value for ℓ, such that the effective potential has a very large centrifugal barrier; at the same time, ℓ is low enough for $V_{\rm eff}$ to have a potential well at short range capable of holding shape resonances; see Fig. 5.4. We choose $\ell = 500$, and we analyze in detail the energy dependence for $\delta_\ell(E)$ and for the quantities introduced in Sec. 5.4.4.

Fig. 5.5 shows the energy dependence of the scaled coefficients; their simple oscillatory behavior stems from the fact that the optimized phase $\beta(R_{\rm m}; E)$ in Eq. (5.23) has a smooth energy dependence (see Fig. 5.6). Moreover, the parameter $u(E)$ is nearly constant, as shown by the nearly flat thick gray line in Fig. 5.5, indicating the oscillation amplitude $(1 + u^2)$ of the scaled coefficients. Recall that the ϵ^2 terms in Eq. (5.23) are negligible (except near the top of the barrier), while $\Delta(E)$ is almost constant. The phase shift $\delta_\ell(E)$ is also shown in Fig. 5.5, with its well known sharp increase by π for each resonance clearly visible; vertical lines mark the positions of all resonances under the barrier, and the values of their widths Γ are plotted. A semilog plot of the scaled coefficient $\bar{b}(E)$ is included in Fig. 5.5, to indicate that its (nearly vanishing) minima signify resonances. We acknowledge that the locations of ultra-narrow resonances can simply be obtained using any method that is suitable for finding bound states. However, obtaining the vanishingly small widths of such resonances is a difficult task, and the approach presented in this chapter yields a convenient solution, as we show next.

For scattering energies deep below the top of the barrier, the inner region becomes inaccessible (unless $E \approx E_{\rm res}$). Thus, for $E \not\approx E_{\rm res}$ the outer region determines the scattering phase shift; indeed, in Eq. (5.26) we identify the background contribution,

$$\delta_\ell^{\rm bg}(E) = \ell\frac{\pi}{2} - \theta_{\rm m}(E), \tag{5.27}$$

which is entirely given by the outer phase θ, and as we show next, we have $\delta_\ell^{\rm bg} \approx \delta$ mod π (for $E \not\approx E_{\rm res}$). The remaining terms in Eq. (5.26) give the contribution of the inner region, which can be interpreted as the resonant part,

$$\begin{aligned} \delta_\ell^{\rm res}(E) &= \arctan[-c(E)] \\ &+ \arctan[c(E)+a(E)z_{\rm m}(E)] + \pi N_{\rm m}(E). \end{aligned} \tag{5.28}$$

Note that $\delta_\ell^{\rm res}(E)$ is continuous; indeed, each $(+\pi)$ jump stemming from $\pi N_{\rm m}(E) = {\rm nint}[\beta_{\rm m}(E)]$ at $\beta_{\rm m} \bmod \pi = \frac{\pi}{2}$ is cancelled by a $(-\pi)$ jump given by $\arctan[c(E) + a(E)z_{\rm m}(E)]$ when $z_{\rm m} = \tan\beta_{\rm m}$ jumps from $+\infty$ to $-\infty$.

Fig. 5.7 shows that $\delta^{\rm res}(E)$ follows a stepwise behavior, effectively counting the resonances trapped by the large centrifugal barrier in our example. Indeed, Eq. (5.28) yields a constant value (an integer multiple of π) for $\delta^{\rm res}(E)$ between resonances, and a very abrupt (albeit continuous) increase by π for each resonance, which is the well known signature of a resonance.

As shown in Fig. 5.5, the resonances are located at the minima of $b(E)$, where $c(E)$ also vanishes. Note that $c(E)$ *decreases* at resonance from large positive values to large negative values; hence, $\delta^{\rm res} \pmod\pi$ will increase sharply from 0 to π, when E increases across $E = E_{\rm res}$.

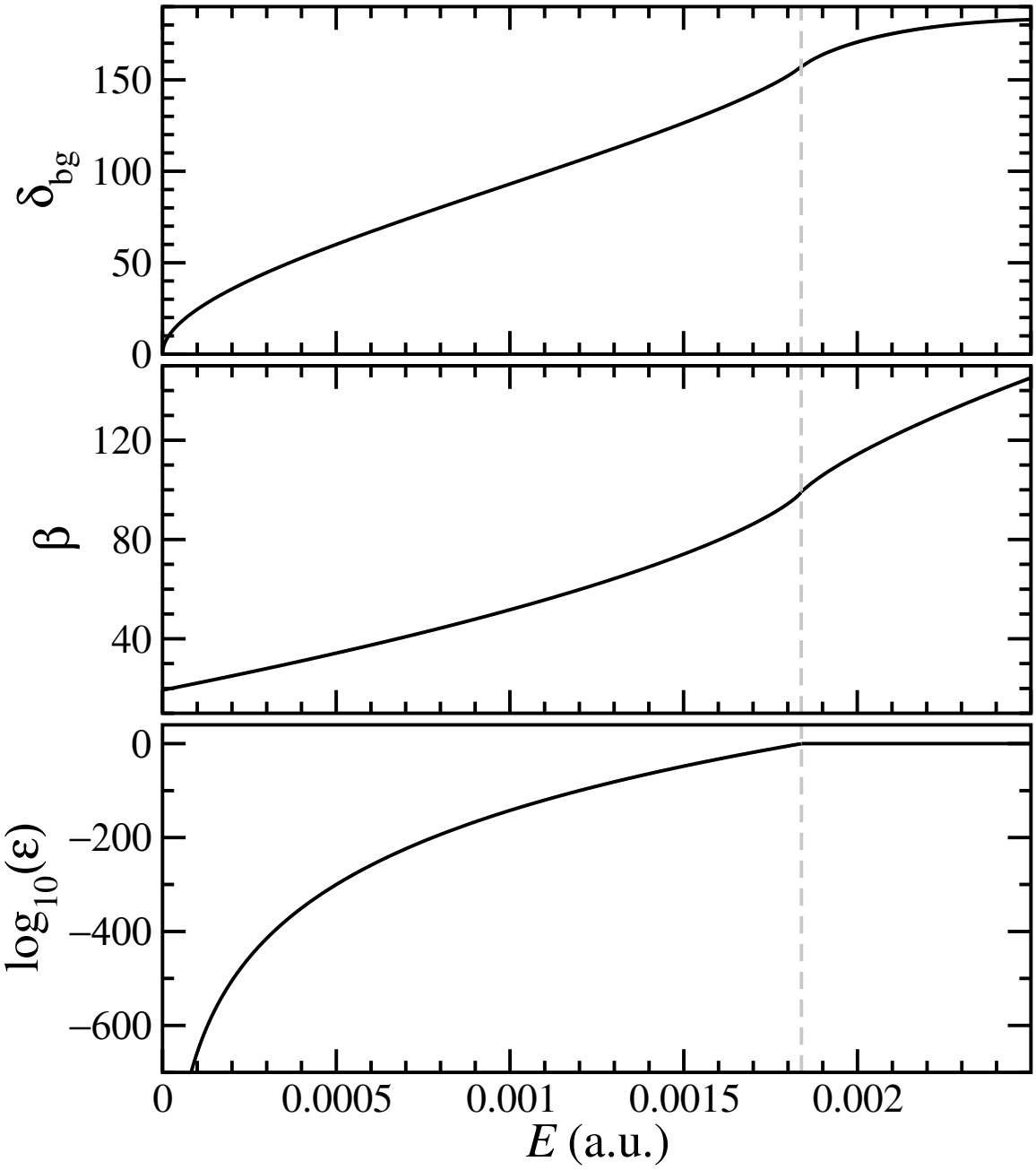

Figure 5.6. Energy dependence of the background phase shift $\delta_{\rm bg}(E)$ (upper), the inner region phase $\beta(R_{\rm m}; E)$ (middle), and the scaling parameter $\epsilon(E)$ (lower). The vertical dashed line marks the top of the barrier.

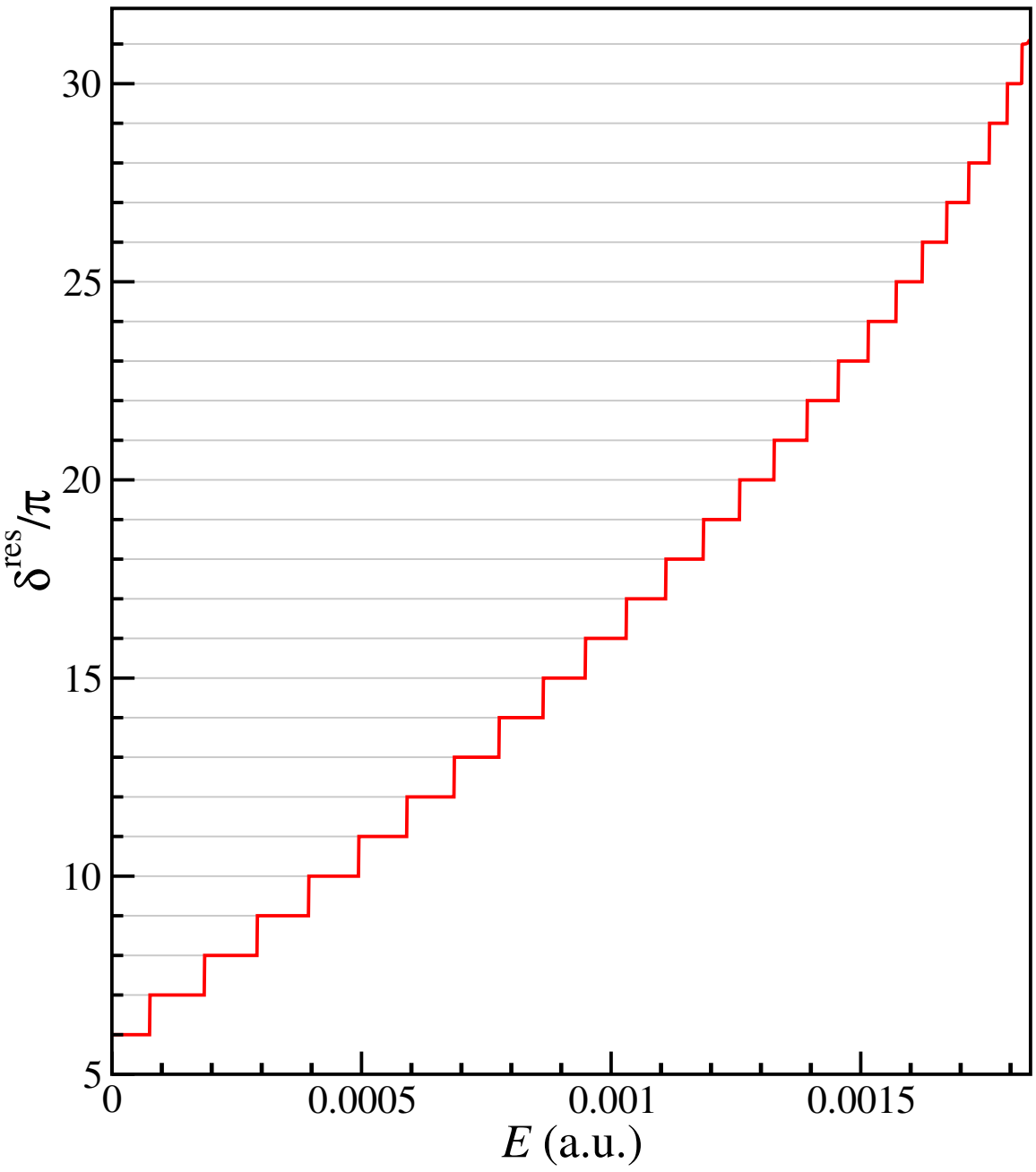

Figure 5.7. Resonant contribution (from the inner region).

The width of the resonance, or rather the lifetime $\tau = 1/\Gamma$ is obtained from the derivative of the phase shift, $\frac{1}{2}\frac{d\delta_\ell}{dE}$ evaluated at $E = E_{\rm res}$. From Eq. (5.28) we have

$$\frac{d\delta_\ell}{dE} \;=\; \dot{\delta}_\ell \;\approx\; -\frac{\dot{c}}{1+c^2}, \tag{5.29}$$

which allows us to extract the width of the resonance,

$$\Gamma = -2\left(\frac{dc}{dE}\right)^{-1}_{E_{\rm res}} = \frac{2}{|\dot{c}_{\rm res}|} \approx \frac{2\epsilon}{|\dot{\bar{c}}|}. \tag{5.30}$$

The vanishingly small values of Γ are due to the exceedingly small values of ϵ. We emphasize that both ϵ and $\dot{\bar{c}}_{\rm res} \equiv \dot{\bar{c}}(E_{\rm res})$ can be computed highly accurately, yielding numerically exact values for Γ.

5.4.6 Numerical test

Due to the constraint (5.11), which was employed in evaluating the integrals in Sec. 5.4.3, only the coefficients a and c appear in Eq. (5.18), while b does not; however, b is directly related to the Jost function. We first recall that ϕ in Eq. (5.22) is the regular solution and it has the asymptotic behavior

$$\phi(r) \;\xrightarrow{r\to\infty}\; A\sin\left(kr-\ell\tfrac{\pi}{2}\right) + B\cos\left(kr-\ell\tfrac{\pi}{2}\right),$$

with $B/A = \tan\delta_\ell$ and $A - iB = \mathcal{J}$ the Jost function. The physical solution normalized to unit amplitude asymptotically, i.e., $\psi(r) \sim \sin\left(kr - \ell\frac{\pi}{2} + \delta_\ell\right)$, is expressed in terms of the regular solution and the Jost function [2, 1],

$$\psi = \frac{\phi}{\mathcal{J}}.$$

Moreover, it can be shown that the coefficient b of the outer envelope expansion (5.8) is related to the Jost function $\mathcal{J}$,

$$b = |\mathcal{J}|^2 = A^2 + B^2.$$

The constraint (5.11) with $W = k$ yields $b = \frac{1+c^2}{a}$, and we thus have

$$\left|\psi_E(r)\right|^2 = \frac{a(E)}{1+c^2(E)}\phi_E^2(r).$$

For energies within a very narrow window ($\Delta E \sim \Gamma$) centered on $E_{\rm res}$, we employ the approximations $c(E) \approx (E - E_{\rm res})\dot{c}_{\rm res}$ and $a(E) \approx a_{\rm res}$. We also have

$$\phi_E(r) \approx \phi_{\rm res}(r) \quad \text{for } E \approx E_{\rm res},$$

which holds for r throughout the inner region and most of the barrier. Thus, for $E \approx E_{\rm res}$, the probability density inside the inner region is resonantly enhanced,

$$\begin{aligned}\left|\psi_E(r)\right|^2 &\approx \frac{a_{\rm res}}{1+\dot{c}_{\rm res}^2(E-E_{\rm res})^2}\phi_{\rm res}^2(r) \\ &= \frac{\frac{\Gamma}{2}}{\left(E-E_{\rm res}\right)^2+\left(\frac{\Gamma}{2}\right)^2}\frac{\bar{a}_{\rm res}\phi_{\rm res}^2(r)}{\left|\dot{\bar{c}}_{\rm res}\right|},\end{aligned}$$

Finally, we follow Breit and Wigner [124] and make use of

$$k_{\rm res}\int_0^{R^{\rm out}} \psi_{\rm res}^2(r)\,dr \approx 2\frac{E_{\rm res}}{\Gamma},$$

to obtain

$$\int_0^{R^{\rm out}} \phi_{\rm res}^2(r)\,dr \approx -\frac{E_{\rm res}\dot{c}_{\rm res}}{k_{\rm res}a_{\rm res}} = -\frac{E_{\rm res}\dot{\bar{c}}_{\rm res}}{k_{\rm res}\bar{a}_{\rm res}}. \tag{5.31}$$

The upper limit $R^{\rm out}$ in the integral above is the turning point on the outer side of the barrier. Eq. (5.31) is used as a numerical test in Fig. 5.8 which clearly shows that the difference of both sides of Eq. (5.31) vanishes very fast as we lower the energy further below the top of the barrier.

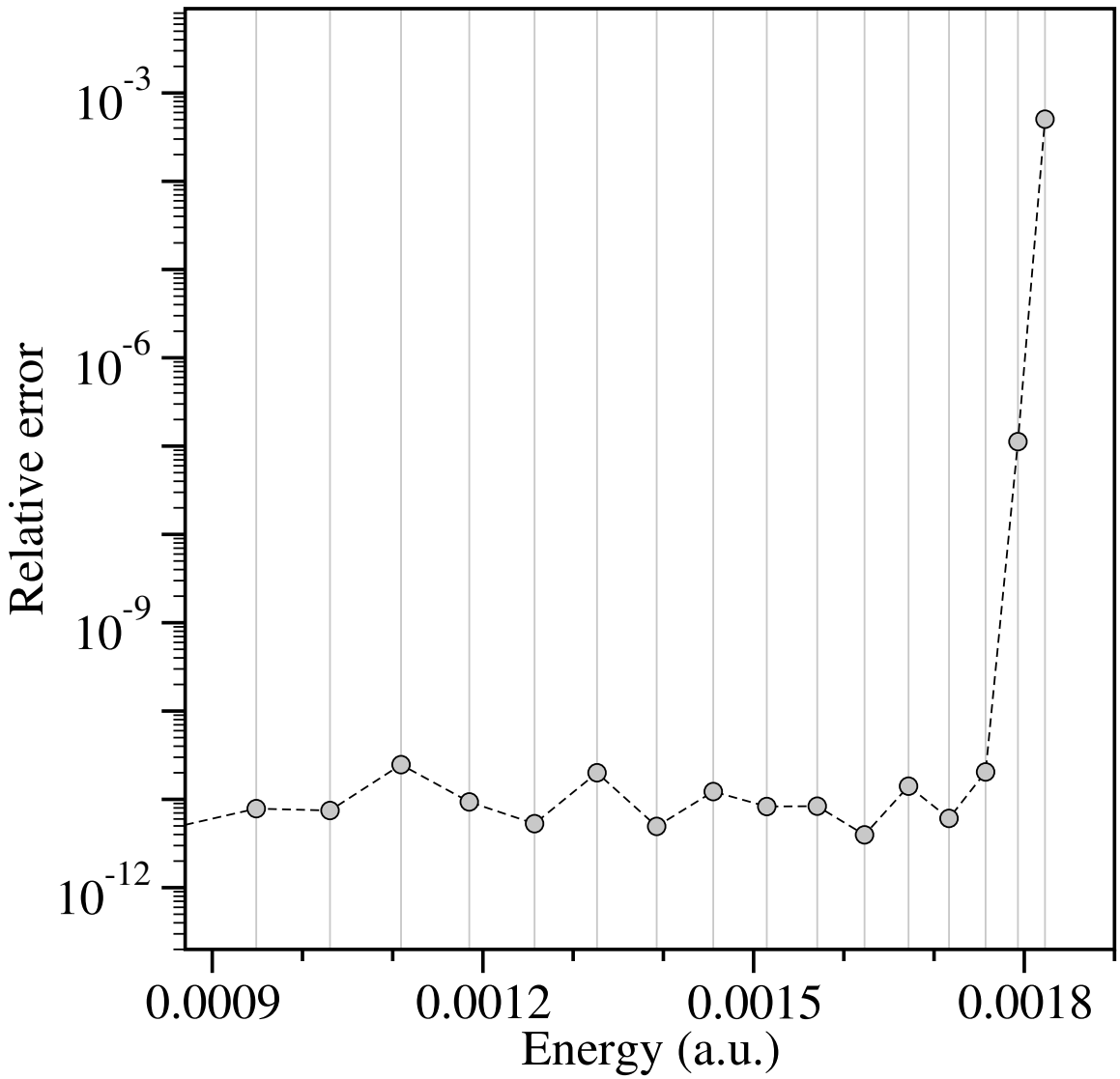

Figure 5.8. The relative error (defined as $|\mathcal{S} - \mathcal{C}|/\mathcal{S}$) for the integral $\mathcal{S} = \int \phi^2 dr$, i.e., the left-hand-side of Eq. (5.31). $\mathcal{S}$ was computed by numerical integration, while $\mathcal{C} \equiv -E_{\rm res}\dot{\bar{c}}_{\rm res}/k_{\rm res}\bar{a}_{\rm res}$ is the right-hand-side of Eq. (5.31).

Chapter 6
Conclusion and Future Direction

In this dissertation, we have studied near threshold behavior of two-body systems and three-body Efimov systems. We solved long standing problems of the phase-amplitude approach using Milne's equation, and built accurate and fast numerical tools. We expanded the phase-amplitude approach to the case when the energy is below a barrier; By matching envelop functions in different regions, we demonstrate that ultra-narrow widths of resonances can be obtained.

We showed that the Jost function is indeed a powerful tool for analyzing the energy dependence of ultra-cold scattering of two-body systems. For elastic scattering, we derived the formula for the cross section in terms of Jost functions for both finite range and long range potentials. Various energy dependence can be explained concisely with the energy dependence of Jost functions. We also verified our prediction numerically.

In multi-channel scattering problems, the Jost matrix can also be very helpful for analysis purposes. We showed that single channel Jost functions for the dominant channel gives us much information about the Jost matrix and further predict the energy dependence of the inelastic cross sections. We systematically tested our hypothesis using accurate numerical tools, and verified that our quantitative prediction is correct for many scenarios including higher partial waves.

We also explored the near threshold resonance effects in Efimov systems. By constructing Jost functions for the three-body systems, we not only successfully explained the oscillatory regions of the cross section as a function of energy at ultra-low

temperatures, we also predicted new energy regions, namely near threshold resonance and near threshold suppression regions.

The phase-amplitude approach using Milne's equation has been studied for decades and yet an effective numerical scheme has not been invented due to the difficulty of finding the non-oscillatory solution to Milne's equation. We invented a simple and effective approach for finding the optimized solution in any classically allowed region and we also created a simple, accurate and fast method to compute the asymptotic solution for the entire infinite tail of long range potentials. Stringent numerical tests show that our approach reaches nearly machine precision. We also extended the phase-amplitude approach to the case when globally smooth solution to the Milne's equation does not exist. We found a method to match the optimized non-oscillatory solutions in different regions, which not only helps us to obtain accurate cross sections efficiently, but also allows us to compute ultra-narrow resonances.

Based on this dissertation, future work will involve the following aspects. From our preliminary results, Jost functions for long range interactions can be written using phase and amplitude functions, which provide a very informative formula. We will explore how the phase-amplitude approach would deepen our understanding of Jost functions of long range interactions. Also, the methods we invented to solve the Milne's equation can be extended to solving coupled differential equations based on the distorted wave approximation, which can be used to solve multi-channel scattering problems very fast and accurately.

Bibliography

[1] J. R. Taylor, *Scattering Theory*, Dover Publications (2012).

[2] R. Newton, *Scattering Theory of Waves and Particles*, Dover Books on Physics, Dover Publications (1982).

[3] C. Joachain, *Quantum collision theory*, North-Holland (1975).

[4] N. Balakrishnan, R. Forrey, and A. Dalgarno, *Threshold phenomena in ultracold atom-molecule collisions*, Chem. Phys. Lett. **280**, 1 (1997).

[5] N. Balakrishnan, V. Kharchenko, R. Forrey, and A. Dalgarno, *Complex scattering lengths in multi-channel atom-molecule collisions*, Chem. Phys. Lett. **280**, 5 (1997).

[6] I. Simbotin, S. Ghosal, and R. Côté, *Threshold resonance effects in reactive processes*, Phys. Rev. A **89**, 040701 (2014).

[7] E. P. Wigner, *On the Behavior of Cross Sections Near Thresholds*, Phys. Rev. **73**, 1002 (1948).

[8] R. Côté and A. Dalgarno, *Mechanism for the production of vibrationally excited ultracold molecules of* $^7Li_2$, Chem. Phys. Lett. **279**, 50 (1997).

[9] R. Côté and A. Dalgarno, *Mechanism for the production of* $^6Li_2$ *and* $^7Li_2$ *ultracold molecules*, J. Mol. Spectr. **195**, 236 (1999).

[10] A. Fioretti, D. Comparat, A. Crubellier, O. Dulieu, F. Masnou-Seeuws, and P. Pillet, *Formation of cold Cs_2 molecules through photoassociation*, Phys. Rev. Lett. **80**, 4402 (1998).

[11] T. Takekoshi, B. M. Patterson, and R. J. Knize, *Observation of optically trapped cold cesium molecules*, Phys. Rev. Lett. **81**, 5105 (1998).

[12] L. D. Carr, D. DeMille, R. V. Krems, and J. Ye, *Cold and ultracold molecules: science, technology and applications*, New J. Phys. **11**, 055049 (2009).

[13] O. Dulieu, R. Krems, M. Weidemuller, and S. Willitsch, *Physics and Chemistry of Cold Molecules*, Phys. Chem. Chem. Phys. **13**, 18703 (2011).

[14] G. Quéméner and P. S. Julienne, *Ultracold Molecules under Control!*, Chem. Rev. **112**, 4949 (2012).

[15] D. W. Chandler, *Cold and ultracold molecules: Spotlight on orbiting resonances*, J. Chem. Phys. **132**, 110901 (2010).

[16] S. Ospelkaus, K.-K. Ni, D. Wang, M. H. G. de Miranda, B. Neyenhuis, G. Quéméner, P. S. Julienne, J. L. Bohn, D. S. Jin, and J. Ye, *Quantum-State Controlled Chemical Reactions of Ultracold Potassium-Rubidium Molecules*, Science **327**, 853 (2010).

[17] M. de Miranda, A. Chotia, B. Neyenhuis, D. Wang, G. Quéméner, S. Ospelkaus, J. Bohn, J. Ye, and D. Jin, *Controlling the quantum stereodynamics of ultracold bimolecular reactions*, Nature Phys. **7**, 502 (2011).

[18] C. Chin, R. Grimm, P. Julienne, and E. Tiesinga, *Feshbach resonances in ultracold gases*, Rev. Mod. Phys. **82**, 1225 (2010).

[19] J. N. Byrd, J. A. Montgomery, and R. Côté, *Controllable Binding of Polar Molecules and Metastability of One-Dimensional Gases with Attractive Dipole Forces*, Phys. Rev. Lett. **109**, 083003 (2012).

[20] A. J. Leggett, *Bose-Einstein condensation in the alkali gases: Some fundamental concepts*, Rev. Mod. Phys. **73**, 307 (2001).

[21] S. Giorgini, L. P. Pitaevskii, and S. Stringari, *Theory of ultracold atomic Fermi gases*, Rev. Mod. Phys. **80**, 1215 (2008).

[22] T. Kraemer, M. Mark, P. Waldburger, J. G. Danzl, C. Chin, B. Engeser, A. D. Lange, K. Pilch, A. Jaakkola, H.-C. Nägerl, and R. Grimm, *Evidence for Efimov quantum states in an ultracold gas of caesium atoms*, Nature **440**, 315 (2006).

[23] D. Shu, I. Simbotin, and R. Côté, *Near Threshold Effects on Recombination and Vibrational Relaxation in Efimov Systems*, Chem. Phys. Chem. **17**, 3655 (2016).

[24] D. DeMille, *Quantum Computation with Trapped Polar Molecules*, Phys. Rev. Lett. **88**, 067901 (2002).

[25] S. F. Yelin, K. Kirby, and R. Côté, *Schemes for robust quantum computation with polar molecules*, Phys. Rev. A **74**, 050301 (2006).

[26] E. Kuznetsova, R. Côté, K. Kirby, and S. F. Yelin, *Analysis of experimental feasibility of polar-molecule–based phase gates*, Phys. Rev. A **78**, 012313 (2008).

[27] K. Willner and F. A. Gianturco, *Low-energy expansion of the Jost function for long-range potentials*, Phys. Rev. A **74**, 052715 (2006).

[28] H. R. Sadeghpour, J. L. Bohn, M. J. Cavagnero, B. D. Esry, I. I. Fabrikant, J. H. Macek, and A. R. P. Rau, *Collisions near threshold in atomic and molecular physics*, J. Phys. B **33**, R93 (2000).

[29] B. Gao, *Solutions of the Schrödinger equation for an attractive* $1/r^6$ *potential*, Phys. Rev. A **58**, 1728 (1998).

[30] B. Gao, *Repulsive* $1/r^3$ *interaction*, Phys. Rev. A **59**, 2778 (1999).

[31] I. Simbotin and R. Côté, *Jost function description of near threshold resonances for coupled-channel scattering*, Chem. Phys. **462**, 79 (2015).

[32] J. P. Neirotti, P. Serra, and S. Kais, *Electronic Structure Critical Parameters From Finite-Size Scaling*, Phys. Rev. Lett. **79**, 3142 (1997).

[33] P. Serra, J. P. Neirotti, and S. Kais, *Electronic Structure Critical Parameters For the Lithium Isoelectronic Series*, Phys. Rev. Lett. **80**, 5293 (1998).

[34] S. Kais and Q. Shi, *Quantum criticality and stability of three-body Coulomb systems*, Phys. Rev. A **62**, 060502 (2000).

[35] V. Efimov, *Force-range correction in the three-body problem: Application to three-nucleon systems*, Phys. Rev. C **44**, 2303 (1991).

[36] V. Efimov, *Effective interaction of three resonantly interacting particles and the force range*, Phys. Rev. C **47**, 1876 (1993).

[37] E. Garrido, D. V. Fedorov, and A. S. Jensen, *Efimov Effect in Nuclear Three-Body Resonance Decays*, Phys. Rev. Lett. **96**, 112501 (2006).

[38] V. Efimov, *Weakly bound states of three resonantly interacting particles*, Soviet Journal of Nuclear Physics **12** (1971).

[39] V. Efimov, *Energy levels arising from resonant two-body forces in a three-body system*, Physics Letters B **33**, 563 (1970).

[40] E. Braaten and H.-W. Hammer, *Universality in few-body systems with large scattering length*, Physics Reports **428**, 259 (2006).

[41] J. R. Williams, E. L. Hazlett, J. H. Huckans, R. W. Stites, Y. Zhang, and K. M. O'Hara, *Evidence for an Excited-State Efimov Trimer in a Three-Component Fermi Gas*, Phys. Rev. Lett. **103**, 130404 (2009).

[42] S. E. Pollack, D. Dries, and R. G. Hulet, *Universality in three-and four-body bound states of ultracold atoms*, Science **326**, 1683 (2009).

[43] N. Gross, Z. Shotan, S. Kokkelmans, and L. Khaykovich, *Nuclear-Spin-Independent Short-Range Three-Body Physics in Ultracold Atoms*, Phys. Rev. Lett. **105**, 103203 (2010).

[44] M. Berninger, A. Zenesini, B. Huang, W. Harm, H.-C. Nägerl, F. Ferlaino, R. Grimm, P. S. Julienne, and J. M. Hutson, *Universality of the Three-Body Parameter for Efimov States in Ultracold Cesium*, Phys. Rev. Lett. **107**, 120401 (2011).

[45] R. J. Wild, P. Makotyn, J. M. Pino, E. A. Cornell, and D. S. Jin, *Measurements of Tan's Contact in an Atomic Bose-Einstein Condensate*, Phys. Rev. Lett. **108**, 145305 (2012).

[46] S. Roy, M. Landini, A. Trenkwalder, G. Semeghini, G. Spagnolli, A. Simoni, M. Fattori, M. Inguscio, and G. Modugno, *Test of the Universality of the Three-Body Efimov Parameter at Narrow Feshbach Resonances*, Phys. Rev. Lett. **111**, 053202 (2013).

[47] T. B. Ottenstein, T. Lompe, M. Kohnen, A. N. Wenz, and S. Jochim, *Collisional Stability of a Three-Component Degenerate Fermi Gas*, Phys. Rev. Lett. **101**, 203202 (2008).

[48] J. H. Huckans, J. R. Williams, E. L. Hazlett, R. W. Stites, and K. M. O'Hara, *Three-Body Recombination in a Three-State Fermi Gas with Widely Tunable Interactions*, Phys. Rev. Lett. **102**, 165302 (2009).

[49] S. Nakajima, M. Horikoshi, T. Mukaiyama, P. Naidon, and M. Ueda, *Nonuniversal Efimov Atom-Dimer Resonances in a Three-Component Mixture of ^6Li*, Phys. Rev. Lett. **105**, 023201 (2010).

[50] G. Barontini, C. Weber, F. Rabatti, J. Catani, G. Thalhammer, M. Inguscio, and F. Minardi, *Observation of Heteronuclear Atomic Efimov Resonances*, Phys. Rev. Lett. **103**, 043201 (2009).

[51] R. S. Bloom, M.-G. Hu, T. D. Cumby, and D. S. Jin, *Tests of Universal Three-Body Physics in an Ultracold Bose-Fermi Mixture*, Phys. Rev. Lett. **111**, 105301 (2013).

[52] R. Pires, J. Ulmanis, S. Häfner, M. Repp, A. Arias, E. D. Kuhnle, and M. Weidemüller, *Observation of Efimov Resonances in a Mixture with Extreme Mass Imbalance*, Phys. Rev. Lett. **112**, 250404 (2014).

[53] S.-K. Tung, K. Jiménez-García, J. Johansen, C. V. Parker, and C. Chin, *Geometric Scaling of Efimov States in a ^6Li–^{133}Cs Mixture*, Phys. Rev. Lett. **113**, 240402 (2014).

[54] B. Huang, L. A. Sidorenkov, R. Grimm, and J. M. Hutson, *Observation of the Second Triatomic Resonance in Efimov's Scenario*, Phys. Rev. Lett. **112**, 190401 (2014).

[55] T. Lompe, T. B. Ottenstein, F. Serwane, K. Viering, A. N. Wenz, G. Zürn, and S. Jochim, *Atom-Dimer Scattering in a Three-Component Fermi Gas*, Phys. Rev. Lett. **105**, 103201 (2010).

[56] S. Knoop, F. Ferlaino, M. Mark, M. Berninger, H. Schöbel, H.-C. Nägerl, and R. Grimm, *Observation of an Efimov-like trimer resonance in ultracold atom–dimer scattering*, Nature Physics **5**, 227 (2009).

[57] M. Zaccanti, B. Deissler, C. DErrico, M. Fattori, M. Jona-Lasinio, S. Müller, G. Roati, M. Inguscio, and G. Modugno, *Observation of an Efimov spectrum in an atomic system*, Nature Physics **5**, 586 (2009).

[58] N. Gross, Z. Shotan, S. Kokkelmans, and L. Khaykovich, *Observation of Universality in Ultracold ^7Li Three-Body Recombination*, Phys. Rev. Lett. **103**, 163202 (2009).

[59] A. Zenesini, B. Huang, M. Berninger, H.-C. Nägerl, F. Ferlaino, and R. Grimm, *Resonant atom-dimer collisions in cesium: Testing universality at positive scattering lengths*, Phys. Rev. A **90**, 022704 (2014).

[60] M.-G. Hu, R. S. Bloom, D. S. Jin, and J. M. Goldwin, *Avalanche-mechanism loss at an atom-molecule Efimov resonance*, Phys. Rev. A **90**, 013619 (2014).

[61] P. Dyke, S. E. Pollack, and R. G. Hulet, *Finite-range corrections near a Feshbach resonance and their role in the Efimov effect*, Phys. Rev. A **88**, 023625 (2013).

[62] Y. Wang and B. D. Esry, *Universal three-body physics at finite energy near Feshbach resonances*, New J. Phys. **13**, 035025 (2011).

[63] Y. Wang, J. P. D'Incao, H.-C. Nägerl, and B. D. Esry, *Colliding Bose-Einstein Condensates to Observe Efimov Physics*, Phys. Rev. Lett. **104**, 113201 (2010).

[64] U. Eismann, L. Khaykovich, S. Laurent, I. Ferrier-Barbut, B. S. Rem, A. T. Grier, M. Delehaye, F. Chevy, C. Salomon, L.-C. Ha, and C. Chin, *Universal Loss Dynamics in a Unitary Bose Gas*, Phys. Rev. X **6**, 021025 (2016).

[65] B. S. Rem, A. T. Grier, I. Ferrier-Barbut, U. Eismann, T. Langen, N. Navon, L. Khaykovich, F. Werner, D. S. Petrov, F. Chevy, and C. Salomon, *Lifetime of the Bose Gas with Resonant Interactions*, Phys. Rev. Lett. **110**, 163202 (2013).

[66] P. K. Sørensen, D. V. Fedorov, A. S. Jensen, and N. T. Zinner, *Three-body recombination at finite energy within an optical model*, Phys. Rev. A **88**, 042518 (2013).

[67] B. Huang, L. A. Sidorenkov, and R. Grimm, *Finite-temperature effects on a triatomic Efimov resonance in ultracold cesium*, Phys. Rev. A **91**, 063622 (2015).

[68] Y. Wang, J. P. D'Incao, and B. D. Esry, *Ultracold Few-Body Systems*, volume 62 of *Adv. At. Mol. Opt. Phys.*, chapter 1, (1 – 115), Academic Press (2013).

[69] J. P. D'Incao and B. D. Esry, *Scattering Length Scaling Laws for Ultracold Three-Body Collisions*, Phys. Rev. Lett. **94**, 213201 (2005).

[70] F. W. J. Olver and L. C. Maximon, *NIST Handbook of Mathematical Functions*, chapter 10, Cambridge University Press (2010).

[71] W. E. Milne, *The Numerical Determination of Characteristic Numbers*, Phys. Rev. **35**, 863 (1930).

[72] J. L. Bohn, *Phase-amplitude method applied to doubly excited states of He* ($^1S^e$), Phys. Rev. A **49**, 3761 (1994).

[73] J. L. Bohn and P. S. Julienne, *Semianalytic theory of laser-assisted resonant cold collisions*, Phys. Rev. A **60**, 414 (1999).

[74] F. Robicheaux, U. Fano, M. Cavagnero, and D. A. Harmin, *Generalized WKB and Milne solutions to one-dimensional wave equations*, Phys. Rev. A **35**, 3619 (1987).

[75] C. Jungen, F. Texier, and C. Jungen, *On the construction of basis functions for quantum defect theory in arbitrary fields*, J. Phys. B **33**, 2495 (2000).

[76] J. P. Burke, C. H. Greene, and J. L. Bohn, *Multichannel Cold Collisions: Simple Dependences on Energy and Magnetic Field*, Phys. Rev. Lett. **81**, 3355 (1998).

[77] B. Yoo and C. H. Greene, *Implementation of the quantum-defect theory for arbitrary long-range potentials*, Phys. Rev. A **34**, 1635 (1986).

[78] C. H. Greene, A. R. P. Rau, and U. Fano, *General form of the quantum-defect theory. II*, Phys. Rev. A **26**, 2441 (1982).

[79] A. Crubellier and E. Luc-Koenig, *Threshold effects in the photoassociation of cold atoms: R^{-6} model in the Milne formalism*, J. Phys. B **39**, 1417 (2006).

[80] L. B. Zhao, I. I. Fabrikant, J. B. Delos, F. Lépine, S. Cohen, and C. Bordas, *Coupled-channel theory of photoionization microscopy*, Phys. Rev. A **85**, 053421 (2012).

[81] F. H. J. Hall, M. Aymar, M. Raoult, O. Dulieu, and S. Willitsch, *Light-assisted cold chemical reactions of barium ions with rubidium atoms*, Mol. Phys. **111**, 1683 (2013).

[82] M. Raoult and G. G. Balint-Kurti, *Application of Generalized Quantum-Defect Theory to Photodissociation Processes: Predissociation of Ar-H_2*, Phys. Rev. Lett. **61**, 2538 (1988).

[83] I. Fourré and M. Raoult, *Application of generalized quantum defect theory to van der Waals complex bound state calculations*, J. Chem. Phys. **101**, 8709 (1994).

[84] J. M. Lecomte and M. Raoult, *Above threshold accumulated phase in molecular potentials*, Mol. Phys. **105**, 1575 (2007).

[85] S.-Y. Lee and J. C. Light, *On the quantum momentum method for the exact solution of separale multiple well bound state and scattering problems*, Chem. Phys. Lett. **25**, 435 (1974).

[86] J.-M. Yuan and J. C. Light, *Direct calculation of the electron density via the milne equation*, Int. J. Quantum Chem. **8**, 305 (1974).

[87] A. Bar-Shalom, M. Klapisch, and J. Oreg, *HULLAC, an integrated computer package for atomic processes in plasmas*, J. Quant. Spectr. Rad. Transf. **71**, 169 (2001).

[88] J. Rundgren, *Elastic electron-atom scattering in amplitude-phase representation with application to electron diffraction and spectroscopy*, Phys. Rev. B **76**, 195441 (2007).

[89] C. Rogers, B. Malomed, K. Chow, and H. An, *ErmakovRayReid systems in nonlinear optics*, J. Phys. A **43**, 455214 (2010).

[90] A. Thilagam, *Berry phase in arbitrary dimensions*, J. Phys. A **43**, 354004 (2010).

[91] I. A. Pedrosa, *Quantum electromagnetic waves in nonstationary linear media*, Phys. Rev. A **83**, 032108 (2011).

[92] G. Reinisch, *Radial action-phase quantization in BoseEinstein condensates*, Phys. Lett. A **372**, 769 (2008).

[93] J. E. Lidsey, *Cosmic dynamics of BoseEinstein condensates*, Class. Quantum Grav. **21**, 777 (2004).

[94] R. M. Hawkins and J. E. Lidsey, *Ermakov-Pinney equation in scalar field cosmologies*, Phys. Rev. D **66**, 023523 (2002).

[95] R. Kaushal, *Existence of a space invariant in the Tolman-Oppenheimer-Volkoff theory*, Class. Quantum Grav. **15**, 197 (1998).

[96] K. Bakke, I. Pedrosa, and C. Furtado, *Geometric phases and squeezed quantum states of relic gravitons*, J. Math. Phys. **50**, 113521 (2009).

[97] K. V. Khmelnytskaya and H. C. Rosu, *An amplitude-phase (Ermakov–Lewis) approach for the Jackiw–Pi model of bilayer graphene*, J. Phys. A **42**, 042004 (2008).

[98] F. H. Mies and M. Raoult, *Analysis of threshold effects in ultracold atomic collisions*, Phys. Rev. A **62**, 012708 (2000).

[99] R. Osséni, O. Dulieu, and M. Raoult, *Optimization of generalized multichannel quantum defect reference functions for Feshbach resonance characterization*, J. Phys. B **42**, 185202 (2009).

[100] Z. Idziaszek, A. Simoni, T. Calarco, and P. S. Julienne, *Multichannel quantum-defect theory for ultracold atomion collisions*, New J. Phys. **13**, 083005 (2011).

[101] E. Y. Sidky, *The Phase-Amplitude Method of Solving the Wave Equation*, Phys. Essays **13**, 408 (2000).

[102] A. Matzkin, *Smooth amplitude-phase formulation of the Schrödinger equation based on the Ermakov invariant*, Phys. Rev. A **63**, 012103 (2000).

[103] W. K. Schief, *A discrete Pinney equation*, Appl. Math. Lett. **10**, 13 (1997).

[104] S. Moyo and P. Leach, *Exceptional Properties of Second and Third Order Ordinary Differential Equations of Maximal Symmetry*, J. Math. Anal. Appl. **252**, 840 (2000).

[105] S. Kiyokawa, *Exact solution to the Coulomb wave using the linearized phase–amplitude method*, AIP Adv. **5**, 087150 (2015).

[106] E. Pinney, Proc. Am. Math. Soc. **1**, 681 (1950).

[107] C. W. Clenshaw and A. R. Curtis, *A method for numerical integration on an automatic computer*, Numer. Math. **2**, 197 (1960).

[108] S. E. El-gendi, *Chebyshev Solution of Differential, Integral and Integro-Differential Equations*, Comput. J. **12**, 282 (1969).

[109] L. Greengard, *Spectral Integration and Two-Point Boundary Value Problems*, SIAM J. Numer. Anal. **28**, 1071 (1991).

[110] R. Gonzales, J. Eisert, I. Koltracht, M. Neumann, and G. Rawitscher, *Integral Equation Method for the Continuous Spectrum Radial Schrdinger Equation*, J. Comput. Phys. **134**, 134 (1997).

[111] B. Mihaila and I. Mihaila, *Numerical approximations using Chebyshev polynomial expansions: El-gendi's method revisited*, J. Phys. A **35**, 731 (2002).

[112] G. Rawitscher, *A spectral PhaseAmplitude method for propagating a wave function to large distances*, Comput. Phys. Commun. **191**, 33 (2015).

[113] M. J. Seaton, *Coulomb functions for attractive and repulsive potentials and for positive and negative energies*, Comput. Phys. Comm. **146**, 225 (2002).

[114] H. Friedrich and A. Jurisch, *Quantum Reflection Times for Attractive Potential Tails*, Phys. Rev. Lett. **92**, 103202 (2004).

[115] R. Côté, H. Friedrich, and J. Trost, *Reflection above potential steps*, Phys. Rev. A **56**, 1781 (1997).

[116] B. Segev, R. Côté, and M. G. Raizen, *Quantum reflection from an atomic mirror*, Phys. Rev. A **56**, R3350 (1997).

[117] R. Côté, B. Segev, and M. G. Raizen, *Retardation effects on quantum reflection from an evanescent-wave atomic mirror*, Phys. Rev. A **58**, 3999 (1998).

[118] R. Côté and B. Segev, *Quantum reflection engineering: The bichromatic evanescent-wave mirror*, Phys. Rev. A **67**, 041604 (2003).

[119] S. Kallush, B. Segev, and R. Côté, *Manipulating atoms and molecules with evanescent-wave mirrors*, Eur. Phys. J. D **35**, 3 (2005).

[120] V. A. Mandelshtam, T. R. Ravuri, and H. S. Taylor, *Calculation of the density of resonance states using the stabilization method*, Phys. Rev. Lett. **70**, 1932 (1993).

[121] J. Babb and M. Du, *Quantum-mechanical calculation of quasi-bound energies and resonance widths for the helium molecular dication He22+*, Chemical Physics Letters **167**, 273 (1990).

[122] E. Y. Sidky and I. Ben-Itzhak, *Phase-amplitude method for calculating resonance energies and widths for one-dimensional potentials*, Phys. Rev. A **60**, 3586 (1999).

[123] D. Shu, I. Simbotin, and R. Côté, *Integral representation for scattering phase shifts via the phase-amplitude approach*, Phys. Rev. A **97**, 022701 (2018).

[124] G. Breit and E. Wigner, *Capture of Slow Neutrons*, Phys. Rev. **49**, 519 (1936).